UNIVERSIDADE
BEIRA INTERIOR

Development and functionalization of gold nanoparticles with silica coating for application in cancer therapy

Ariana Soraia Carreira Gonçalves

Dissertação para obtenção do Grau de Mestre em
Ciências Biomédicas
(2º ciclo de estudos)

Orientador: Prof. Doutor Ilídio Joaquim Sobreira Correia
Co-orientador: Doutor André Ferreira Moreira
Co-orientador: Mestre Ana Carolina Félix Rodrigues

setembro de 2020

"The more our knowledge increases, the more evident our ignorance becomes."

- John F. Kennedy

Dedication

À minha família, Miguel e ao senhor Quirino.

Acknowledgments

Antes de tudo queria agradecer ao meu orientador, Professor Doutor Ilídio Correia, por me ter dado a oportunidade de fazer parte do seu grupo de investigação. Agradecer de igual modo por toda a ajuda e por mostrar que com trabalho tudo é possível. A sua orientação e recomendações foram essenciais para a evolução do meu trabalho e também para o meu crescimento pessoal e profissional.

Ao meu co-orientador, Doutor André Moreira, quero agradecer por toda a ajuda, tempo despendido comigo ao longo deste ano. Agradeço de igual forma, todo o conhecimento que me transmitiu e pela constante disponibilidade para tirar dúvidas. Sem a sua ajuda, nada teria sido possível!

À minha co-orientadora, Mestre Ana Carolina Rodrigues, quero agradecer toda a paciência que teve comigo, toda a ajuda que providenciou, todos os conhecimentos que me transmitiu e pela troca de ideias que efetuámos ao longo do desenvolvimento desta tese. Obrigada por tudo!

Aos meus colegas de grupo de investigação, queria agradecer toda ajuda, compreensão e pela boa disposição que tornaram toda esta jornada mais agradável. Agradeço a todos por tornarem este último ano mais fácil de ultrapassar.

Às amigas que a Covilhã me deu, Andreia, Ana, Patrícia e Diana agradeço por estarem sempre comigo. Obrigada por aturarem as minhas crises de nervos, as minhas crises de choro e por serem as minhas mães da Covilhã. Um especial agradecimento à Andreia, por ser aquela amiga que me acompanhou desde o primeiro dia na Covilhã e por me mostrar que amizades ao acaso são as melhores amizades que se podem ter na vida. Agradeço por toda a ajuda, por todas as lágrimas que partilhou comigo e por todas as gargalhadas que tornou possível.

À minha família, não há maneira possível de agradecer por todos os esforços que fizeram para que tudo isto fosse possível. Aos meus pais agradeço todo o amor que me deram e todas as palavras de incentivo que me fizeram entender que nunca se desiste à primeira. Às minhas irmãs agradeço por estarem sempre lá e nunca me deixarem desistir, por serem o meu porto seguro. Ao meu avô, agradeço por ser a pessoa que mais se orgulha dos meus esforços, por perceber que um estudante também sofre e por estar sempre lá quando precisei de carinho e do seu caloroso colo.

Por fim, quero agradecer ao Miguel, que foi a pessoa que mais me ajudou nesta jornada. Obrigada por todos os dias que partilhaste comigo ao longo destes 5 anos. Agradeço-te todo o amor e paciência, sem ti nada teria sido possível!

Resumo

O cancro é uma das principais causas de morte em todo o mundo, cuja incidência se prevê que continue a aumentar ao longo das próximas décadas. A elevada taxa de mortalidade associada a esta doença é explicada pela toxicidade não específica e reduzida eficácia terapêutica dos tratamentos usados na clínica, nomeadamente a cirurgia, quimioterapia e radioterapia. Em particular, os agentes quimioterapêuticos apresentam uma rápida degradação bem como reduzida solubilidade e seletividade para as células cancerígenas. Dentro das novas abordagens terapêuticas que têm vindo a ser desenvolvidas, destaca-se a aplicação de nanomateriais capazes de mediar um efeito fototérmico (*i.e.* aumentar a temperatura em resposta a um estímulo de luz com um determinado comprimento de onda), com o objetivo de eliminar as células cancerígenas. Dentro dos vários nanomateriais aplicados na terapia fototérmica (PTT), destacam-se as nanopartículas de ouro revestidas com sílica (AuMSS) que apresentam excelentes propriedades físico-químicas que permitem a sua ação como agentes fototérmicos e de entrega de fármacos. Os diferentes parâmetros do núcleo de ouro (*e.g.* tamanho, forma) podem ser ajustados para melhorar a capacidade fototérmica destas nanopartículas e, consequentemente, a sua eficácia terapêutica. Adicionalmente, a combinação das nanopartículas AuMSS com outros materiais e moléculas pode melhorar a eficácia fototérmica das mesmas. Apesar do elevado potencial terapêutico apresentado por estas nanopartículas, a sua aplicação clínica é dificultada pelo seu reduzido tempo de circulação na corrente sanguínea e baixa especificidade para o tecido tumoral.

Desta forma, o trabalho desenvolvido durante o meu 2º ano de mestrado teve como objetivo proceder à funcionalização da superfície das nanopartículas AuMSS em forma de bastonete com polímeros biofuncionais, com a finalidade de aumentar o seu tempo de circulação na corrente sanguínea e ainda incrementar a sua internalização pelas células cancerígenas. Para tal, as AuMSS em forma de bastonete foram quimicamente modificadas com Polietilenoglicol metil éter (PEG-CH_3) e Gelatina (GEL). O PEG-CH_3 foi escolhido devido à sua natureza anfifílica e elevada solubilidade, propriedades estas que permitem reduzir a adsorção de proteínas na superfície das nanopartículas e, consequentemente, aumentar o seu tempo de circulação na corrente sanguínea. Por outro lado, a GEL trata-se de um polímero natural que possui na sua constituição sequências de aminoácidos de arginina-glicina-ácido aspártico (RGD) cujos recetores estão sobreexpressos nas células cancerígenas. Paralelamente, o IR780 foi também encapsulado pela primeira vez nas nanopartículas AuMSS de forma a aumentar a sua

capacidade fototérmica e fotodinâmica e, consequentemente, o seu potencial terapêutico.

Os resultados obtidos neste estudo demonstraram que o revestimento dos AuMSS em forma de bastonete com os polímeros GEL e PEG-CH_3 permitiu a neutralização da carga de superfície das nanopartículas de -23 para -7.46 mV. O sucesso da ligação dos polímeros às nanopartículas foi ainda confirmado por análise termogravimétrica (TGA) e por espectroscopia de infravermelho por transformada de Fourier (FTIR). Nos estudos efetuados *in vitro*, as nanoformulações mostraram ser biocompatíveis quando em contacto com células cancerígenas (cancro do colo do útero) e células saudáveis (fibroblastos) até à máxima concentração testada de 200 $\mu g.mL^{-1}$. Adicionalmente a funcionalização das nanopartículas com GEL aumentou a sua internalização pelas células cancerígenas não afetando a sua capacidade fototérmica. Contudo a encapsulação do IR780 (IR780@AuMSS/T-PEG-CH_3/T-GEL) promoveu um aumento da capacidade fototérmica das nanopartículas e da geração de espécies reativas de oxigénio (ROS). Por fim, todas as nanoformulações estudadas foram capazes de induzir eficazmente a morte das células cancerígenas.

Em suma, os resultados obtidos confirmam que a funcionalização das nanopartículas com os polímeros GEL e PEG-CH_3 foi bem-sucedida. Adicionalmente, foi ainda demostrado o potencial da combinação das nanopartículas AuMSS com o IR780, podendo estas realizar simultaneamente PTT e terapia fotodinâmica com direcionamento para as células cancerígenas.

Palavras-chave

Cancro;nanopartículas de ouro com revestimento de sílica;terapia fototérmica; IR780;GEL; PEG-CH_3.

Resumo alargado

O cancro é uma das principais causas de morte em todo o mundo, cuja incidência se prevê que continue a aumentar ao longo das próximas décadas. A elevada taxa de mortalidade associada a esta doença é explicada pela toxicidade não específica e reduzida eficácia terapêutica dos tratamentos usados na clínica, nomeadamente, a cirurgia, quimioterapia e radioterapia. Em particular, a quimioterapia é o tratamento mais utilizado, apesar das suas diversas limitações. Os agentes quimioterapêuticos administrados apresentam uma baixa solubilidade em água, são facilmente degradados e eliminados, apresentam uma baixa seletividade para o tecido tumoral, bem como diversos efeitos secundários associados e, consequentemente, uma baixa eficácia terapêutica. Para além disso, as células cancerígenas podem adquirir um fenótipo de resistência a múltiplos fármacos o que limita ainda mais a eficácia deste tipo de tratamento. Desta forma, torna-se urgente o desenvolvimento de novas abordagens terapêuticas no combate ao cancro.

Os avanços na área da nanotecnologia permitiram o desenvolvimento de diferentes sistemas à escala nanométrica capazes de ultrapassar as limitações apresentadas pelas terapias convencionais, abrindo assim caminho para uma nova geração de medicamentos que podem ser aplicados no tratamento do cancro. Estes nanosistemas (nanopartículas) constituem uma abordagem terapêutica promissora, uma vez que possuem a capacidade de encapsular fármacos, protegem-nos da degradação e eliminação prematura, controlam a sua libertação e permitem que estes sejam entregues especificamente às células cancerígenas. Paralelamente, a terapia fototérmica (PTT) mediada por nanomateriais tem atraído a atenção de diferentes investigadores em todo mundo. Esta abordagem terapêutica explora a capacidade intrínseca que as nanopartículas possuem em se acumularem no tumor. Uma vez presentes no tumor e sob exposição a estímulos específicos, nomeadamente radiação do infravermelho próximo (NIR), determinadas nanopartículas conseguem converter a energia da luz incidente em calor. Este aumento de temperatura localizado na região do tumor poderá induzir efeitos citotóxicos nas células cancerígenas, que podem levar à sua destruição ou sensibilização para outras terapias (*e.g.* quimioterapia). A utilização de luz na região NIR permite que este tipo de terapia não induza danos nos tecidos saudáveis, uma vez que o comprimento de onda utilizado (750-1,100 nm) não interage com os componentes biológicos. Desta forma, a ação combinada da quimioterapia com a PTT constitui uma das abordagens anticancerígenas mais exploradas.

Dentro dos nanomateriais com capacidade de mediar um efeito fototérmico, as nanopartículas de ouro com revestimento de sílica (AuMSS) possuem propriedades físico-químicas únicas, que permitem a sua aplicação não só na terapia (p.ex. PTT, entrega de fármacos) como na imagiologia. O núcleo de ouro possui elevada absorção na região NIR conferindo a capacidade de converter a energia da radiação incidente em calor. Este aumento de temperatura poderá promover alterações celulares irreversíveis nas células cancerígenas. Por sua vez, o revestimento com sílica mesoporosa protege o núcleo de ouro de fenómenos de degradação e agregação, servindo ainda como um local de carga adicional para o encapsulamento de diferentes agentes terapêuticos no interior dos seus poros. Apesar do elevado potencial terapêutico apresentado por estas nanopartículas a sua aplicação é muitas vezes dificultada pelo seu reduzido tempo de circulação na corrente sanguínea e reduzida especificidade para o tecido tumoral.

Desta forma, diversas abordagens têm vindo a ser desenvolvidas com o intuito de melhorar a capacidade fototérmica das nanopartículas bem como a sua especificidade para o tecido tumoral. No caso das nanopartículas à base de ouro, a otimização da eficácia fototérmica pode ser conseguida através do ajuste de diferentes parâmetros físicos (*e.g.* tamanho, forma) bem como através da sua combinação com outros materiais e moléculas. Adicionalmente, a superfície das nanopartículas pode ser modificada com agentes (p.ex. anticorpos, aptâmeros, proteínas) que vão permitir o direcionamento ativo destas para o tecido tumoral, explorando o reconhecimento específicos de moléculas sobreexpressas ou unicamente expressas nas células cancerígenas.

Assim sendo, o trabalho desenvolvido durante o meu 2º ano de mestrado teve como objetivo proceder à funcionalização da superfície das nanopartículas AuMSS em forma de bastonete com polímeros biofuncionais. Esta modificação de superfície teve como finalidade aumentar o tempo de circulação das nanopartículas na corrente sanguínea e ainda incrementar a sua internalização pelas células cancerígenas. Para tal, o Polietilenoglicol metil éter (PEG-CH_3) e a Gelatina (GEL) foram quimicamente imobilizados na superfície das AuMSS. O PEG-CH_3 foi escolhido devido à sua natureza anfifílica e elevada solubilidade. Estas propriedades permitem reduzir a adsorção de proteínas na superfície das nanopartículas e, consequentemente, aumentar o seu tempo de circulação na corrente sanguínea e ainda a probabilidade de se acumularem no tumor. Por outro lado, a GEL trata-se de um polímero natural, biodegradável e biocompatível que possui na sua constituição sequências de aminoácidos de arginina-glicina-ácido aspártico (RGD) cujos recetores de integrinas $\alpha v\beta_3$ estão sobreexpressos nas membranas das células cancerígenas. Paralelamente, o IR780 foi também encapsulado pela primeira vez nas nanopartículas AuMSS. Esta molécula tem a capacidade de promover um

aumento de temperatura (PTT) e ainda produzir espécies reativas de oxigénio (terapia fotodinâmica-PDT) sob ação de um laser NIR. Contudo quando presente na sua forma livre, o IR780 possui uma baixa solubilidade e elevada toxicidade. Desta forma, a combinação das nanopartículas AuMSS e IR780 permitirá aumentar a capacidade fototérmica e fotodinâmica do nanosistema e, consequentemente, o seu potencial terapêutico.

Os resultados obtidos neste estudo demonstram que as AuMSS em forma de bastonete apresentaram uma morfologia uniforme, com um núcleo de ouro e revestimento de sílica bem definidos. A funcionalização dos AuMSS em forma de bastonete com a GEL e PEG-CH_3 foi efetuada através de uma reação de condensação entre as AuMSS e os polímeros previamente modificados com um silano (Isocianato de 3-(trimetoxisilil) propril-TESPIC). A modificação das AuMSS com GEL e PEG-CH_3 resultou na neutralização da carga de superfície dos AuMSS de -23 para -7.46 mV. Adicionalmente, a imobilização da GEL e PEG-CH_3 na superfície das AuMSS foi ainda confirmada através das técnicas de FTIR e TGA. Por outro lado, avaliando a capacidade fototérmica dos nanosistemas observou-se que tanto as AuMSS e AuMSS/T-PEG-CH_3/T-GEL mediaram um aumento de temperatura de ≈35°C quando irradiadas com radiação NIR. Contudo, as nanopartículas AuMSS/T-PEG-CH_3/T-GEL carregadas com IR780 apresentaram uma capacidade fototérmica superior promovendo um aumento de temperatura de aproximadamente ≈40°C. Nos ensaios biológicos *in vitro,* foi demostrada a biocompatibilidade das AuMSS e AuMSS/T-PEG-CH_3/T-GEL até concentrações máximas de 200 $\mu g.mL^{-1}$. Para além disso, verificou-se que a funcionalização com GEL aumentou a internalização das nanopartículas pelas células cancerígenas do colo do útero. Adicionalmente, também foi verificado que a encapsulação do IR780 (IR780@AuMSS/T-PEG-CH_3/T-GEL) além de aumentar a capacidade fototérmica das nanopartículas também promove uma maior geração de espécies reativas de oxigénio (ROS) quando irradiadas com luz NIR. Por fim, foi observado que as AuMSS/T-PEG-CH_3/T-GEL mediavam a destruição completa das células cancerígenas, independentemente da presença ou ausência de IR780, quando irradiadas com luz NIR e a concentrações superiores a 100 $\mu g.mL^{-1}$. Por outro, foi observada uma maior toxicidade nas AuMSS/T-PEG-CH_3/T-GEL contendo IR780 quando a concentração das nanopartículas foi reduzida para 50 $\mu g.mL^{-1}$.

Em suma, os resultados obtidos confirmam a modificação da superfície das AuMSS em forma de bastonete com os polímeros GEL e PEG-CH_3. Esta funcionalização aumentou a seletividade das AuMSS para as células cancerígenas do colo do útero. Adicionalmente, foi ainda demonstrado o potencial da combinação das nanopartículas AuMSS com o

IR780, podendo este nanosistema realizar simultaneamente PTT e PDT, o que consequentemente se traduz numa maior capacidade anticancerígena.

Abstract

Cancer is one of the leading causes of death worldwide and its incidence is expected to continue to increase over the next few decades. Such is explained by the non-specific toxicity and reduced therapeutic efficacy displayed by conventional treatments currently used in the clinic, namely surgery, chemotherapy, and radiotherapy. Particularly, chemotherapeutic agents are rapidly degraded and present a reduced solubility and selectivity to cancer cells. Among the new therapeutic approaches that have been developed, the application of nanomaterials capable of mediating a photothermal effect (*i.e.* increasing the temperature in response to a light stimulus with a specific wavelength), to induce the cancer cell deaths have been gaining increased attention. Among the several nanomaterials applied in photothermal therapy (PTT), gold core silica shell (AuMSS) nanoparticles presented excellent physicochemical properties that allow their application as photothermal and drug delivery agents. Different parameters of the gold core (*e.g.* size, shape) can be optimized to improve the photothermal capacity of these nanoparticles, and consequently their therapeutic efficacy. Additionally, the combination of AuMSS nanoparticles with other materials and molecules can also improve their photothermal effectiveness. However, despite the high therapeutic potential of AuMSS nanoparticles, their clinical application is hampered by their reduced circulation time in the bloodstream and lack of specificity to the tumoral tissue.

Taking this into account, the research work developed during the second year of my MSc aimed to develop a new surface functionalization for rod-shaped AuMSS nanoparticles, based in biofunctional polymers to increase both its half-life in the bloodstream and internalization by cancer cells. For this purpose, the rod-shaped AuMSS nanoparticles were chemically modified with Polyethyleneglycol methyl ether (PEG-CH_3) and Gelatin (GEL). The PEG-CH_3 was chosen due to its amphiphilic nature and high solubility, which reduces the protein adsorption on the nanoparticles' surface and consequently increases its blood circulation time. On the other hand, GEL is a natural polymer that contains arginine-glycine-aspartic acid (RGD) amino acid sequences with specificity for receptors overexpressed in cancer cells. Simultaneously, the encapsulation of IR780 was also tested for the first time in AuMSS nanoparticles to increase the photothermal and photodynamic capacity, and consequently its therapeutic potential.

The obtained results demonstrated that the functionalization of rod-shaped AuMSS nanoparticles with GEL and PEG-CH_3 polymers led to a neutralization of the surface

charge from -23 to -7.46 mV. The successful incorporation of the polymers on nanoparticles surface was also confirmed by thermogravimetric analysis (TGA) and by Fourier transform infrared spectroscopy (FTIR). The *in vitro* studies demonstrated the biocompatibility of the different nanoformulations when in contact with cancer cells (cervical cancer) and healthy cells (fibroblasts) up to the maximum tested concentration of 200 $\mu g.mL^{-1}$. Additionally, the AuMSS functionalization with GEL increased their internalization by cancer cells without affecting their photothermal capacity. Otherwise, it was also observed that the encapsulation of IR780 resulted in an enhanced photothermal capacity of AuMSS/T-PEG-CH_3/T-GEL nanoparticles and increased the generation of reactive oxygen species (ROS) upon irradiation with a NIR laser. Finally, the AuMSS/T-PEG-CH_3/T-GEL nanoparticles were capable of effectively inducing the death of cancer cells.

In summary, the obtained results confirm the successful functionalization of AuMSS nanoparticles with the GEL and PEG-CH_3. Additionally, the potential of the AuMSS/IR780 combination was also demonstrated, where this nanosystem can simultaneously perform PTT and photodynamic therapy (PDT), which translates to an enhanced anticancer capacity.

Keywords

Cancer, gold core silica shell nanoparticles, photothermal therapy, IR780, GEL, PEG-CH_3.

List of Publications

Articles published in peer-reviewed international journals:

Gonçalves, A. S. C., Rodrigues, C. F., Moreira, A. F., Correia, I. J. "Strategies for improving the photothermal capacity of gold-based nanomedicines". Acta Biomaterialia (2020). DOI: 10.1016/j.actbio.2020.09.008

Index

Figure Index

Table Index

List of abbreviations

ANOVA	One-way analysis of variance
A.R.	Aspect ratio
AuMSS	Gold core silica shell nanoparticles
BSA	Bovine serum albumin
Calcein AM	Calcein acetozxmethyl
CLSM	Confocal laser scanning microscopy
CTAB	Cetyltrimethylammonium bromide
DOX	Doxorubicin
ECM	Extracellular matrix
E.E.	Encapsulation efficiency
EtOH	Ethanol
FITC	Fluorescein 5-isothiocyanate
FTIR	Fourier transform infrared spectroscopy
FibH	Primary normal human dermal fibroblast
GEL	Gelatin
GO	Graphene oxide
H_2DCF-DA	2',7'-Dichlorofluorescein diacetate
HA	Hyaluronic acid
HeLa	Human negroid cervix epithelioid carcinoma
HCl	Hydrochloric acid
ICG	Indocyanine green
IO	Iron oxide
K^-	Negative control
K^+	Positive control
L	Lenght
LSPR	Localized surface plasmon resonance
MCF-7	Breast cancer cell line
MDR	Multidrug resistance
NIR	Near-infrared
n.s.	Non-significant
PEG	Poly(ethylene glycol)
PEG-CH_3	Poly(ethylene glycol) methyl ether
PLGA	Poly(lactic-co-glycolic acid)

PBS	Phosphate-buffered saline
PDA	Polydopamine
PDT	Photodynamic therapy
PEI	Polyethyleneimine
PFA	Paraformaldehyde
PI	Propidium iodide
PPy	Polypyrrole
PTT	Photothermal therapy
RGD	Arginine-glycine-aspartic acid
ROS	Reactive oxygen species
s.d.	Standart derivation
TEM	Transmission electron microscopy
TEOS	Tetraethyl orthosilicate
TESPIC	3-(Triethoxysilyl)propyl isocyanate
TESPIC-PEG-CH_3	TESPIC modified PEG-CH_3
TESPIC-GEL	TESPIC modified GEL
TGA	Thermogravimetric analysis
THF	Tetrahydrofuran
TME	Tumor microenvironment
USA	United States of America
W	Width
WGA-Alexa Fluor® 594	Wheat germ agglutinin conjugate Alexa 594®

Chapter 1

Introduction

This chapter is based on the publication entitled: "*Strategies for improving the photothermal capacity of gold-based nanomedicines*", Acta Biomaterialia, 2020

1. Introduction

1.1. Cancer development, hallmarks, and treatments

1.1.1. Cancer

Cancer is one of the leading causes of death, with a growing incidence in the worldwide population [1]. In the current year, only in the United States of America (USA), it is predicted that more than one million eight hundred thousand new cancer cases will be detected and cancer will be responsible for more than six hundred thousand deaths [2]. Moreover, in the world, it is estimated that 1 in 5 men and 1 in 6 women develop cancer during their lifetime, and 1 in 8 men and 1 in 10 women die from cancer every year [3]. In Portugal, sixty thousand new cases and thirty thousand of cancer-related deaths were registered in 2018. Further, in the next five years, it is expected that the number of prevalent cancer cases will be approximately one hundred and fifty thousand [3]. As a matter of fact, a study developed by *Direção Geral de Saúde* (2017) reports that cancer incidence has been increasing at a rate of 3% per year, in Portugal [4].

Cancer is a highly complex group of diseases whose mechanisms are not yet fully understood. However, several risk factors have been associated with increased probabilities to develop cancer, including diet, smoking, alcohol and drug consumption, obesity, infections, and genetic predisposition [5, 6]. Moreover, the exposure to environmental agents (*e.g.* pollution and radiation), as well as the global population growth and aging, have been associated with cancer development [5]. Additionally, the gender of the population is also considered to be a factor in cancer prevalence [7]. In the most recent reports, men are the most affected by cancer, registering higher mortality and incidence rates. In men, lung cancer is the most prevalent and lethal, followed by prostate and colorectum cancer. In contrast, breast cancer is the most prevalent type of cancer in women, followed by lung and cervical cancer [3].

1.1.2. Cancer development and hallmarks

Cancer is a highly complex group of diseases characterized by the formation of a heterogeneous tissue that shows uncontrolled cellular proliferation through a multistep process in response to genetic and epigenetic alterations [8]. These alterations can ultimately lead to the malignant transformation of normal cells and promote the invasion of surrounding tissues or migration to other sites in the body [9].

Apart from cancer cells, cancer tissue is also composed of immune and stromal cells (*e.g.* endothelial cells and fibroblast), compounds of the extracellular matrix (ECM) (*e.g.* collagen), and signalling molecules that form the tumor microenvironment (TME)

[10]. The elements of TME establish dynamic interactions that play an important role in tumor establishment, progression, and metastasis. In fact, the interaction of cancer cells with TME elements can trigger different pro-survival, invasion, and proliferation pathways that are crucial for cancer development and progression. In this way, Hanahan and Weinberg defined several key characteristics designated by hallmarks of cancer that are responsible for the development, maintenance, and progression of cancer cells [11]. The capacity of cancer cells to maintain their proliferative signalling is one of its most important characteristics [11].

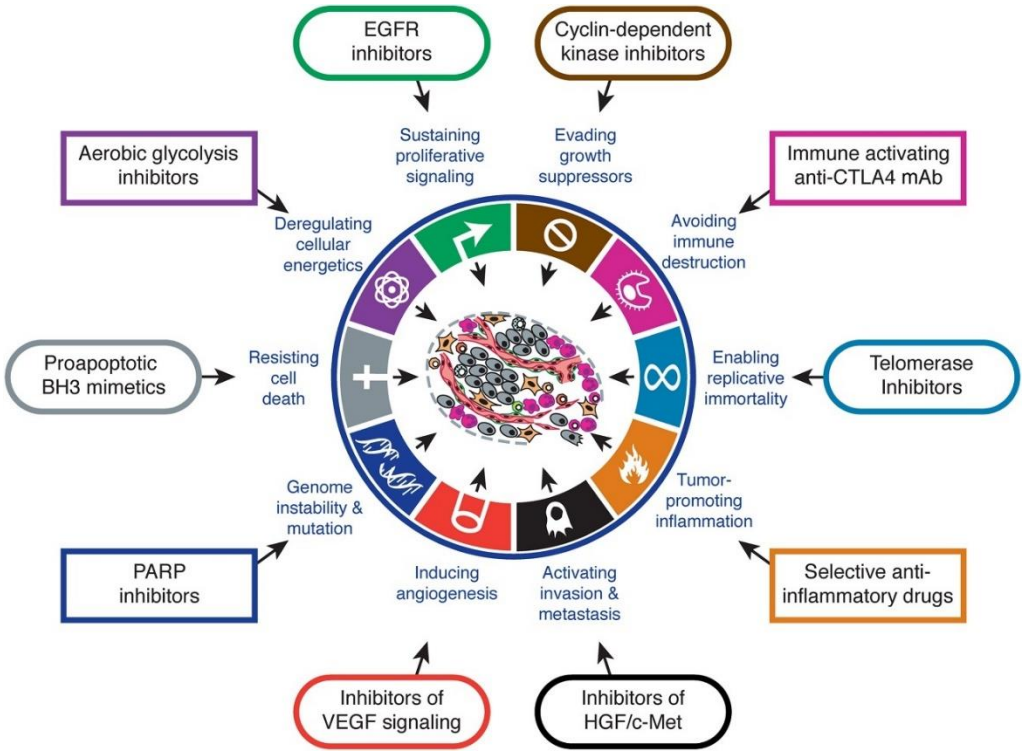

Figure 1: Cancer cells' hallmarks and examples of the drug types that target each one of these key characteristics for tumor growth and progression (Adapted from [11]).

In this way, cancer cells possess the ability and autonomy to produce their growth factors through autocrine signalling (*e.g.* platelet-derived growth factor), to stimulate the TME elements to produce growth factors (paracrine signalling) or even overexpress the receptors related to cell growth pathways [12, 13]. Thus, cancer cells become less dependent on the surrounding tissues and will be more responsive to lower levels of growth factors. On the other hand, cancer cells can become insensitive to anti-growth factors, particularly those responsible for cell apoptosis regulation (*e.g.* tumor suppressor protein 53 and retinoblastoma protein) and simultaneously increase the expression of anti-apoptotic proteins (*e.g.* B-cell lymphoma 2 family) [14-16]. Additionally, the overexpression of telomerase confers to cancer cells the potential to

replicate indefinitely. The telomerase is a DNA polymerase responsible for maintaining the length of telomeres (chromosomal ends of DNA) by adding repeated sequences to the DNA ends. In normal cells, the expression of telomerase is mostly absent, and through the replicative cycles the capacity to conserve the telomeres decreases, which consequently leads to cell apoptosis or senescence. In opposite, the overexpression of telomerase in cancer cells maintains the telomeres integrity, prevents the DNA damages, and avoids cancer cell death [17, 18].

Due to the high proliferative state of cancer cells, the continuous supply of nutrients and oxygen is crucial as well as an alternative to eliminate all metabolic wastes. All these facts require high tumor vascularization (blood and lymphatic vessels) and blood supply. Thus cancer cells can induce angiogenesis through the activation of angiogenic inducers (*e.g.* platelet-derived growth factors, vascular endothelial growth factor, and angiopoietins), and suppressing angiogenic inhibitors (*e.g.* thrombospondin-1), which facilitates the formation of new blood vessels [19, 20]. Additionally, cancer cells can acquire an invasive phenotype and metastasize through the inhibition of cell-cell and cell-ECM adhesion molecules (*e.g.* E-cadherin) and increase the production of enzymes that degrade the ECM. This in conjugation with a defective tumor vasculature (*i.e.* fenestra's with an abnormal size) enables the extravasation of cancer cells to other sites in the body [21, 22]. In recent years, it was also described that cancer cells can modify their cellular metabolism (glycolytic pathways) to support the high proliferative state and improve tumor progression [11]. Additionally, it was also described that cancer cells can evade recognition from the immune system and consequently avoid cellular destruction [11].

1.1.3. Conventional therapies

Currently, in the clinic, the most common treatments for cancer are surgery [23, 24], chemotherapy [25, 26], and radiotherapy [27, 28]. Particularly, the patients are subject to a combination of these therapies, usually a combination of surgery with chemotherapy and/or radiotherapy [28]. However, these therapeutic procedures are not selective, present a reduced efficacy, and promote several side effects (*e.g.* nausea, fatigue, pain, infertility, and cardiovascular toxicity) that in some cases can lead to organ failure or even patient death [29, 30]. In the case of surgery, the complete removal of the tumor is not guaranteed, and the surrounding healthy tissues can be affected during the procedure [31]. Similarly, radiotherapy can affect healthy tissues close to the tumor or even induce systemic damages [32]. In turn, chemotherapy uses highly cytotoxic drugs that present a low bioavailability, non-specific toxicity, rapid degradation, and low water solubility [33, 34]. Moreover, cancer cells can acquire a multipledrug resistance (MDR)

phenotype, being another factor that contributes to the reduction of the therapeutic effectiveness of chemotherapeutic agents [35]. In this case, cancer cells can surpass and modify the drugs' mechanisms of action by inhibiting the apoptosis, inducing mutations in the drug target, reducing the drugs' absorption, increasing the DNA repair and membrane transporters that are involved in drug efflux (*e.g.* glycoprotein P) [36]. Additionally, cancer cells with an MDR phenotype to a specific drug can acquire resistance to other drugs, even those with different chemical structures and mechanisms of action [37].

Despite the low efficacy and safety of chemotherapy, this remains in most cases the first line of treatment for cancer therapy [34]. In this way, a huge effort has been made to develop novel and more effective anti-cancer therapeutics, such as gene therapy [38], immunotherapy [39], and hyperthermia [40].

1.2. Hyperthermia

Currently, hyperthermia is one of the most studied modalities for cancer treatment [41]. Hyperthermia-based cancer therapies explore the exposition of the tumor site to higher temperatures to eliminate the cancer cells. Temperatures superior to 45°C can induce proteins denaturation and DNA damages as well as inhibit different cellular functions that will trigger the death of cancer cells [42, 43]. Alternatively, cancer cells can become more sensitized to other therapies (*e.g.* chemotherapy, radiotherapy) when temperature range between 40-45°C (mild hyperthermia). Conventional hyperthermia approaches often rely on outside-in approaches (*e.g.* superficial, regional, and whole-body hyperthermia) mediated by external sources (*e.g.* microwaves, radiofrequency, and thermal baths) to induce an increase in the tumor tissue temperature. The superficial hyperthermia increases the temperature in a small area and is used for treating superficial tumors or metastases in the skin or superficial tissues [44]. In the case of regional hyperthermia, entire tissues and organs are targeted [44, 45], whereas in the whole-body hyperthermia the overall temperature of the body is raised [44, 46]. However, in these approaches, the maximum temperature is reached in the body surface and decreases with the distance from the external heat source, which reduces the therapeutic efficacy. Moreover, the healthy tissues are also affected which can lead to several side effects [47].

Due to this, different studies have been performed to develop novel and more efficient approaches to surpass the limitations of conventional hyperthermia. To accomplish that, nanoparticles capable of generating heat in response to outside stimuli have been applied to trigger a localized and selective thermal ablation with minimal damages in the

surrounding healthy tissues [48]. The nanomaterials take advantage of their reduced size and the defective vasculature of tumors to become accumulated in cancer cells [47, 49]. Once accumulated in the tumor, the nanoparticles can mediate the thermal ablation of cancer cells in response to an external stimulus (*e.g.* near-infrared (NIR) laser, magnetic field, and ultrasound) [48]. This fact led to the development of nanomedicine-based hyperthermia therapies that can be classified in magnetic, ultrasound, and photothermal based hyperthermia therapies. Particularly, the nanomedicine-based photothermal therapy (PTT) is one of the most applied hyperthermia therapies, triggering the selective ablation of cancer cells by irradiation of the tumor area with a NIR laser [50]. The application of NIR radiation (700-1,200 nm) is crucial since the major components of the human body (*e.g.* water, proteins, collagen, hemoglobin) present an insignificant absorption in this region of the electromagnetic spectrum, which decrease the interactions and possible damages on healthy tissues [47, 51]. Moreover, the optical transparency of the human body to NIR radiation allows the minimization of absorption and scattering phenomena, which improves the radiation penetration and photothermal efficacy [47].

1.2.1. Nanomaterials application in photothermal therapy

The PTT mediated by nanomaterials is highly dependent on several parameters such as the capacity of the nanomaterials to generate heat and its selectivity towards the tumor tissue as well as the laser irradiation parameters. Considering the systemic administration, the nanomaterials must be able to accumulate in the tumor tissue by passive accumulation (enhanced permeability and retention effect or vascular burst events) and/or active targeting (receptor-ligand or antigen-antibody interactions) [52, 53]. Therefore, the nanomaterials bioavailability in tumors is closely linked to several physicochemical parameters such as the nanoparticle size, surface charge, corona, and surface moieties, as reviewed in detail by [54, 55]. Then, the nanomaterials PTT is triggered by irradiating the tumor zone with a light source, usually a NIR laser. Several laser light parameters affect the heat generation by the nanomaterials, such as wavelength, power density, number of irradiations, laser distance, and duration [56-59]. The biological transparency windows located in the NIR region of spectra (*i.e.* NIR-I; 700–900 nm and NIR-II; 1,000–1,700 nm) decrease the off-target interaction of the radiation and endow a deeper penetration in the body [60]. Further, the laser wavelength should also match the absorption peak of the nanomaterial to maximize the heat generation (Figure 2) [61]. Otherwise, the power density (total energy per second delivered into a specific area) of NIR irradiation will influence the penetration depth and the heat generated by the nanomaterials [62]. The utilization of higher power densities

is associated with an increased nanoparticle excitation and heat generation [63]. Nevertheless, excessive power densities can also induce side-effects (*e.g*. skin burns) due to off-target interaction [64]. Furthermore, the photothermal effect can also be enhanced by optimizing the duration of the laser irradiation and the application of multiple irradiation sessions [65, 66]. Upon the irradiation of the tumor site, the radiation-to-heat conversion efficiency of nanoparticles will be determinant for achieving an effective PTT. In gold-based nanomaterials, the radiation-to-heat conversion efficiency is dependent on the localized surface plasmon resonance (LSPR) phenomenon (defined by the nanoparticle size and shape) and can be enhanced through the combination of gold with other materials (*e.g*. silica, iron oxide, and graphene) or small molecules (*e.g*. IR780 and Indocyanine green (ICG)) (reviewed in section 1.2.5.).

1.2.2. Gold nanomaterials

Gold nanoparticles have been widely explored for cancer therapy applications, such as drug delivery and PTT [67]. Particularly, in PTT different design criteria affect the gold nanomaterials performance, such as the LSPR phenomenon, the radiation-to-heat conversion efficiency, and the surface functionalization. The LSPR phenomenon is defined by the light-induced resonant oscillation of the free electrons on the particle's surface, which can result in the light scattering or absorption [68]. Upon light absorption, the free electrons progress to an excited state and can release the absorbed energy in the form of heat during relaxation [69]. In gold nanomaterials, the LSPR wavelength can be adjusted to the NIR region by fine-tuning the particle size and organization [70]. Additionally, the shape also plays an important role in the LSPR phenomenon of gold nanomaterials. In this regard, the sphere, rod, star, and cage-like shapes are the most explored ones for the biological application of gold nanomaterials, namely in cancer PTT. Nevertheless, it is worth to notice that there are less explored shapes such as nanovesicles [71-73], bellflowers [74-76], nanobipyramids [77], and nanoprisms [78-83] that can also be explored to mediate a photothermal effect in response to irradiation with a NIR laser. The optimization of gold nanostructures to match the LSPR wavelength with the NIR laser irradiation results in increased energy absorption and consequently an enhanced heat generation (Figure 2).

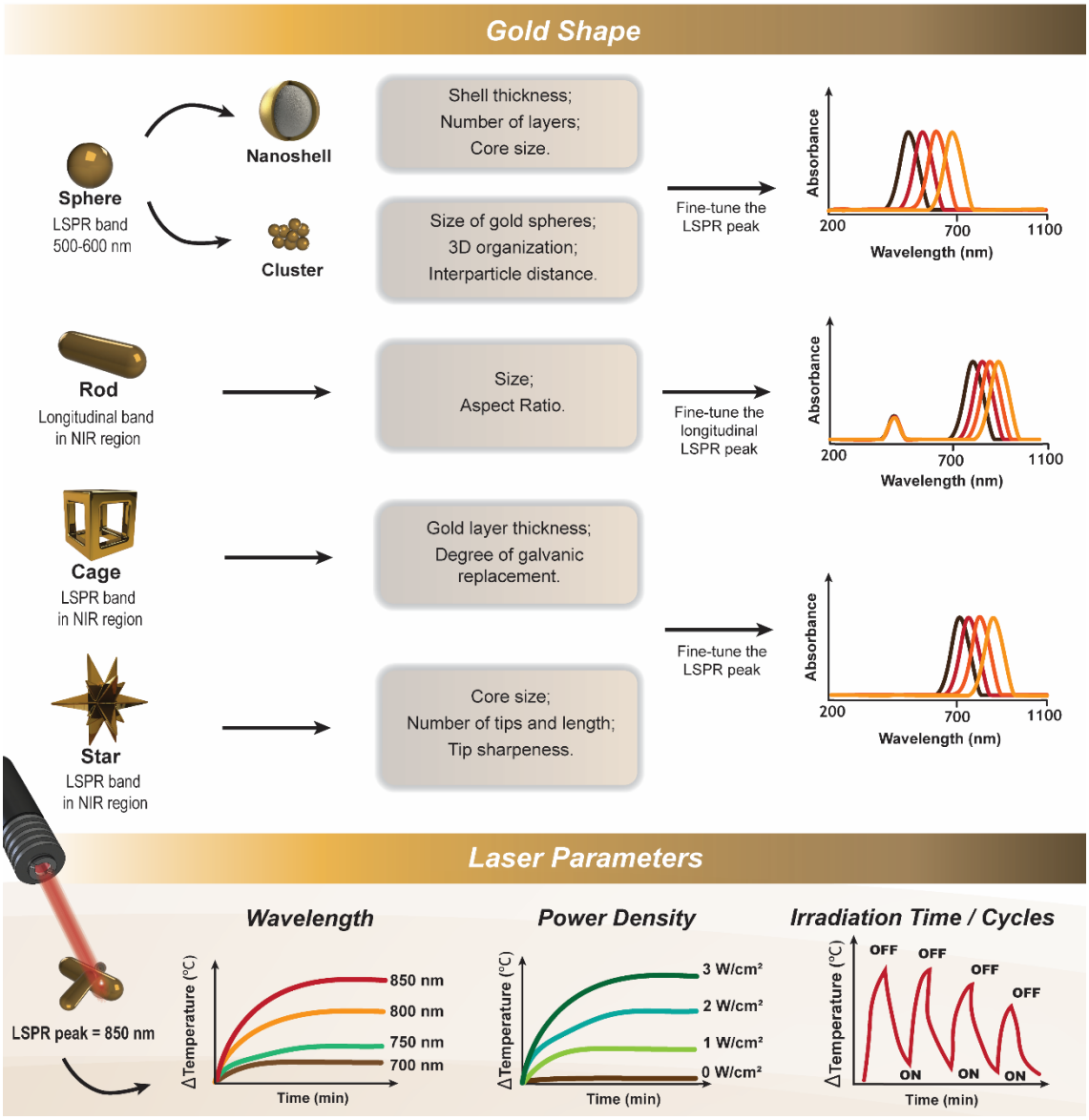

Figure 2: Representation of the main factors affecting the gold nanoparticles PTT performance. The light-to-heat conversion efficiency and consequently the thermal ablation is directly affected by the shape and size of gold nanoparticles as well as the laser irradiation parameters, such as power laser wavelength, power density, and irradiation time.

1.2.3. Optimization of the gold nanomaterials' size and shape

1.2.3.1. Nanostructures based on gold nanospheres

The gold nanoparticles are usually produced by promoting the nucleation of gold atoms upon the reduction of a gold source in the presence of stabilizing agents [84]. The gold spheres are originated when this reaction occurs under thermodynamically controlled conditions [85]. Nevertheless, the optimization of the gold nanospheres size only leads to slight changes in the LSPR absorption band, in the 500 to 600 nm region [86]. Alternatively, the organization of gold nanospheres as clusters or shells has demonstrated the ability to imprint in the nanosystem a PTT capacity [87, 88]. This change in the physical properties of the gold nanostructures is attributed to the

interactions of the near-field of one particle with the adjacent ones in close proximity promoting the coupling of the plasmon oscillations [89]. This phenomenon is more pronounced when the interparticle gaps are decreased, using smaller nanospheres or reduce the space between them [90].

1.2.3.1.1. Gold nanoclusters

The gold nanoclusters are formed by promoting the aggregation/coupling of gold nanospheres. Different strategies have been explored to mediate this process, such as the use of polymeric spacer-arms linking different particles, dendrimers/polymeric matrices encapsulating the gold nanospheres, large templates based on proteins, polymers, or DNA, and the utilization of organic solvents or small molecules to promote the aggregation of gold nanospheres [91-93]. Chegel *et al.* demonstrated that the organic compounds containing amine and thiol groups such as cysteamine, ethanolamine, and thiourea can promote the aggregation of citrate coated gold nanoparticles originating nanoclusters [94]. The produced single gold nanospheres presented a diameter of 10-15 nm and a single absorption peak at ≈520 nm. The authors observed that the increase of the thiourea concentration from 1 μM to 5 μM induced a decrease in the absorption peak at 520 nm with a concurrent appearance of a second broad absorption peak in the 660-800 nm region. The authors also recorded a similar behavior when cysteamine (5 μM) was added to the gold nanospheres, however, the shift in the absorption peak occurred only in 623-640 nm. Otherwise, only ethanolamine concentrations in the millimolar ranges induced alterations in the gold nanospheres absorption spectra, with the appearance of low intensity and a very broad shoulder in the range of 550-800 nm. Park and colleagues explored albumin to produce gold nanoclusters for the photothermal treatment of colon cancer [95]. The gold nanoclusters were produced through a desolvation process, incubating gold nanospheres (≈5 nm of diameter) with albumin, followed by glutaraldehyde-mediated crosslinking. The resulting gold nanocluster-loaded albumin nanoparticles (size 105-182 nm) showed a greater absorbance over the 600–900 nm region, contrasting with the single absorption peak at 520 nm of the gold nanospheres. Additionally, the authors observed the gold nanocluster-loaded albumin nanoparticles (200 $\mu g.mL^{-1}$) irradiation (808 nm, 1.5 $W.cm^{-2}$, for 10 min) could induce a temperature increase up to ≈70°C. This photothermal capacity rendered to the nanosystem the capacity to increase the tumor tissue temperature to values superior to 50°C (808 nm, 1.5 $W.cm^{-2}$, for 5 min), 6 h after the nanoparticle's injection via tail vein of HCT116 tumor-bearing mice. Further, the authors also reported that gold nanocluster-loaded albumin nanoparticles mediated the suppression of the tumor growth and the decrease of the tumor volume to 17.8 mm^3 on

day 20, contrasting with the ≈1,850 mm^3 registered in the control group (treated with phosphate-buffered saline (PBS)), without eliciting any significant damages on major organs. Similarly, Iodice and coworkers used poly(lactic-co-glycolic acid) (PLGA)-based nanoparticle for promoting the clustering of gold nanospheres with 6 nm in diameter [96]. With that in mind, the gold nanospheres were resuspended in a chloroform solution containing PLGA and allowed to dry. Then, the resulting film was dissolved in acetonitrile and added to an ethanol (EtOH) solution containing L-*α*-Phosphatidyl-DL-Glycerol and 1,2-Distearoyl-sn-Glycero-3-Phosphoethanolamine-N-Carboxy(Polyethylene glycol (PEI))-2000. These authors observed that the increase in the initial amount of gold nanospheres (25-150 μg) resulted in bigger nanoparticles (100-170 nm). Accordingly, the authors reported an overall enhancement of the nanoparticles absorbance along the spectra and higher initial concentrations of gold nanospheres resulted in a larger shift in the absorption peak of the nanoparticles, from 520 to 580 and 600 nm for the initial gold nanospheres amount of 100 and 150 μg, respectively. Moreover, upon irradiation with an 800 nm laser (fluence: 20 $J.cm^{-2}$, pulse width: 400 ms, pulse frequency: 1 Hz, during 1 min), the nanoparticles formed with 150 μg of gold nanospheres mediated an increase in the temperature of 20°C. Further, these authors also demonstrated that this photothermal capacity induced the death of breast cancer cells (SUM-159) as well as the almost complete ablation of tumor spheroids composed of glioblastoma multiforme cells (U87MG cells). Alternatively, Li *et al.* produced gold nanoclusters using1,9-nonanedithiol to promote the crosslinking of gold spheres (10 nm in diameter) previously modified with Cys-Arg-Gln-Ala-Gly-Phe-Ser-Leu-5-ALA (CRQAGFSL-5-ALA) and Cys-Arg-Gln-Ala-Gly-Phe-Ser-Leu-Cy5.5 (CRQAGFSL-Cy5.5) [97]. Then, PEGylated U11 targeting peptides were immobilized on the surface of the gold nanoclusters (≈53 nm in diameter). The authors reported that the 1,9-nonanedithiol-mediated aggregation of gold nanospheres provoked an increase in the absorbance in the NIR region (*i.e.* 700-800 nm) and a red-shift in the absorption peak from the 532 to 544 nm. Further, the gold nanoclusters irradiation with a NIR laser (750 nm, 2 $W.cm^{-2}$, for 5 min) induced a 30°C increase in the medium temperature, reaching a maximum of 50°C. Such photothermal capacity inhibited the growth of orthotopic pancreatic tumors (intravenous administration of nanoclusters at a dose of 2 pmol per mouse). Further, the authors observed the almost complete tumor eradication after 15 days when the PTT effect was combined with the 5-ALA action (photodynamic agent).

1.2.3.1.2. Gold nanoshells

The gold nanoshells, likewise the nanocluster, can present absorption in the NIR region of the spectra when different gold nanospheres are immobilized in proximity. Loo and

coworkers demonstrated that the gold nanoshells absorption spectra, in a predetermined inner core radius, is dependent on the shell thickness [98]. The authors produced gold nanoshells by grafting small gold seeds (1-3 nm) on the surface of amine-modified silica nanoparticles (60 nm in diameter). Then, the gold modified silica nanoparticles were incubated with a gold source ($HAuCl_4$) allowing the growth of the seeds and the formation of the gold nanoshell. The authors observed that the decrease in the gold nanoshell thickness from 20 to 10, 7, and 5 nm induced a red-shift in the absorption peak of the nanoparticles from ≈730 nm to ≈820, ≈910, and ≈1,020 nm, respectively. Similarly, Gao and colleagues reported the development of multilayered gold nanoshells by promoting the growth of small gold seeds (2 nm) attached on the surface of gold core organosilica shell nanospheres via gold-thiol interactions [99]. The multilayered gold nanoshells were composed of a spherical gold core with 50 nm in diameter, an organosilica layer with 30 nm, and an outer gold nanoshell with 20 nm. The authors reported that the formation of the gold nanoshells resulted in two absorption bands located in the 590 and 780 nm region, contrasting with the single absorption peak at 555 nm of the gold core organosilica shell nanospheres. Moreover, the authors observed that the size increase of the spherical gold core from 30 to 50, and 70 nm in diameter induces a red-shift on both absorption peaks, respectively to 560 and 760 nm, 590 and 790 nm, and 615 and 815 nm. Further, the photothermal experiments revealed that upon NIR laser irradiation (808 nm, 2 $W.cm^{-2}$, for 15 min), the multilayered gold nanoshells mediated the temperature increase up to 55°C. The assays performed in MDA-MB-231 breast cancer cells demonstrated that the PTT capacity of this multilayered gold nanoshells could promote the death of 90% of the cells and the increase in the tumor tissue temperature to ≈58°C upon intravenous administration (100 μL, 4 $mg.mL^{-1}$) in MDA-MB-231 tumor-bearing mice and NIR laser irradiation for 5 min. In turn, Luo *et al.* produced a gold nanoshell on the surface of chitosan-coated oleanolic acid liposomes for mediating chemo-photothermal antitumor therapy [100]. For that purpose, small gold seeds were produced via $NaBH_4$ reduction of gold salt and incubated with the previously formed chitosan-coated oleanolic acid liposomes. The attachment of the gold seeds occurred through the formation of Au-N bonds due to the amine groups available in the chitosan backbone. Then, the gold seeds modified liposomes were reacted with a growth solution containing $AuCl_3$ originating the gold nanoshell. The authors observed that the formation of the gold nanoshell rendered to the liposomes a broad absorption band between 600 and 850 nm, contrasting with the single absorption peak at 520 nm observed in the gold seeds modified liposomes. The authors explored this absorption capacity in the NIR region of the spectra to trigger the drug release, drug release of 92% and 69% at pH 5.5 and 7.4 after NIR laser irradiation (808 nm, 1 $W.cm^{-2}$, for 4 min)

whereas in the absence of NIR laser these values decreased to 80% and ≈55%, respectively. Moreover, the combined action of the photothermal effect and faster drug release resulted in an increased antitumoral effect. The authors reported that the size of U14 tumors in the groups treated with the gold nanoshells presented a slower growth, with 79.65% and 50% inhibition rate for the irradiated (daily NIR laser irradiation 808 nm, 1 $W.cm^{-2}$, for 4 min) and non-irradiated groups, respectively. Rastinehad and colleagues reported the clinical results of the application of silica core gold nanoshells (AuroShells®, 15 nm thickness gold shell) in the PTT of prostate tumors [101]. The authors observed that the AuroShells administration at a dose of 7.5 $mL.kg^{-1}$ (AuroShells concentration 4.8 $mg.mL^{-1}$) followed by the NIR laser irradiation (810 nm for 3 min) mediated the tumor ablation in 15 of 16 patients at 3 months, with 14 of 16 patients presenting the ablation zones negative for tumor after 12 months.

1.2.3.2. Gold nanorods

The rod-like shape of gold nanoparticles has been the standard for the application of the gold-based nanomaterials in PTT. This gold shape is usually produced using a seed-mediated growth methodology in the presence of a structure-directing agent [102]. In this process, small spherical gold spheres (*i.e.* seeds) are produced by using a strong reducing agent to promote the nucleation of gold atoms [103]. Subsequently, the gold seeds are added to a "growth solution", which is composed of gold salt (*e.g.* chloroauric acid), silver nitrate, and a stabilizing agent *(e.g.* cetyltrimethylammonium bromide-CTAB) inducing a rod-shaped growth [104]. The shape of gold nanorods renders to them two absorption bands in the electromagnetic field due to the specific LSPR phenomenon occurring in the two different dimensions of the nanorods (*i.e.* longitudinal and transversal axis) [105]. The LSPR phenomena of the nanorod's short axis correspond to the transverse plasmon resonance band, which leads to an absorption peak with lower intensity at 500-600 nm region. Otherwise, the longitudinal plasmon band that occurs along the major axis can be tuned to the NIR region of the spectra by optimizing the nanorods aspect ratio (A.R.) (*i.e.* rod length/width coefficient) [106]. Wang and colleagues demonstrated that increasing the gold nanorods A.R. mediated a red-shift in the longitudinal absorption peak [107]. The authors observed that the longitudinal absorption peaks occurred at 650, 760, 840, 920, 1,000 nm for gold nanorods with an A.R. of 2.2, 3.5, 4.1, 5.1, and 6.3, respectively. Further, apart from the A.R., the actual dimensions of gold nanorods also impact its absorption spectra and photothermal capacity [106]. The authors observed that by maintaining the A.R. (3.4-3.5) changes on the size of the nanorods (length and width) 38 × 11, 28 × 8, and 17 × 5 nm provoked shifts on the longitudinal absorption peak 740, 770, and 755 nm, respectively. Further, the authors also registered alterations on the nanorods

photothermal capacity upon irradiation with a NIR laser (808 nm, 5.8 $W.cm^{-2}$, for 2 min), when compared to the 38 × 11 and 17 × 5 nm nanorods, the photothermal-to-heat conversion efficiency of 28 × 8 nm gold nanorods was 2.05 and 1.40 times superior. Accordingly, the photothermal effect on HSC-3 cells was also superior in the 28 × 8 gold nanorods group, with a cell viability of 17% contrasting with the 100% and 29% recorded for the cells treated with 38 × 11 and 17 × 5 nm gold nanorods. Maestro *et al.* studied the light-to-heat conversion efficiency of gold nanorods with the longitudinal absorption peaks in the first (700-950 nm) and second NIR biological window (1,000-1,400 nm) [108]. The authors produced gold nanorods with 28 × 7 and 77 × 16 nm with longitudinal absorption peaks at 808 nm and 1,000 nm. The authors observed that the heating efficiency of gold nanorods with 28 × 7 nm was ≈40% superior to that of 77 × 16 nm gold nanorods. Further, the subcutaneous injection (5 µL, $1.0x10^{11}$ nanoparticles per mL) of gold nanorods in chicken breast tissues demonstrated the upon irradiation with NIR laser (808 or 1,090 nm, 1 $W.cm^{-2}$), the heating generated by the 28 × 7 nm gold nanorods (808 nm laser) is limited to the injected area, whereas the heating of 77 × 16 nm gold nanorods (1,090 nm laser) spread to adjacent tissues. Xu and co-workers functionalized gold nanorods with Anti-HER2 antibody-modified hyaluronic acid (HA)-containing hydrazide and thiol groups for the targeted PTT and photodynamic therapy (PDT) of breast cancer [109]. For this purpose, gold nanorods with 55 × 11 nm were prepared via the seed-mediated growth method and reacted with Anti-HER2 antibody-modified HA-containing hydrazide and thiol groups, exploring the gold-thiol affinity. Additionally, the authors incorporated 5-Aminolevulinic acid and Cy7.5 into the coated nanorods via hydrazone and amide linkages, respectively. The produced gold nanorod-based system presented a longitudinal absorption peak at 800 nm and upon irradiation with a NIR laser (20 $\mu g.mL^{-1}$, 808 nm, 2 $W.cm^{-2}$, for 10 min) mediated a temperature increase up to 55°C. Moreover, the authors reported that the intravenous administration of the gold nanorod-based system (0.2 mL at 1 $mg.mL^{-1}$) in breast cancer cell line (MCF-7) tumor-bearing mice mediated the increase in the tumor tissue temperature up to 60°C upon NIR laser irradiation (808 nm, 1 $W.cm^{-2}$, for 5 min). This photothermal effect slowed the tumor growth and when combined with the PDT, the tumors were eliminated without reoccurrence for 20 days.

1.2.3.3. Gold nanocages

Gold nanocages have a hollow quasi-cubic structure with porous walls and emerged as a novel plasmonic nanoparticle with excellent tunable optical properties [70, 110]. These gold-based nanoparticles are produced through the use of a galvanic replacement reaction between a silver nanocube template and a gold salt [111]. During this process, due to the different electrochemical potentials between these two metals, silver ions will

dissolve into the solution while simultaneously a thin layer of gold is being formed at the silver nanocube outer surface [112]. The thickness of the gold layer is adjusted according to the amount of gold source (*e.g.* $HAuCl_4$) added to the solution. With the extension of this reaction, the silver from the interior of the nanocube and the gold-silver alloy walls will be removed, forming the porous gold cage-like nanostructures. The LSPR peaks of gold nanocages can be adjusted to the NIR region by optimizing the thickness of the gold layer, *i.e.* adjusting the amount of gold source and the Ag/Au ratio. Panfilova *et al.* observed a red-shift in the gold nanocubes absorption peak with the increase of $HAuCl_4$ added to the silver nanocubes [113]. The addition of 0.1, 0.2, and 0.5 mL of $HAuCl_4$ (1 $mmol.L^{-1}$) provoked a shift in the absorption peak from 448 to 480, 500, and 700 nm, respectively. The authors also described changes in the structure of the nanocube, the addition of 0.1 mL of the $HAuCl_4$ solution resulted in the production of Au/Ag "alloy islands" and the increase to 0.2 mL promoted the transition of this nanostructures to nanoboxes, which progressed to hollow gold nanocages with the increase of $HAuCl_4$ solution to 0.5 mL. Similarly, Yang and colleagues also demonstrated that the addition of increasing volumes of $HAuCl_4$ solution (0.2, 0.4, 0.6, 0.8, 1.6, 1.8, 2.2, 4.0, and 6.0 mL at 0.5 mM) to silver nanocubes induce a gradual red-shift on the LSPR peak from 495 to 1,250 nm [114]. Moreover, the authors also observed that excessive amounts of $HAuCl_4$ (volumes superior to 6 mL) had a negative impact on the gold nanocubes absorption, registering a blueshift in the LSPR peak to 530 nm (Figure 3).

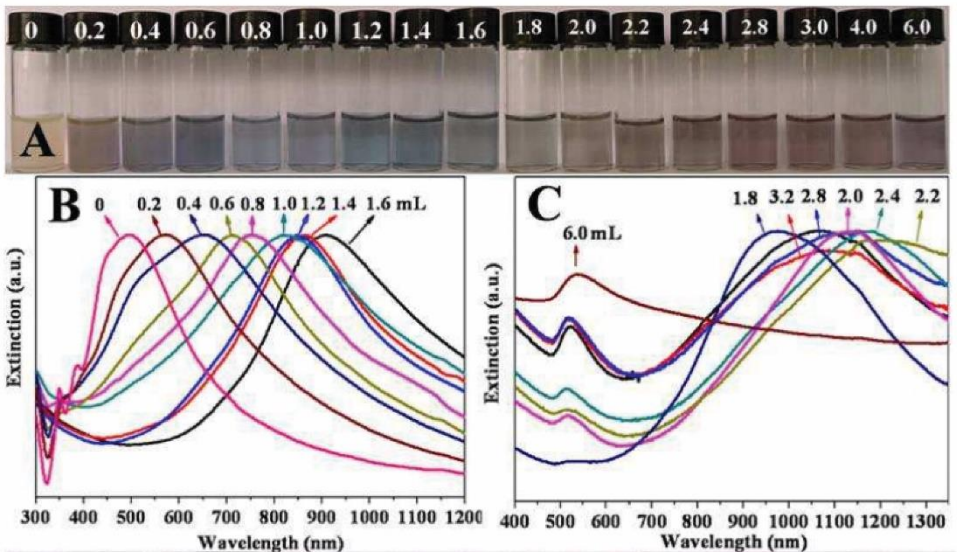

Figure 3: Characterization of the gold nanocubes absorption spectra. Photographs (A) and UV-Vis absorbance spectra (B) of the gold nanocubes solutions with increasing amounts (0.2-6.0 mL) of 0.5 Mm $HAuCl_4$ (Adapted from [114]).

Chen and co-workers developed gold nanocages combined with lauric acid (a phase-change material) for delivering selenous acid (precursor of selenite) in the combinatorial therapy of lung cancer [115]. For that purpose, the gold nanocages with 49 nm of edge length and 5.4 nm of wall thickness were produced using the conventional galvanic replacement process. Then, the hollow cavity of gold nanocages was loaded with lauric acid/selenous acid mixture. The gold nanocages presented the LSPR peak at 810 nm and induced a temperature increase to ≈75°C and ≈50°C upon irradiation with a NIR laser (808 nm, 4 min) at a power density of 0.8 $W.cm^{-2}$ and 0.4 $W.cm^{-2}$. The authors also demonstrated that this heat generation could prompt the release of selenous acid, the drug concentration increased from 7.5 $\mu g.mL^{-1}$ when incubated at 37°C to 27 and 72 $\mu g.mL^{-1}$ upon NIR laser irradiation at a power density of 0.4 $W.cm^{-2}$ and 0.8 $W.cm^{-2}$. Moreover, the photothermal effect mediated by the gold nanocubes upon NIR laser irradiation (808 nm, 0.8 $W.cm^{-2}$, for 10 min) mediated the decrease in the A549 tumor cells viability to values close to 58%, and when combined with the simultaneous selenous acid action the viability of A549 cells decreased to 31%.

1.2.3.4. Gold nanostars

The nanostars are another anisotropic gold nanostructure that is comprised of a small gold core and several gold tips. The gold nanostars are commonly produced using a seed-mediated method. This approach explores the reduction of a gold source (*e.g.* $HAuCl_4$) on small gold spheres in the presence of surfactant agents (*e.g.* CTAB and poly(N-vinylpyrrolidone)). The surfactant agents will direct the anisotropic growth of the tips of gold nanostars, additionally, silver nitrate can be added to the reaction increasing the control over the particle morphology [116, 117]. The LSPR phenomenon in gold nanostars is dependent on the core size as well as the tips dimension, number, and shape. In general, the gold nanostars LSPR peak red-shifts with the increase in the core size, number of tips, tip length, and sharpness [118]. Yuan and co-workers demonstrated that the increase of Ag^+ concentrations (5 μM, 10 μM, 20 μM, 30 μM) led to gold nanostars with an increased number of tips (4 to 10) as well as longer and sharper tips [116]. Accordingly, these morphological changes also impacted the gold nanostars LSPR absorption peak from 600 to 1,000 nm. Further, the authors showed that the shift in the LSPR absorption peak is related to the changes in the ratio between the length and base width of the tips, increased ratios result in the tuning of LSPR peaks to the NIR region. Additionally, the increase in the number of tips and its length as well as core size resulted in absorption peaks with higher intensity. Espinosa *et al.* also observed that an increase in the gold nanostars diameter (25, 55, 85, 120, and 150 nm) led to a red-shift on the LSPR absorption peak from 700 nm (25 nm gold nanostars) to 790, 800, 900, and 950 nm for the nanostars with 55, 85, 120, and 150 nm in diameter, respectively [119].

Further, the gold nanostars irradiation (808 nm, 1 W.cm^{-2}, for 10 min) induced a temperature increase of ≈18°C, ≈45°C, and ≈36°C for the 25, 85, and 150 nm nanoparticles. Li and colleagues produced polydopamine (PDA) coated gold nanostars for mediating the PTT of cervical cancer [120]. For that purpose, the gold nanostars were produced using the conventional seed-mediated method and then modified with thiolated PEI, gold-thiol affinity, and coated with PDA. The produced gold nanostars presented a mean diameter of 74 nm and the LSPR peak at 726 nm. The authors demonstrated that the gold nanostars (Au concentration 0.35 mM) upon NIR laser irradiation (808 nm, 1.3 W.cm^{-2}, for 5 min) could mediate a temperature increase up to 40.2°C with a light-to-heat conversion efficiency of 40%. Moreover, the intratumoral injection of the PDA coated gold nanostars (Au concentration 5.6 mM) mediated the increase of Human negroid cervix epithelioid carcinoma (HeLa) tumors to 58.7°C upon irradiation with NIR laser (808 nm, 1.3 W.cm^{-2}, for 10 min) promoting the complete ablation at 20 days posttreatment. Wang and coworkers developed Chlorin e6-PEG-functionalized gold nanostars to mediate the PDT and PTT treatment of breast cancer [121]. In this approach, the gold nanostars were initially modified with a thiol-terminated PEG, which was subsequently modified with Chlorin e6 via carbodiimide chemistry. The resulting gold nanostars presented a mean size of 54 nm and a LSPR absorption band at 670 nm. The authors observed that the irradiation of Chlorin e6-PEG-functionalized gold nanostars with a laser (671 nm, 2 W.cm^{-2}, for 10 min) could mediate a temperature increase up to 65°C as well as induce the generation of ROS. Further, the authors also demonstrated that the intratumoral injection of gold nanostars in MDA-MB-435 tumor-bearing mice could be explored to induce a 23°C increase in the tumor tissue temperature upon laser irradiation (671 nm, 1 W.cm^{-2}, for 6 min), which decreased the tumor growth during 14 days. Otherwise, the combinatorial treatment mediated by the Chlorin e6-PEG-functionalized gold nanostars significantly reduced the volume of MDA-MB-435 tumors being observed extensive cancer necrosis and a decreased oxygen saturation.

1.2.4. Gold-based nanohybrid materials

Apart from the optimization of the gold nanoparticles' size, morphology, and organization, these nanostructures can be combined with other materials to improve their therapeutic. Various multifunctional gold-based nanohybrid materials have been prepared to improve both the gold nanostructures PTT capacity as well as its stability and resistance to photodegradation (Figure 4).

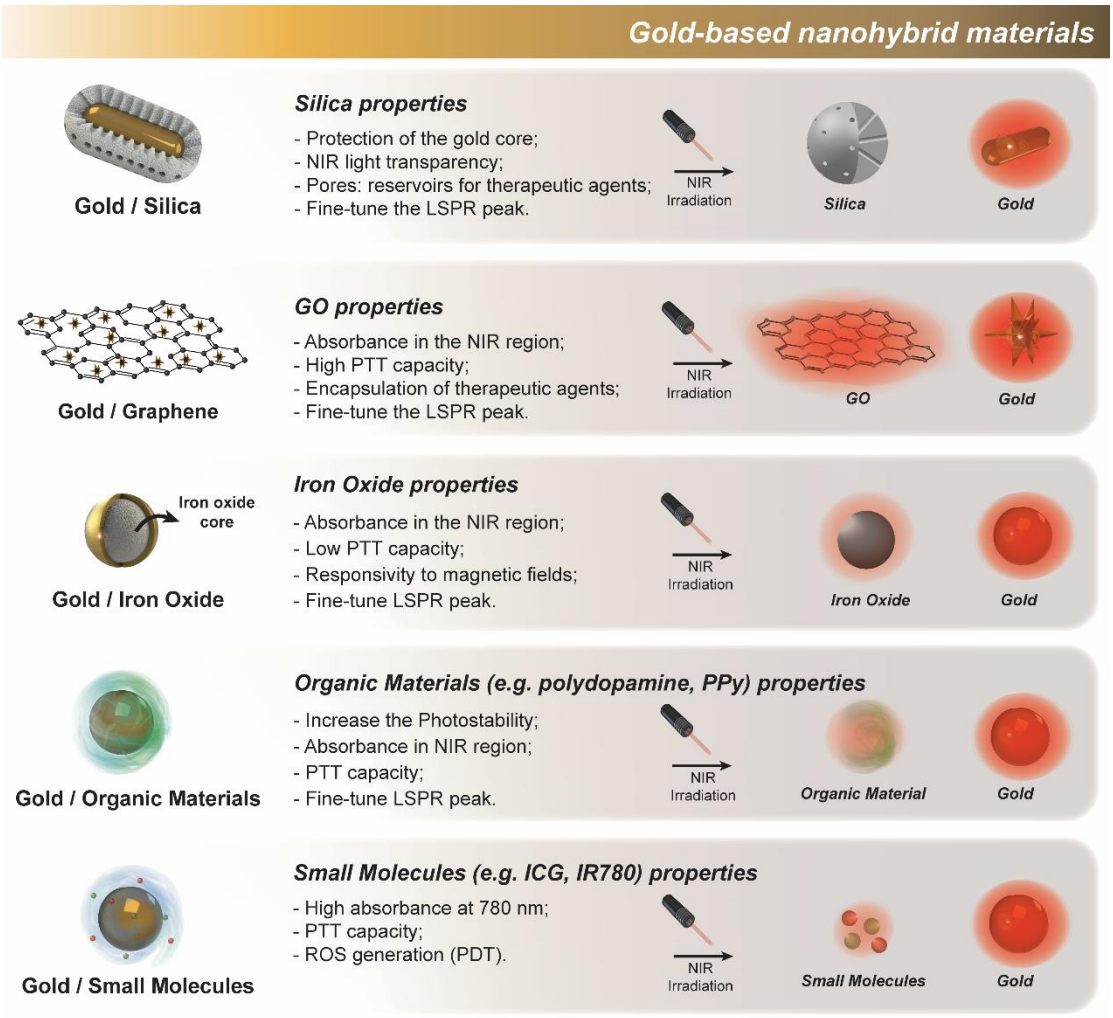

Figure 4: Representation of the main gold-based nanohybrid materials and their contribution to improving the PTT capacity of gold nanomaterials.

1.2.4.1. Gold-silica nanohybrids

The silica is a chemically inert and biocompatible material that can improve the colloidal stability of gold nanostructures [122]. The inclusion of silica derivatives, such as mesoporous silica, can also increase the drug loading capacity of gold nanoparticles [123]. Further, the silica NIR light transparency does not impact the excitation of gold cores during the PTT [124]. The modification of gold nanomaterials with silica can be performed using the conventional Stöber method or its derivations [125]. During this procedure, a silica shell is formed in the surface of the gold nanostructures by promoting the condensation of a silica precursor (*e.g.* tetraethyl orthosilicate) under alkaline conditions [51, 67, 85, 126]. The silica shell on gold nanostructures can be fine-tuned to optimize the LSPR peak wavelength and intensity of gold-silica nanohybrids. Fernandez-López and colleagues observed that the introduction of a silica shell in gold nanospheres results in a red-shift in the LSPR absorption peak [127]. The authors observed that the red-shift in the LSPR absorption peak was dependent on the size of the

gold nanosphere. The deposition of silica shells with 24 nm in thickness resulted in a ≈33 nm shift in the absorption peak, from ≈680 to ≈713 nm, for gold nanospheres with 142.8 nm in diameter, whereas in gold nanospheres with 98.5 nm and 60.4 nm the red-shift in the absorption peak was 10 and 8 nm, respectively. Similarly, Zhang and co-workers reported a red-shift on the longitudinal LSPR peak of gold nanorods with the formation of a silica shell [128]. The authors observed that the growth of a silica shell on the surface of gold nanorods induced a ≈10 nm red-shift in the longitudinal LSPR peak (from 799 to 813 nm) when the silica thickness reached the 7 nm. The further growth of the silica shell to 14 nm provoked an additional 10 nm shift in the longitudinal LSPR peak to 823 nm (Figure 5).

Furthermore, Khlebtsov *et al.* reported that the increase in the shell thickness of silica-coated gold nanocages from 10 to 120 nm impact both the LSPR peak wavelength and magnitude [129]. The authors observed the red-shift in the LSPR peak with the increase of the silica shell thickness, *e.g.* from 775 to 802 nm with a 20 nm shell thickness, as well as a gradual increase in the LSPR maxima.

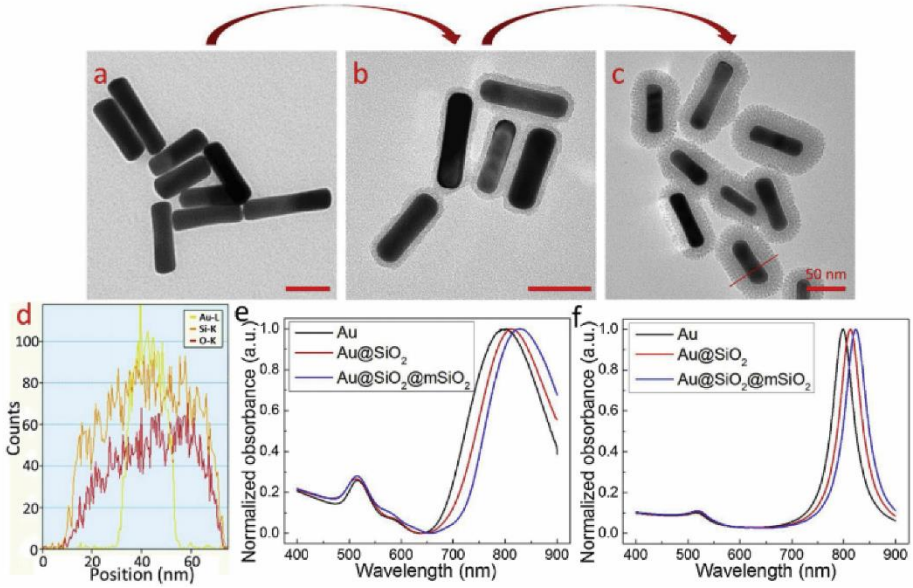

Figure 5: Physicochemical characterization of gold nanorods, Au@SiO_2, and Au@SiO_2@mSiO_2 nanoparticles. Transmission electron microscopy (TEM) images of gold nanorods (a), Au@SiO_2 (b), and Au@SiO_2@mSiO_2 (c); EDX analysis (d); Nanoparticles UV-Vis absorbance spectra and respective LSPR peak changes with silica coating (e); Corresponding extinction spectra calculated by FDTD (f) (Adapted from [128]).

Otherwise, the silica shell also protects the gold nanomaterials from photodegradation phenomena. The gold nanostructures exposition to high energetic radiations and high temperatures has been associated with the reshaping of the nanoparticles and loss of the NIR absorption capacity. Nevertheless, Chen and colleagues observed that the coating of

gold nanorods with a silica shell enhances the thermal stability of the nanoparticles [130]. The authors observed that the gold nanorods irradiation with 300 laser pulses of 7 ns duration at fluences superior to 4 $mJ.cm^{-2}$ resulted in alterations in the longitudinal LSPR peak, 10% amplitude decrease in 800 nm region upon irradiation at 8 $mJ.cm^{-2}$ and a strong increase of the absorption in the 600–650 nm range at higher fluences. These changes on the gold nanorods absorption spectra were consistent with the particle reshaping, namely the rounding of gold nanorods. However, the absorption spectra of silica-coated gold nanorods with a shell thickness of 20 nm remained constant, with the authors observing small changes, a 10% decrease in the 800 nm region, only when the silica-coated gold nanorods were irradiated at 20 $mJ.cm^{-2}$.

1.2.4.2. Gold-graphene nanohybrids

Graphene oxide (GO) a single-atom-thick layer of sp^2 hybridized carbon atoms and can be composed of different oxygen-containing groups (*e.g.*, hydroxyl, and epoxy groups) in the edges and base of its aromatic structure [131]. The GO, particularly the reduced GO, present the capacity to absorb in the NIR region, which enables their application in PTT [132]. Therefore, the combination of gold nanoparticles with graphene materials can improve the NIR absorption of nanomaterials, and consequently their photothermal and bioimaging potential (*e.g.* fluoresce imaging, PAI, Raman Imaging). Xu and co-workers produced nano GO-modified gold nanorods functionalized with HA to mediate the delivery of doxorubicin (DOX) and the PTT of liver cancer [133]. For that purpose, the authors produced carboxylated nanosized GO through the modified Hummer's method and exfoliation processes. Then, gold nanorods with a 3.8 A.R. (3.1±8.2 and 13.8±3.2 nm) were modified with the nanosized GO via electrostatic interactions. The resulting gold-graphene nanohybrids were further functionalized with HA exploring the carbodiimide coupling chemistry between the carboxyl groups on GO and amine groups of HA. The authors reported that the GO-modified gold nanorods functionalized with HA despite presenting the GO characteristic absorption peak at 239 nm also displayed a significant enhancement in the intensity of the absorption band at the 760-800 nm region. This improvement in the nanomaterials absorption capacity resulted in an enhanced photothermal effect with the gold-graphene nanohybrids inducing an increase in the solution temperature to ≈65°C upon NIR laser irradiation (808 nm, 4 $W.cm^{-2}$, for 3 min), whereas the bare gold nanorods only reached the ≈59°C [133]. Additionally, the authors observed that the photothermal treatment mediated by the HA-functionalized gold-graphene nanohybrids (808 nm, 1 $W.cm^{-2}$, for 5 min) induced the death of 22% of the Huh-7 cancer cells, which increased when combined with the simultaneous delivery of DOX inducing the death of 82% of the cells. Similarly, Turcheniuk *et al.* also modified gold nanorods with GO nanosheets to improve the PTT of glioblastoma [134]. The gold-

graphene nanohybrids were produced by exploring electrostatic interactions between the positively charged gold nanorods (A.R. 3.8) and carboxylated nanosized GO and then modified via carbodiimide chemistry with an amine-modified PEG. The authors observed that the GO nanosheets attachment in the gold nanorods led to a red-shift in the longitudinal LSPR peak from 807 to 814 nm as well as an increase in the peak maximum absorbance. Moreover, the authors reported that the irradiation (808 nm, 0.5 $W.cm^{-2}$, for 10 min) of PEGylated gold-graphene nanohybrids resulted in a temperature increase to 60°C, whereas the gold nanorods only reached the ≈50°C. Additionally, the *in vivo* studies also revealed that the tail vein administration of Tat-targeted PEGylated gold-graphene nanohybrids could be explored to mediate the increase in the temperature of U87MG tumors to 52.5°C after NIR laser irradiation (808 nm, 0.7 $W.cm^{-2}$, for 10 min). Such resulted in the size reduction of the tumors from 500 mm^3 to ≈250 mm^3, contrasting with the 1,750 mm^3 observed in the control group. Wu and colleagues combined gold nanostars with GO for mediating the delivery of Chlorin e6 and the PTT of breast cancer [135]. In this approach, the GO nanosheets were used as supports for the gold nucleation and growth of the gold nanostars. Then, the gold-graphene nanohybrids were functionalized with athiol-terminated PEG by exploring the gold-thiol affinity. The resulting nanostructures presented an increased absorbance in the NIR region of the spectra, broad absorption peak at 600 to 900 nm region. The enhanced NIR absorption rendered to the gold-graphene nanohybrids a superior photothermal potential prompting the temperature increase up to 75°C upon laser irradiation (660 nm, 2 $W.cm^{-2}$, for 8 min), whereas the gold nanorods and the GO nanosheets only reached the ≈65°C and ≈47°C, respectively (Figure 6). Similar data were observed in the *in vivo* studies with the intratumoral administration of PEGylated gold-graphene nanohybrids mediating the temperature increase of EMT6 tumors to 60°C upon laser irradiation (660 nm, 3 $W.cm^{-2}$, for 10 min), which stalled the tumor growth and when combined with the simultaneous action of Chlorin e6 promoted the tumor eradication.

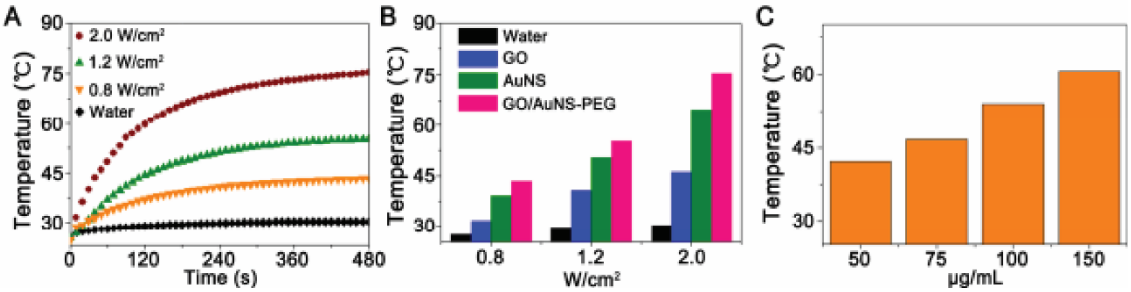

Figure 6: Characterization of the GO/AuNS-PEG/Ce6 nanoparticles photothermal capacity. Temperature variation curves of GO/AuNS-PEG/Ce6 under the exposure to the 660 nm laser with different power densities, during 8 min (A); Maximum temperature reached by AuNS, GO, and GO/AuNS-PEG/Ce6 under the exposure to the 660 nm laser with different power densities (B); Maximum temperature registered for GO/AuNS-PEG/Ce6 nanoparticles at different concentrations under 660 nm laser radiation at 2.0 W.cm^{-2} for 8 min (C) (Adapted from [135]).

1.2.4.3. Gold-iron oxide nanohybrids

Iron oxide (IO) nanomaterials due to its plasmonic properties can also mediate a photothermal effect in response to NIR laser irradiation. These nanomaterials can be found in different chemical compositions, such as maghemite (Fe_2O_3), magnetite (Fe_3O_4), or non-stoichiometric combinations of Fe and O [136-138]. Nevertheless, when compared to gold nanomaterials, the IO nanomaterials demand higher energies to induce the excitation of free electrons, which is associated with the higher free electron density [139]. However, the production of gold-IO nanohybrids can be explored both to improve the PTT capacity of the nanomaterials and imprint a responsivity to magnetic fields that can enhance the tumor accumulation. Bai *et al.* produced hollow gold nanospheres with IO nanoparticles immobilized on its surface for mediating both the imaging and PTT of cervical cancer [140]. For that purpose, dimercaptosuccinic acid-modified IO nanoparticles were attached to the surface of the hollow gold nanospheres exploring the gold thiol-affinity. Additionally, this gold-IO nanohybrid was functionalized with polyvinylpyrrolidone and folic acid to confer stability and targeting capacity, respectively. The authors observed that the introduction of IO nanoparticles results in a red-shift in the hollow gold nanospheres LSPR peak, from 800 to 830 nm. Further, these gold-IO nanohybrids were able to induce a temperature increase up to 63.4°C, whereas a gold nanorod (AR: 3.5) control group only reached 56.3°C. Liang and co-workers developed a PEGylated IO-core gold shell nanohybrids for the PTT treatment of breast cancer [141]. For that purpose, poly(acrylic acid)-coated IO nanoparticles were stabilized with poly(allylamine hydrochloride) and then mixed with small gold nanoseeds. Subsequently, the seeds were grown to a gold nanoshell by promoting the reduction of gold salt ($HAuCl_4$) and modified with lipoic-acid-terminated PEG via gold-thiol linkages. The authors observed that the gold-IO nanohybrids presented a significant enhancement of the absorbance in the NIR region of the spectra, 0.88 *vs.* 0.1

of IO nanoparticles. Accordingly, the nanohybrid materials induced a superior temperature increase upon irradiation with NIR laser (808 nm, 0.5 W.cm^{-2}, for 10 min), 55°C and 39°C maximum temperature for the gold-IO nanohybrids and IO nanoparticles respectively (Figure 7). Moreover, the authors also reported that the intratumoral injection of gold-IO nanohybrids could mediate the temperature increase of breast tumors up to 52°C upon NIR laser irradiation (808 nm, 0.5 W.cm^{-2}, for 10 min) improving the mice survival.

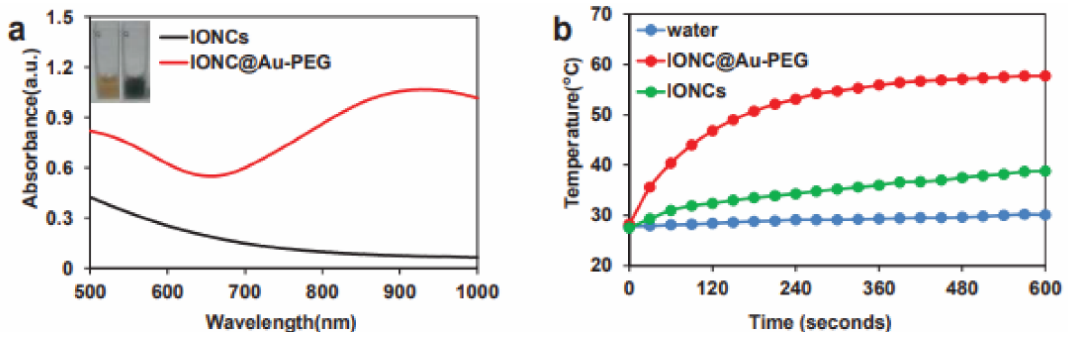

Figure 7: Optical and photothermal characterization of PEGylated gold-IO nanohybrids (IONC@Au-PEG). IONC@Au-PEG and IONCs UV-Vis absorbance spectra (a); Temperature variation curves of IONCs, and IONC@Au-PEG nanoparticles under exposure to the 808 nm laser, 0.5 W.cm^{-2} for 10 min (Adapted from [141]).

1.2.4.4. Other gold-based nanohybrids

The development of more efficient photothermal agents can also be achieved by combining the gold nanostructures with organic materials. Nam and colleagues coated gold nanostars with PDA to mediate the DOX delivery and the PTT of colon carcinoma [142]. The authors observed that the gold nanostars functionalization with PDA induced a red-shift in the absorption spectra in a concentration-dependent manner. The absorption peak for gold-PDA hybrids shifted from ≈780 nm to 815, 840, and 860 nm for dopamine concentrations of 0.1, 0.2, and 0.3 mg.mL^{-1}, respectively. The authors also reported that the inclusion of PDA increases the photostability of the gold nanostars since no significant alterations in the relative absorbance at 808 nm were observed in the nanohybrid materials after irradiation with a NIR laser (808 nm, 10 W.cm^{-2}, for 30 min), whereas the gold nanostars presented a ≈70% reduction of the relative absorbance. Further, the gold nanohybrid materials mediated a temperature increase superior to 80°C after NIR laser irradiation (808 nm, 10 W.cm^{-2}, for 30 min) contrasting with 40°C obtained for the gold nanostars. The authors also demonstrated that the intratumoral injection of gold nanohybrid materials followed by NIR laser irradiation (808 nm, 1 W.cm^{-2}, for 5 min) could induce a 13°C increase in the temperature of CT26 tumors followed by tumor regression, with complete tumor eradication in 40% of the animals.

Hu *et al.* produced a PEGylated polypyrrole (PPy)-gold nanohybrid to improve PPT of breast tumors [143]. For that purpose, PEI-PPy nanoparticles were produced using $FeCl_3$ as the oxidant to initiate the pyrrole monomer polymerization process. Then, these nanoparticles were PEGylated via carbodiimide chemistry (NH_2 groups of PEI and COOH terminated mPEG) and small gold spheres were grown in the interior of the PPy nanoparticles by promoting the *in situ* reduction of $HAuCl_4$. The authors revealed that the inclusion of the gold spheres enhanced the light-to-heat conversion efficiency from 35.3% to 37.1%. Accordingly, the PEGylated PPy-gold nanohybrids mediated a temperature increase to 55.6°C upon NIR laser irradiation (808 nm, 1.5 $W.cm^{-2}$, for 10 min), even after 5 cycles of irradiation, which contrasts with the 45.4°C obtained for the PPy nanoparticles. Further, the authors reported an enhancement of the 4T1 cancer cells PTT, the 4T1 cancer cells treated with the PPy-gold nanohybrids or PPy nanoparticles presented cell viability of 25.2% and 34.9%, respectively, after NIR irradiation.

Otherwise, the introduction of other metals in the gold nanomaterials can also result in an enhanced photothermal capacity. Leng *et al.* reported a red-shift in the longitudinal LSPR peak of gold nanorods (A.R. 4.2) from 770 to 803 nm as well as an increase in the light-to-heat efficiency from 39% to 56% after the gold nanorods coating with a layer of copper sulfide [144]. Further, the authors also demonstrated that the gold-copper nanohybrids present increased photothermal stability, mediating the temperature increase up to 60°C even after four irradiation cycles (808 nm, 0.9 $W.cm^{-2}$, for 10 min) whereas the gold nanorods exhibited a 20% decrease in the temperature elevation (from 52.5°C to 47°C) after the irradiation cycles. Similar results were reported by Kumar and co-workers after the coating of gold bipyramids with molybdenum disulfide via electrostatic interactions [145]. The gold-molybdenum nanohybrids presented a red-shift in the longitudinal LSPR from 791 to 837 nm as well as an increase in the absorption maxima. Such improved the photothermal capacity of the gold bipyramids, registering a temperature increase up to 60.3°C, 50.6°C, and 55.6°C for the gold-molybdenum nanohybrids, molybdenum disulfide, and gold bipyramids, respectively, upon NIR laser irradiation (808 nm, 2 $W.cm^{-2}$, for 10 min). The authors also observed that the coating of gold bipyramids with molybdenum disulfide improved the PTT against HeLa cells. The NIR laser irradiation (808 nm, 2 $W.cm^{-2}$, for 3 cycles of 10 min) resulted in the decrease of HeLa cells' viability to 46.2% and 21.6% for the cells treated with gold bipyramids and gold-molybdenum nanohybrids, respectively.

1.2.5. Incorporation of small molecules with photothermal capacity

Among the different strategies explored to improve the cancer PTT mediated by the gold nanomaterials, the encapsulation of NIR responsive small molecules have been

displaying promising results (Table 1). In this regard, ICG and heptamethine cyanines (*e.g*. IR780) are the most explored molecules to enhance the optical properties of gold nanostructures, and consequently its photothermal potential.

The ICG is a dye approved by the Food and Drugs Administration for clinical fluorescence imaging, such as angiography [146]. Additionally, this molecule presents a high absorbance at 780 nm and a good light-to-heat conversion efficiency [147]. Further, ICG can also mediate the generation of reactive oxygen species (ROS) in response to NIR laser irradiation [148]. Higbee-Dempsey *et al.* produced small gold nanoclusters consisting of 2 nm gold cores coated with dodecanethiol loaded with ICG to mediate the PTT and photoacoustic imaging of triple-negative breast cancer [149]. For that purpose, the authors explored the amphiphilic nature of ICG to drive the self-assembly of the hydrophobic 2 nm gold cores in spheroid nanostructures with ≈61 nm in diameter. The authors observed that the gold nanoclusters only present a slight red-shift in the LSPR absorption peak, whereas ICG loaded gold nanoclusters displayed a strong absorption in the 780 nm region, which is in agreement with the ICG absorption spectra. Additionally, the irradiation of the ICG-loaded gold nanoclusters with a NIR laser (808 nm, 1.2 $W.cm^{-2}$, for 10 min) was able to induce a temperature increase up to 70°C, whereas the free ICG solutions only reached the 45°C. Further, the authors noticed that the free ICG showed a rapid loss of its heating capacity with multiple laser irradiations (2-3 cycles), while the ICG-loaded gold clusters maintained its photothermal capacity. Such photothermal capacity was also confirmed in mice bearing 4T1 tumors after intravenous administration of ICG-loaded gold clusters induced the increase of tumors temperature up to 52.3°C after NIR laser irradiation (808 nm, 0.7 $W.cm^{-2}$ for 30 min) contrasting with the 45.6°C obtained in the free ICG treated group. Accordingly, the ICG-loaded gold clusters PTT induced the regression of the 4T1 tumors until day 11 with the complete remission of the primary tumor in two out of five mice. Otherwise, free ICG treatment only slowed tumor growth without any significant changes in mice survival. Chen and colleagues produced bovine serum albumin (BSA) stabilized gold nanostars loaded with ICG to mediate the PTT of glioma [150]. The gold nanostars loading was achieved by promoting the ICG adsorption in the surface of the nanoparticles followed by the addition of BSA. The produced gold nanostars presented an LSPR peak at 680 nm, which suffered a red-shift to 712 nm and also a pronounced absorption at 780 nm characteristic of ICG. The authors reported that the ICG-nanostars combination results in a more effective light-to-heat conversion efficiency and increased photostability, reaching the 63°C upon NIR laser irradiation (808 nm, 1 $W.cm^{-2}$ for 5 min). Otherwise, the free ICG and BSA stabilized gold nanostars only reached 41°C and 59°C, respectively. Additionally, the authors also demonstrated that this photothermal capacity can be

explored to mediate the photothermal ablation of U87 glioma cells, 85.1% and 94.2% of cell death for gold nanostars and ICG-loaded gold nanostar after NIR laser irradiation (808 nm, 1 $W.cm^{-2}$ for 5 min).

The heptamethine cyanines (*e.g.* IR780) in general present superior optical (*e.g.* higher molar extinction coefficient at 780 nm) and therapeutic capabilities, when compared to ICG [151]. Nevertheless, the application of these molecules in the clinic is hindered by its hydrophobic character, acute toxicity, and photodegradation, which can be surpassed by promoting the heptamethine cyanines encapsulation in nanoparticles such as gold nanomaterials [152]. Nagy-Simon *et al.* prepared pluronic coated gold nanospheres loaded with IR780 for being applied in the colon carcinoma PTT [153]. The authors observed that apart from the characteristic LSPR peak of gold nanospheres at 522 nm, the IR780-pluronic coated gold nanospheres also presented a second absorption peak at 780 nm due to the IR780. Further, the IR780-pluronic coated gold nanospheres irradiation (785 nm, 170 mW for 6 min) induce a temperature increase of 9°C, whereas the free IR780 suffered photodegradation after 2.5 min of irradiation reaching a final temperature variation of ≈2°C. Similarly, Xia and co-workers developed IR780-loaded gold nanostars functionalized with BSA and matrix metalloproteinases polypeptides (Ac-GPLGIAGQ) for the PTT and PDT of lung cancer [154]. The IR780 loading was physically adsorbed onto the functionalized gold nanostars via hydrophobic interactions. The authors observed that the gold nanostars presented the LSPR peak in the 700-800 nm region and after the loading of IR780 the absorption in this region of the spectra increased being noticed the characteristic absorption peak at 780 nm (Figure 8). Upon irradiation with a NIR laser (808 nm, 0.8 $W.cm^{-2}$, for 5 min), the IR780-loaded gold nanostars mediated the temperature increase to 63°C, whereas the gold nanostars alone only reached the 58.5°C. The authors confirmed the PTT potential on A549 tumor-bearing mice after the intravenous administration of functionalized with BSA and Ac-GPLGIAGQ, observing the increase in the tumor tissue temperature to 46°C after NIR laser irradiation (808 nm, 0.8 $W.cm^{-2}$, for 5 min), which resulted in the reduction of the tumor volume during 18 days.

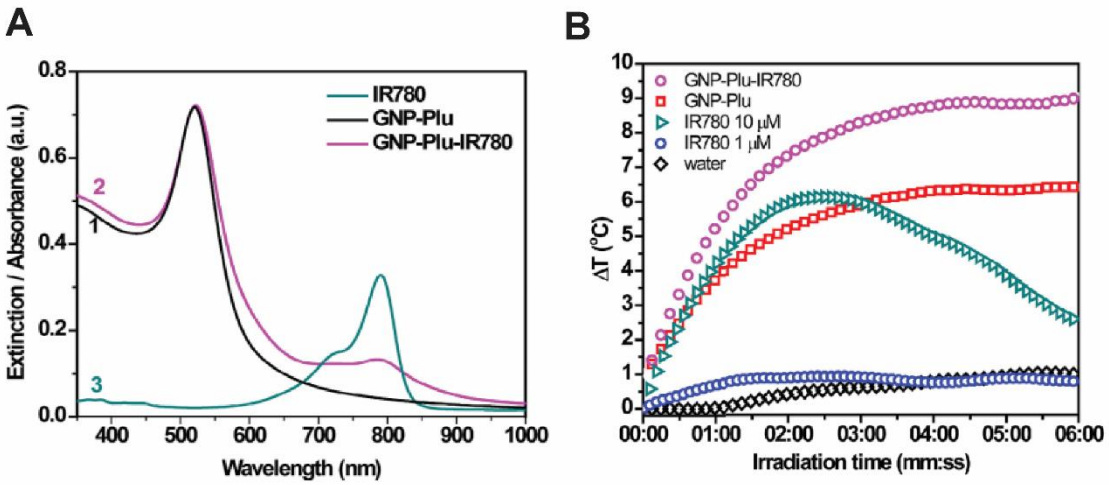

Figure 8: Optical and photothermal characterization of GNP-Plu and GNP-Plu-IR780 nanoparticles. UV–Vis absorbance of GNP-Plu (1), GNP-Plu-IR780 (2), and IR780 (3) (A); Temperature variation curves of GNP-Plu-IR780, GNP-Plu, and free IR780 at different concentrations under the exposure of the 785 nm laser at 170 mW for 6 min (B) (Adapted from [153]).

Table 1: Application of NIR responsive small molecules that have been explored to improve the photothermal capacity of gold-based nanomaterials (N.D. – non disclosed, N.A. – not applicable, L: length; W: width).

Small molecules	Gold Shape	Size	Surface Modification	LSPR peak (nm)	Photothermal Effect		Type of Study	Test Model	Main Results	Ref.
					Laser Parameters	Temperature				
ICG	Nanoclusters	mPEG-PLGA nanocapsules loaded with gold nanoparticles and ICG	BSA, RGD peptides, and mPEG–PLGA, Poly(vinyl alcohol), poly (acrylic acid)	700-850	808 nm, 1.0 W.cm^{-2}, 5 min	ΔT≈25°C	*In vitro*	U87-MG cells	The PTT effect mediated by the nanocapsules loaded with gold nanoparticles and ICG induced the reduction of the viability of U87-MG cells to 35%.	[155]
	Nanoclusters	61.22 nm gold nanoclusters (gold nanoclusters ≈2 nm) coated with ICG	N.A.	803 nm	808 nm, 1.2 W, 7 min	≈60°C	*In vitro/In vivo*	4T1 cells/4T1 tumor-bearing mice	The ICG/gold nanoclusters mediated a ≈15°C increase in the temperature of 4T1 tumors, whereas the tumors treated with free ICG only presented a ΔT ≈5°C. Further, the ICG/gold nanoclusters treatment induced the reduction of the tumor volume until day 8 followed by the tumor re-growth until day 20.	[149]
	Nanoclusters	3.4 nm gold nanoclusters loaded with ICG molecules	Glutathione	≈700 and 800 nm	808 nm, 0.5 W.cm^{-2}, 5 min	ΔT≈20°C	*In vitro/In vivo*	MCF-7/MCF-7 tumor-bearing mice	The PTT effect mediated by the gold/ICG nanostructures increased the temperature of the MCF-7 tumor to 55°C, whereas the free ICG only reached ≈40°C. Further, this combinatorial treatment resulted in the complete elimination of MCF-7 tumors in 14 days.	[156]
	Nanostar	80 nm gold nanostar (70 nm) with ICG adsorbed in the surface	BSA	712 and 780 nm	808 nm, 1.0 W.cm^{-2}, 0-6 min	63.9°C	*In vitro*	U87 cells	The PTT effect of gold nanostar reduced the U87 cell viability to 15%, which combined with the ICG reached 5% of cell viability.	[150]

Nanostar	Gold nanostar (96 nm) loaded with ICG	$CaCO_3$	800-900 nm	808 nm, 1.0 $W.cm^{-2}$, 6 min	≈60°C	*In vitro/In vivo*	MGC803 cells/MGC80 tumor bearing mice	The PTT effect mediated by the gold/ICG nanomaterials induced the increase of the MGC80 tumors' temperature to ≈43°C, which mediated the reduction of the tumor volume during 20 days.	[157]
Nanocluster	ICG loaded gold nanocluster	BSA and HA	700 nm	808 nm, 1.5 $W.cm^{-2}$, 2 min	N.D.	*In vitro/In vivo*	4T1 cells/4T1 tumor-bearing mice	The PTT effect of the gold/ICG nanostructures promoted a 15°C increase in the temperature of the 4T1 tumor, which induced the decrease of the tumor volume during 10 days followed by the tumor re-growth until day 12. Otherwise, the single treatment with free ICG or gold nanoclusters only slowed the growth of 4T1 tumors.	[158]
Nanoshell	151.1 nm hollow gold nanoshell (125.3 nm) loaded with ICG	Gadolinium and BSA	Broad absorbance from 700 to 900 nm	808 nm, 1.5 $W.cm^{-2}$, 5 min	≈60°C	*In vitro/In vivo*	4T1 cells/4T1 tumor-bearing mice	The 4T1 tumors treated with gold/ICG nanostructures registered a temperature increase up to ≈57°C, whereas the administration of free ICG or gold nanoshell only reached ≈48°C. This photothermal improvement resulted in a decrease in the 4T1 tumors' volume during 21 days.	[159]
Nanorod	Nanosctrure with≈103 nm comprised of molybdenum coated with gold nanorods (L:50 nm, width:14 nm, A.R.:3.5) and ICG	PEG	788 nm	808 nm, 0.2 $W.cm^{-2}$, 5 min	57°C	*In vitro/In vivo*	HeLa cells/HeLa tumor-bearing mice	The gold nanorod/molybdenum/ICG nanohybrid led to higher tumor weight reduction followed by gold nanorod/molybdenum, free ICG, gold nanorod, and molybdenum alone.	[160]

	Nanorod	ICG loaded silica (shell:17.34–32.43-nm) coated gold nanorod (L:47.23 nm, W:13.56 nm, A.R:3.50)	Mesoporous silica, $tLyp^{-1}$ peptide and PEG	754 nm	785 nm, 3 $W.cm^{-2}$, 5 min	≈60°C	*In vitro*	MDA-MB-231 cells	The PTT effect mediated by the G/ICG nanostructures provoked the reduction of the viability of MDA-MB-231 cells to values inferior to 20%.	[160]
	Nanorod	ICG loaded silica (shell:21 nm) coated gold nanorod (L:57.3; W:16.2; A.R:3.47)	β-CD, RLA-Ada and (DMA CS(DMA)-PEG	813 nm	808 nm, 2 $W.cm^{-2}$, 5 min	≈60°C	*In vitro/In vivo*	MCF-7 cells/MCF-7 tumor bearing mice	The MCF-7 tumors treated with G/ICG nanostructures registered a temperature increase up to ≈45°C, whereas the administration of free ICG only reached ≈38°C. This photothermal improvement resulted in a decrease in the volume of MCF-7 tumors during 21 days, whereas the free ICG only slowed the tumor growth.	[161]
	Nanocluster	31.97 nm ICG loaded gold nanoclusters (3.57 nm spheres)	BSA	760 nm	808 nm, 0.8 $W.cm^{-2}$, 4 min	≈60°C	*In vitro/In vivo*	4T1 cells/4T1 tumor-bearing mice	The PTT effect mediated by the gold/ICG nanostructures increased the temperature of the 4T1 tumor to 53°C, whereas the free ICG only reached ≈46°C. Further, this combinatorial treatment resulted in the complete elimination of 4T1 tumors in 24 days without recurrence, whereas the free ICG only slowed the tumor growth.	[162]
IR780	Nanostar	121.5 nm IR780-loaded gold nanostar (80 nm)	BSA and metalloproteinases (MMP2) polypeptides	Broad absorbance from 600 to 1,000 nm	808 nm, 0.8 $W.cm^{-2}$, 2 min	≈60°C	*In vitro/In vivo*	A549 cells/A549 tumor bearing mice	The A549 tumors treated with gold/IR780 nanostructures registered a temperature increase up to ≈46°C, whereas the administration of free ICG only reached ≈41°C. This photothermal improvement resulted in a decrease in the	[154]

									A549 tumors' volume during 18 days, whereas the free ICG only slowed the tumor growth.	
	Nanosphere	30 nm gold nanosphere loaded with IR780	Pluronic F127	522 and 780 nm	785 nm, 170 mW, 30 min	ΔT≈9°C	*In vitro*	C26 cells	The combinatorial treatment mediated by the gold/IR780 nanostructures presented a higher number of C26 dead cells than the treatment with free ICG.	[153]
	Nanoprism	Ir780 loaded on gold nanoprisms surface (57.5 nm)	Lyp-1 and PEG	600-700 nm	660 nm, 1 $W.cm^{-2}$, 5 min	≈50°C	*In vitro/In vivo*	MDA-MB-231 cells/MDA-MB-231 tumor bearing mice	The MDA-MB-231 tumors treated with gold-IR nanostructures registered a temperature increase up to ≈50°C mediating the decrease of the tumor volume with the complete tumor ablation in 2 of the 5 animals.	[163]
Heptamethine cyanine dye	Nanorod	L:48.5; W:10.7 heptamethine cyanine dye coated gold nanorod	Glutathione	843 nm	808 nm; 1.5 $W.cm^{-2}$, 5 min	≈50°C	*In vitro/In vivo*	A549 cells/A549 tumor bearing mice	The PTT effect mediated by the gold/heptamethine cyanine dye nanostructures increased the temperature of the A549 tumor to 60°C promoting the complete tumor ablation in 16 days.	[164]

1.2.6. Biocompatibility of gold-based nanomaterials

The wide application of gold-based nanomaterials in biomedical applications raises some human safety concerns, which highlights the necessity to better understand their interaction with the human body. In this regard, several studies are currently being performed to evaluate the biodistribution and circulation of gold nanoparticles in the bloodstream, their pharmacokinetics and elimination from the organism, as well as any possible toxicity, *i.e.* adverse side effects to the organism as a whole or at the cellular and genomic level. It is worth to notice that several parameters affect the interaction of gold nanomaterials with the human body, such as size, shape, charge, and surface chemistry (reviewed in detail by [165-168] (Figure 9). In a typical synthesis of gold nanorods and other gold-based nanomaterials, the highly cytotoxic CTAB molecules are used as a stabilizing agent impacting its applicability in humans [169]. Therefore, the biocompatibility of these gold nanomaterials is ensured by replacing the CTAB molecules with non-toxic materials such as PEG [170], chitosan [171], albumin [172], silica [173]. Manivasagan and colleagues reported that the silica-core gold shells functionalized with chitosan and lipoic acid where biocompatible at concentrations up to 250 $\mu g.mL^{-1}$ (*i.e.* cell viabilities superior to 95%), whereas a notorious decrease in the viability of MDA-MB-231 cells was observed at concentrations superior to 150 $\mu g.mL^{-1}$ [174]. Zhang *et al.* evaluated the toxicity responses of mice subjected to the intraperitoneal injection of Albumin or GSH coated gold nanoclusters at a concentration up to 7.55 $mg.kg^{-1}$ [175]. The obtained results revealed that after 24 h no significant statistical differences were observed in the bodyweight of the mice as well as no pathological lesions in major organs were detected.

Nevertheless, the authors demonstrated that after 24 h the high dose of gold nanoclusters induces acute immune responses (*i.e.* thymus index values increased from 2.3 to 4.2 in the treated groups), increases the blood levels of white blood cells and creatine as well as affects the kidney function. Interestingly, these toxicity responses were almost completely reverted in the GSH coated gold nanoclusters after 28 days, which was attributed to the faster metabolism and renal clearance of this nanomaterial. Otherwise, the surface passivation of the gold nanomaterials can also enhance its colloidal stability and increase the blood circulation time [176, 177]. Xu and coworkers observed that the PEGylation of gold-core silica shell nanorods increased the blood circulation half-life from 1.8 to 9.2 h [178]. Similarly, Xie *et al.* reported that the PEGylation of gold nanoshells also increased the blood circulation half-life from 0.54 to 12.76 h [179]. Further, the authors also observed that increasing the blood circulation half-life resulted in an enhanced tumor uptake from 0.15 to 0.77%ID/g.

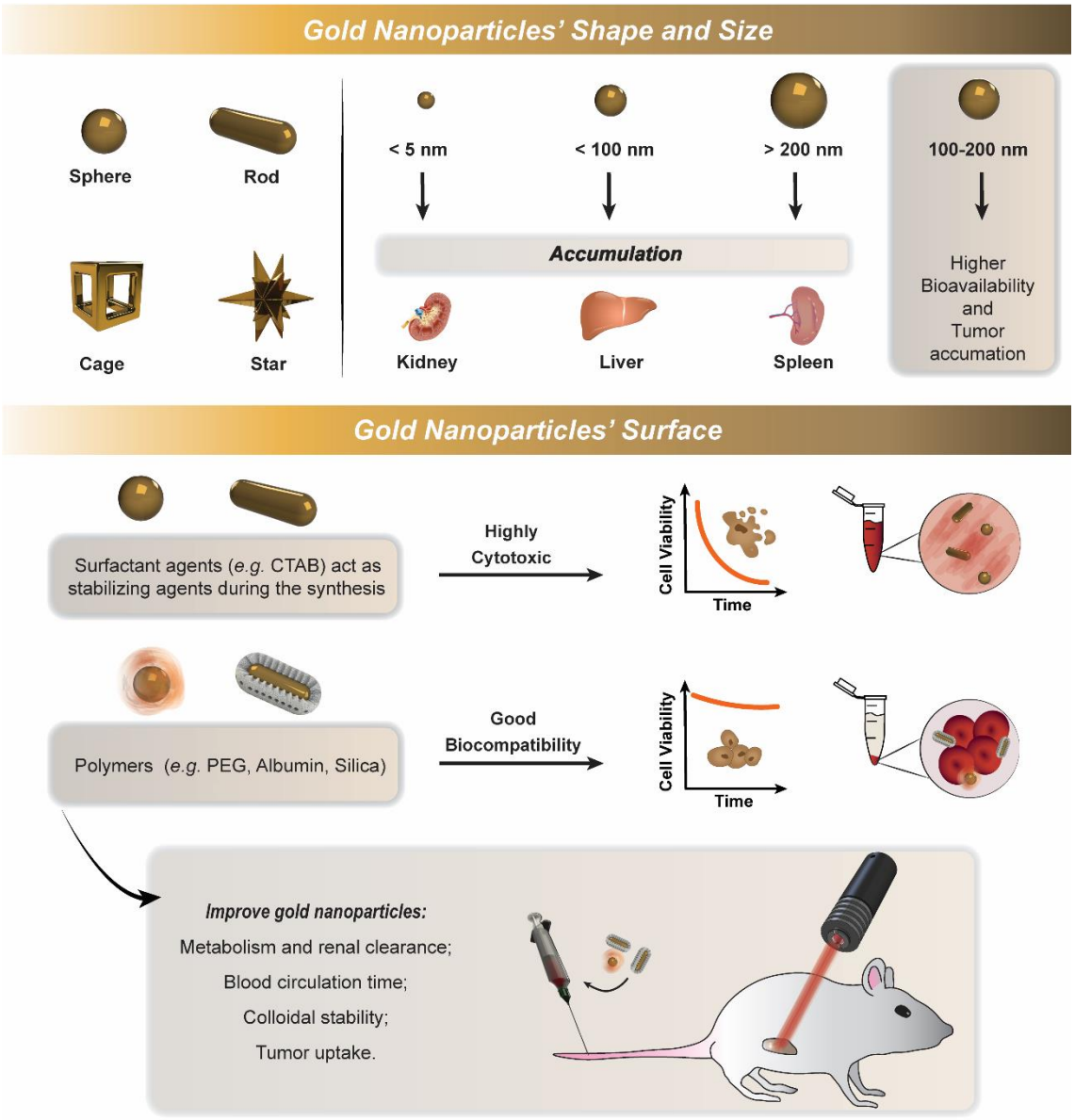

Figure 9: Representation of the main factors that affect gold nanoparticles biocompatibility and safety.

Aims

The main objective of this dissertation was to design and develop a novel surface functionalization for gold core silica shell (AuMSS) nanorods. Simultaneously, the encapsulation of IR780 in AuMSS nanoparticles was also aimed to increase the photothermal and photodynamic capacity, and consequently its therapeutic potential. The surface functionalization of AuMSS nanorods with Poly(ethylene glycol) methyl ether (PEG-CH_3) and Gelatin (GEL) was explored to improve both the blood circulation time and targeting towards the cancer cells. To accomplish that, PEG-CH_3 and GEL were previously modified with 3-(Triethoxysilyl)propyl isocyanate (TESPIC) (T-PEG-CH_3 and T-GEL) and then were used to functionalize AuMSS nanorods, originating the AuMSS/T-PEG-CH_3/T-GEL nanorods. Additionally, the IR780 was loaded in the pores of the mesoporous silica shell.

The specific aims of this dissertation were:

- Synthesize the T-GEL and T-PEG-CH_3 derivatives;
- Synthesize and functionalize the AuMSS nanorods;
- Characterize the nanoparticles' physicochemical properties;
- Evaluate the IR780 loading capacity;
- Determine the AuMSS nanoformulations' photothermal capacity;
- Evaluate the AuMSS nanoformulations' cytocompatibility;
- Characterize the nanoparticles' cellular uptake;
- Evaluate the nanoparticles' cytotoxic activity (PTT and PDT) in cervical cancer cells.

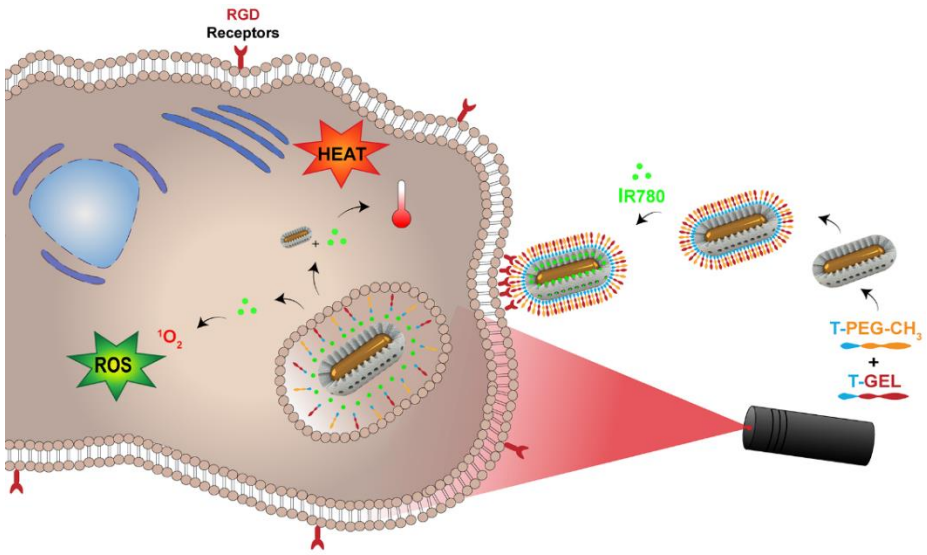

Figure 10: Schematic representation of IR780@AuMSS/T-PEG-CH_3/T-GEL assembly and its application in cancer phototherapy.

Chapter 2

Experimental Section

2. Experimental Section

2.1. Materials

Hydrogen tetrachloroaurate (III) hydrate ($HAuCl_4$) was purchased from Alfa Aesar (Karlsruhe, Germany). Tetraethylorthosilicate (TEOS) and tetrahydrofuran (THF) were obtained from Acros Organics (Geel, Belgium). CTAB was acquired from Tokyo Chemical Industry (Tokyo, Japan). Hydrochloric acid (HCl) was acquired from Panreac (Barcelona, Spain). Methanol was obtained from VWR International (Carnaxide, Portugal). L-ascorbic acid, silver nitrate ($AgNO_3$), Dulbecco's Modified Eagle medium-high glucose (DMEM-HG), Dulbecco's Modified Eagle Medium/Nutrient Mixture F-12 (DMEM-F12), ethanol (EtOH), Fluorescein 5-isothiocyanate (FITC), resazurin, sodium borohydride ($NaBH_4$), Paraformaldehyde (PFA), PBS solution, PEG-CH_3 (Mw=223.35 $g.mol^{-1}$), TESPIC, GEL, IR780 iodide,2',7'-Dichlorofluorescein diacetate (H_2DCF-DA) and trypsin were bought from Sigma-Aldrich (Sintra, Portugal). Hoechst 33342®, calcein acetozxmethyl (Calcein AM), Propidium iodide (PI), and wheat germ agglutinin conjugate Alexa 594® (WGA-Alexa® Fluor 594) were obtained from Invitrogen (Carlsbad, CA). Human negroid cervix epithelioid carcinoma HeLa cells (ATCCs CCL-2™) were acquired from ATCC (Middlesex, UK). Primary normal human dermal fibroblast (FibH) cells were bought to Promocell (Heidelberg, Germany). Fetal bovine serum (FBS) was acquired to Biochrom AG (Berlin, Germany). Cell imaging plates were acquired from Ibidi GmbH (Ibidi, Munich, Germany). Cell culture t-flasks were supplied by Orange Scientific (Braine-l'Alleud, Belgium). Double deionized and filtered water (ultrapure water) was obtained by using a Milli-Q Advantage A10 Ultrapure Water Purification System (0.22 μm filtered; 18.2 $M\Omega.cm^{-1}$ at 25°C)

2.2. Methods

2.2.1. Synthesis of AuMSS nanorods

The rod-shaped gold nanoparticles were synthesized through a seed-mediated growth methodology, as previously described in the literature [67, 126]. In the first step, a solution containing small spherical gold spheres (seeds) was prepared by adding 0.6 mL of $NaBH_4$ (0.01 M) to an aqueous solution containing 5 mL of CTAB (0.20 M) and 5 mL of $HAuCl_4$ (0.0005 M). After 6 h at 30°C, the seed solution was added to a growth solution, which was prepared by adding under magnetic stirring 0.21 mL of L-ascorbic acid (0.08 M), 0.03 mL of $AgNO_3$ (0.1 M), and 0.3 mL $HAuCl_4$ (0.05 M) to an aqueous solution containing 20 mL of CTAB (0.2 M). The final solution was left under magnetic stirring at 30°C for 16 h, to obtain the gold nanorods.

Then, the synthesis of the mesoporous silica shell was performed according to a method previously described in the literature [180]. For that purpose, the gold nanorods were centrifuged (12,000 g, 20 min at 25°C) to remove the excess of CTAB and resuspended in ultrapure water. Subsequently, 0.7 mL of CTAB (0.01 M) was added and the resultant solution was left under stirring overnight at 40°C. Afterward, 0.07 mL of NaOH (0.1 M) was added to the solution and left under stirring for 30 min. After this period, three injections of TEOS (0.03 mL at 20% v/v in methanol) were performed in 30 min intervals. Finally, the solution was left under stirring at 40°C for 24 h and the AuMSS nanorods were recovered by centrifugation (12,000 g for 20 min at 25°C) and washed several times with ultrapure water.

2.2.2. Removal of the surfactant template

The cytotoxic surfactant CTAB used in the synthesis of AuMSS nanorods was removed from the nanoparticles by adapting a solvent-based approach, previously described by Moreira and co-workers [181]. Briefly, nanoparticles were resuspended in an acid solution (HCl 7.5% v/v in EtOH), sonicated for 5 min, and centrifuged (18,000 g, 20 min at 25°C). This step was repeated numerous times and was followed by additional washing cycles with EtOH (99,9% v/v) and ultrapure water. Finally, AuMSS nanorods were recovered by centrifugation (18,000 g for 15 min) and resuspended in ultrapure water.

2.2.3. Synthesis of T-PEG-CH_3 and T-GEL

The TESPIC-PEG-CH_3 (T-PEG-CH_3) and TESPIC-GEL (T-GEL) polymers were synthesized by adapting a method described by Rodrigues and co-workers [67]. Briefly, 0.5 g of PEG-CH_3 polymer were dissolved in 20 mL of THF anhydrous, whereas 0.5 g of GEL were dissolved in 20 mL of THF (40% v/v). Both reactions were left at room temperature under a nitrogen atmosphere and magnetic stirring for 6 h. Next, TESPIC was added in a molar ratio of 1:1 for PEG-CH_3 and 2:1 for GEL and left under magnetic stirring for 24 h. Afterward, the T-PEG-CH_3 and T-GEL polymers were recovered by evaporation (Rotavap®R-215, Büchi, Switzerland), and the film obtained was resuspended with ultrapure water, sonicated, and freeze-dried.

The successful synthesis of the polymers TESPIC derivatives was accessed using the Fourier-transform infrared (FTIR) spectroscopy.

2.2.4. AuMSS nanorods functionalization with T-PEG-CH_3 and T-GEL

The polymer silanated derivatives, T-PEG-CH_3 and T-GEL, were chemically coupled to the surface of AuMSS nanorods through condensation reaction [67] (Figure 11). First, 20 mg of AuMSS nanorods were resuspended in 40 mL of EtOH (33%, pH 4) and sonicated

for 10 min. Then, T-PEG-CH_3 and T-GEL polymers were added to the AuMSS nanorods solution with a T-PEG-CH_3/T-GEL ratio of 3:1 (w/w) and left under stirring at 900 rpm for 24 h. Finally, the AuMSS/T-PEG-CH_3/T-GEL nanorods were recovered by centrifugation (8,000 g, 20 min at 25°C) and washed several times with ultrapure water to remove the unlinked polymers chains.

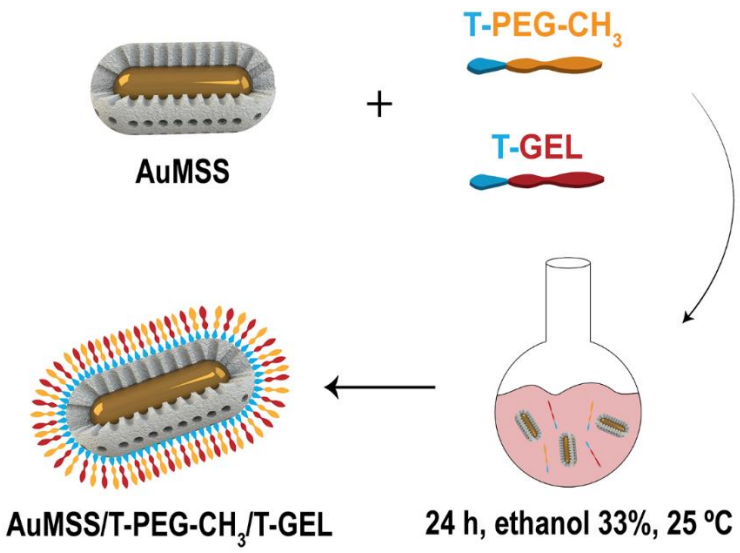

Figure 11: Representation of the AuMSS nanorods' functionalization with T-PEG-CH_3 and T-GEL polymers.

2.2.5. Characterization of nanocarriers physicochemical properties

2.2.5.1. Morphological characterization and size analysis

The morphology of the AuMSS and AuMSS/T-PEG-CH_3/T-GEL nanoparticles was evaluated by TEM (TEM-Hitachi-HT7700, Tokyo, Japan). Briefly, nanoparticles samples were placed in formvar-coated copper grids and were left to dry at room temperature. The TEM images were obtained at an accelerating voltage of 80 and 200 kV. Further, the silica shell thickness and nanoparticles' total size and gold core size were measured by software (Image J 2.0.0 NIH Image, USA).

2.2.5.2. Zeta potential and Ultraviolet-visible spectroscopy analysis

The zeta potential of AuMSS nanorods, AuMSS/T-PEG-CH_3/T-GEL, and AuMSS/T-PEG-CH_3/T-GEL loaded with IR780 (IR780@T-PEG-CH_3/T-GEL) was measured using a Zetasizer Nano ZS equipment (Malvern Instruments, Worcestershire, United Kingdom). The measurements were performed in ultrapure water at 25°C in a disposable capillary cell.

To confirm the success of AuMSS nanoformulations' synthesis and NIR absorption capacity a UV-Vis spectrum was assessed using a UV-Vis spectrophotometer (Thermo

Scientific Evolution™ 201, Bio UV-Vis Spectrophotometer, ThermoFisher Scientific Inc, USA) with a wavelength range between 300 to 1,100 nm at a scan rate of 300 nm/min.

2.2.5.3. Fourier transform infrared spectroscopy analysis

The successful purification and functionalization of AuMSS nanorods were evaluated through FTIR. The nanoformulations' FTIR spectra were obtained by using a Nicolet iS10 spectrometer with a 4 cm^{-1} spectral resolution from 600 to 4,000 nm (Thermo Scientific Inc (Massachusetts, USA). The Data acquired were executed in the OMNIC spectra software (Thermo Scientific).

2.2.5.4. Thermogravimetric analysis

The T-PEG-CH_3 and T-GEL content on AuMSS nanorods was measured by performing a thermogravimetric analysis (TGA) of AuMSS and AuMSS/T-PEG-CH_3/T-GEL nanoparticles. For that propose, samples were subjected to increasing temperatures up to 600 ^{o}C (rate of 10^{o}C/min under an inert atmosphere) and the nanoparticles' weight loss was recorded along the time using an SDT Q600 equipment (TA Instruments, USA).

2.2.6. The IR780 loading on AuMSS/T-PEG-CH_3/T-GEL

IR780 was loaded on AuMSS and AuMSS/T-PEG-CH_3/T-GEL nanorods by adapting an impregnation method described by Moreira and co-workers [182]. For that propose, AuMSS formulations were resuspended in 5 ml of methanol containing IR780 at a concentration of 40 μg.mL^{-1}. The solution was sonicated for 15 min with subsequent stirring for 48 h at room temperature. Afterward, the IR780 loaded AuMSS formulations (IR780@AuMSS and IR780@AuMSS/T-PEG-CH_3/T-GEL) were recovered by centrifugation (18,000 g for 30 min at 4°C) and freeze-dried. The obtained supernatant was used to determine the amount of IR780 that was encapsulated in AuMSS formulations. For that purpose, the absorption of the supernatant at 780 nm was measured using a UV-Vis Spectrophotometer (Thermo Scientific Evolution™ 201 Bio-UV spectrophotometer, ThermoFisher Scientific Inc., USA), and the IR780 content determined using a calibration curve (ABS=0,3929C + 0,0201, R^2=0,9978).

The encapsulation efficiency (E.E.) was calculated through equation 1:

$$\text{E.E. (\%)} = \frac{\text{(Initial IR780 weight-IR780 weight in the supernatant)}}{\text{Initial IR780 weight}} \times 100 \quad \text{(Eq. 1)}$$

2.2.7. *In vitro* photothermal measurements

The *in vitro* photothermal capacity of AuMSS formulations and free IR780 was evaluated as previously reported in the literature [180]. Briefly, free IR780 (1.3 μg.mL^{-1}), AuMSS,

AuMSS/T-PEG-CH_3/T-GEL, and IR780@AuMSS/T-PEG-CH_3/T-GEL nanorods at a concentration of 100 μg.mL^{-1} were irradiated with a NIR laser (808 nm, 1.7 W.cm^{-2}). During the procedure, the variation of the solution temperature was measured at different time points (from 1 up to 10 min) by using a thermocouple sensor with an accuracy of 0.1°C. A control group without the particles and IR780 was also irradiated and the temperature changes measured. Additionally, the photothermal capacity of AuMSS formulations and free IR780 after multiple irradiations was also measured at different points (from 1 up to 5 min).

The photothermal conversion efficiency of AuMSS formulations and free IR780 was calculated through equation 2:

$$\eta = \frac{hS(Tmáx-Tsol.amb)-Qdis}{I(1-10^{-}A808)} \text{ (Eq. 2)}$$

, where h is the heat transfer coefficient, S is the surface area of the container, T_{max} is the maximum temperature reached by the solutions, $T_{sol.amb}$ is the room temperature, I the intensity of the NIR, and A_{808} laser is the absorbance of the AuMSS nanorods at 808 nm [183]. The value of *hS* is obtained from equation 3:

$$hS = \frac{m \times C}{\tau s} \text{ (Eq. 3)}$$

, where m is the water mass (0.2 g), C is the specific heat capacity of water (4.2 J/g °C), τs is the sample system time constant. This constant is determined through the following equation:

$$\tau s = -\frac{t}{\ln(\theta)} \text{ (Eq. 4)}$$

, where t is the time of irradiation of the sample (600 s) and θ is calculated through the equation 5:

$$\theta = \frac{Tamb-Tsol.amb}{Tmáx-Tsol.amb} \text{ (Eq. 5)}$$

, where T_{amb} corresponds to room temperature (22.8°C).

2.2.8. Cytocompatibility assay

The biocompatibility of AuMSS and AuMSS/T-PEG-CH_3/T-GEL nanorods towards HeLa (cervical cancer cell model) and FibH (Human fibroblasts) cells was determined through the resazurin-based assay [181]. Briefly, both cells lines were seeded (10,000 cells/well) into 96-well flat-bottom culture plates and cultured with 100 μL of medium

(DMEM-HG for HeLa cells and DMEM-F12 medium for FibH cells) in an incubator with a humidified atmosphere (37°C, 5% CO_2) during 24 h. Posteriorly, cells were incubated with different concentrations (25 to 200 μg.mL^{-1}) of AuMSS formulations. After 24, 48, and 72 h, the medium was replaced with 110 μL of resazurin solution 10% (v/v) and incubated for 4 h in the dark at 37°C and 5% CO_2. After this time, the cells' viability was determined by measuring the fluorescence of the produced resorufin using a microwell plate reader (Spectramax Gemini XS, Molecular Devices LCC, USA) at an excitation/emission wavelength of λex=560 nm and λem=590 nm. Cells incubated with EtOH (99,9%) and cells only incubated with culture medium were used as positive (K^+) and negative (K^-) controls, respectively.

2.2.9. Evaluation of AuMSS nanoformulations' cellular uptake

The uptake of AuMSS and AuMSS/T-PEG-CH_3/T-GEL nanorods by HeLa or FibH cells was determined by fluorescence spectroscopy according to a method described by Moreira and co-workers [51]. Briefly, HeLa or FibH cells were seeded into 96-well flat-bottom culture plates at a density of 10,000 cells per well and cultured for 24 h, at 37°C, 5% CO_2 humidified atmosphere. After this period, the culture media was removed, and the cells were incubated with FITC stained AuMSS nanoformulations at a concentration of 100 and 200 μg.mL^{-1} for 2 h. In one test group, the cells were previously treated with GEL (200 μg.mL^{-1}) for 4 h. Then, the cells were washed with ice-cold Krebs Ringer Buffer (KRB) and lysed with 1% Triton X-100 in KRB for 30 min at 37°C. Cells incubated only with KRB were used as control. Afterward, FTIC fluorescence (λex=490 nm and λem=520 nm), was quantified using a Spectramax Gemini XS (Molecular Devices LCC, USA).

Additionally, the internalization of AuMSS nanoformulations by HeLa cells was confirmed by confocal laser scanning microscopy (CLSM) [184]. Briefly, HeLa cells were seeded on μ-Slide 8 well Ibidi imaging plates with a cell density of 20,000 cells per well and incubated for 24 h, at 37°C, 5% CO_2 humidified atmosphere. After this time, the medium was removed, and cells were incubated with FITC stained AuMSS nanoformulation at a concentration of 200 μg.mL^{-1}. After 6 h, the cells were washed with PBS, fixed with PFA (4% w/v) for 10 min, and washed again with PBS. Then, cells were treated with Hoechst 33342® and WGA-Alexa Flour 594 for cell nucleus and cytoplasm staining, respectively. The CLSM images were obtained using a Zeiss LSM 710 Confocal microscope (Carl Zeiss SMT Inc., Germany). The image analysis was performed in the Zeiss Zen 2010 software.

2.2.10. Evaluation of intracellular ROS generation

The generation of intracellular ROS was assessed using the H_2DCF-DA probe, as described by Dias and colleagues [180]. Initially, HeLa cells were seeded in 96-well plates with a cell density of 10,000 cells per well and cultured for 24 h, at 37°C, and 5% CO_2 humidified atmosphere. Then, cells were incubated with nanoparticles (100 and 200 $\mu g.mL^{-1}$) during 4 h. Subsequently, the cell medium was removed, and 10 mM of the H_2DCF-DA solution was added in the dark (at 37°C, a humidified atmosphere with 5% CO_2). After 1 h of incubation with the H_2DCF-DA probe, the cells were washed twice with PBS and fresh medium (phenol red-free). Cells cultured only with culture medium were used as the control group. Then, the cells were irradiated with a NIR laser (808 nm, 1.7 $W.cm^{-2}$) for 5 min, washed with ice-cold KBR, and lysed with 1% Triton X-100 in KRB for 30 min at 37°C. Finally, H_2DCF-DA fluorescence, λex=488 nm and λem=540 nm, was quantified using a Spectramax Gemini XS plate reader (Molecular Devices LLC, USA).

2.2.11. Evaluation of AuMSS nanoformulations phototherapeutic effect

2.2.11.1. Characterization of the AuMSS *in vitro* cytotoxic activity

The cytotoxic effect of free IR780 and AuMSS nanoformulations (AuMSS, AuMSS/T-PEG-CH_3/T-GEL, and IR780@AuMSS/T-PEG-CH_3/T-GEL) was determined *in vitro* using the resazurin assay [51]. For that propose 10,000 HeLa cells were seeded in 96-well plates and cultured for 24 h. Afterward, the cells were incubated with free IR780 (0.65, 1.3, and 2.6 $\mu g.mL^{-1}$) or AuMSS nanoformulations at different concentrations (50, 100, and 200 $\mu g.mL^{-1}$) for 24 h. Then, the cells were irradiated with a NIR laser (808 nm, 1.7 $W.cm^{-2}$) for 5 min. Non-irradiated cells were used as control. After 24 h, the cells' viability was assessed using the resazurin method as described above. Cells incubated with EtOH (99,9%) and cells only incubated with culture medium were used as K^+ and negative K^- controls, respectively.

2.2.11.2. Live/death assay

The phototherapeutic effect mediated by AuMSS, AuMSS/T-PEG-CH_3/T-GEL, IR780@AuMSS/T-PEG-CH_3/T-GEL nanorods, and free IR780 was also evaluated by fluorescence microscopy through the Live/Dead assay (Invitrogen, Life Technologies, USA). For that propose, 25,000 HeLa cells were seeded on µ-Slide 8 well Ibidi imaging plates (Ibidi GmbH, Germany), and incubated at 37°C in a humidified atmosphere (5% CO_2). After 48 h, HeLa cells were treated with AuMSS nanoformulations (100 $\mu g.mL^{-1}$) and free IR780 (1.3 $\mu g.mL^{-1}$) for 24 h and irradiated with a NIR laser (808 nm, 1.7 $W.cm^{-2}$) for 5 min. Afterward, cells were stained with Calcein AM and PI to allow the

visualization of live and dead cells, respectively. Finally, the live/death images were obtained by CLSM (Zeiss LSM 710, Carl Zeiss, Germany).

2.2.12. Statistical analysis

Data are presented as the mean±standard deviation (s.d.). The statistical analysis of experiments with two groups was performed with the unpaired *T-student test*. One-way analysis of variance (ANOVA) with the Student–Newman–Keuls post-test was used for multiple groups comparison. A *p*-value lower than 0.05 ($p<0.05$) was statistically significant. Statistical analysis was performed using GraphPad Prism v.6.0 software (Trial version, GraphPad Software, USA).

Chapter 3

Results and Discussion

3. Results and Discussion

3.1. Synthesis and characterization of T-PEG-CH_3 and T-GEL polymers

PEG-CH_3 is a biocompatible and amphiphilic polymer that can act as has a solubilizer agent to improve the colloidal stability and blood circulation time of AuMSS nanoparticles [185]. Such is attributed to the PEG capacity to decrease the adsorption of proteins on the surface of nanoparticles, reducing their recognition by the immune system and consequent elimination [186]. Further, increased blood circulation times have been correlated with higher probabilities of the nanoparticles accumulate in the tumor tissue [187]. Otherwise, GEL is a natural polymer obtained through the hydrolysis of collagen with biodegradability and biocompatibility properties [188, 189]. Further, GEL presents specific binding domains, known as RGD sequences, with specificity to $\alpha v\beta_3$ integrin receptors overexpressed in cancer cell membranes, which consequently will improve the AuMSS nanoparticles' specificity to the cancer cells and therapeutic potential [190, 191]. For that purpose, PEG-CH_3 and GEL polymers were previously modified with TESPIC (T-PEG-CH_3 and T-GEL silane derivatives) through a hydrogen-transfer nucleophilic addition reaction to enable their posterior chemical grafting in AuMSS surface (Figure 12).

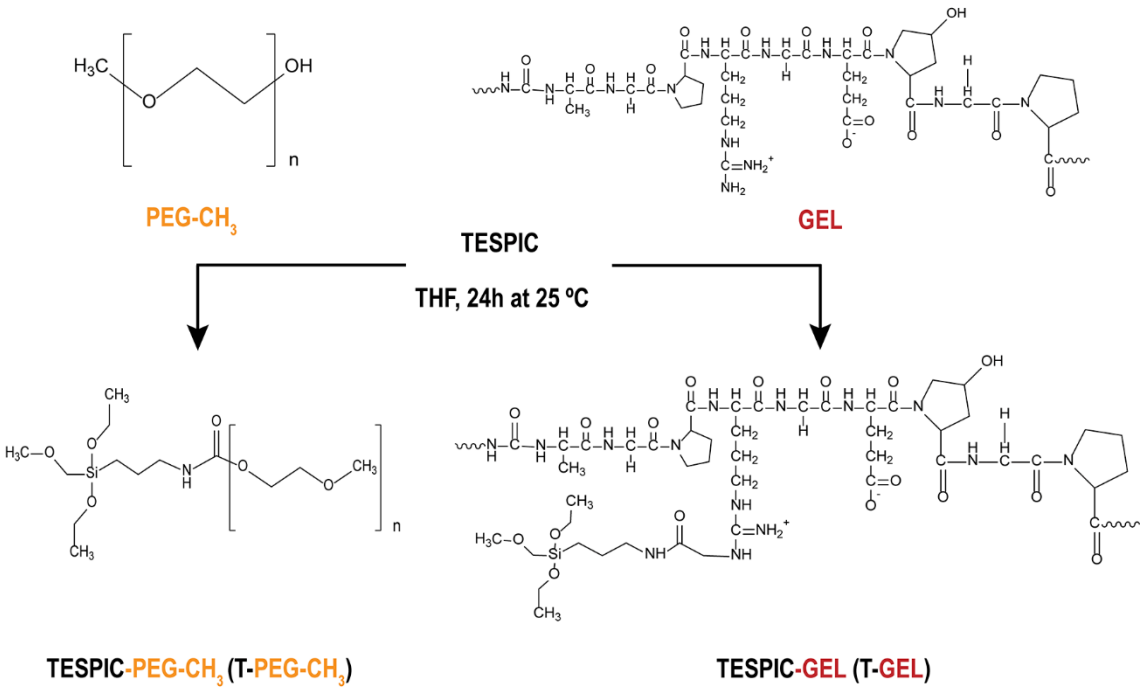

Figure 12: Schematic synthesis of T-PEG-CH_3 and T-GEL polymers.

The modification of GEL and PEG-CH_3 with TESPIC was confirmed through FTIR analysis. The FTIR spectra of GEL and T-GEL shows the characteristic peaks of GEL at 3,288 cm^{-1}, corresponding to the N-H vibrations, and at 1,680-1,640 cm^{-1} region attributed to the strong C=O stretching of amide II [192]. After modification with TESPIC, the T-GEL spectrum showed some changes at the 1,000-1,100 cm^{-1} region due to the absorption band of the Si-O-C bonds. Otherwise, the T-PEG-CH_3 shows both the PEG-CH_3 characteristic peaks at 2,800-2,900 cm^{-1} (C-H stretching) and the peaks corresponding to the C=O stretching of amide II (1,680-1,640 cm^{-1}) bond resulting from the TESPIC linkage (Figure 13) [126].

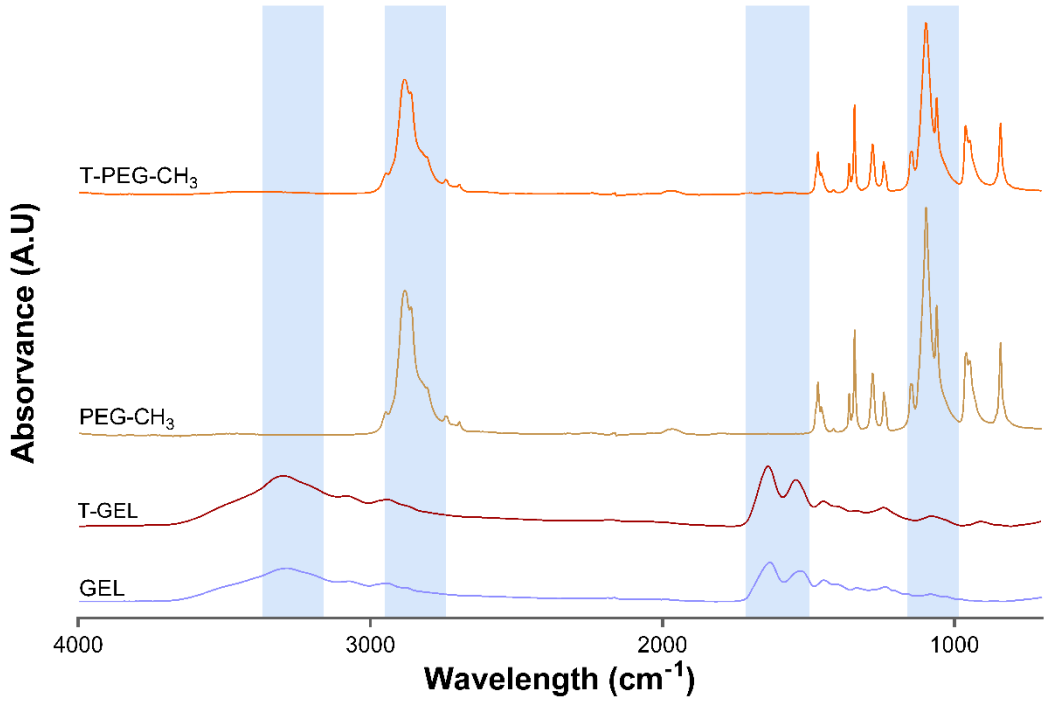

Figure 13: FTIR spectra of GEL, T-GEL, PEG-CH_3, and T-PEG-CH_3 polymers.

3.2. Synthesis and characterization of AuMSS nanorods

The synthesis of AuMSS nanorods was performed using a seed-mediated methodology already described in the literature [193, 194]. The synthesis method is divided into three main steps: i) production of small gold spheres (seeds), ii) seed growth forming the gold nanorods, iii) and the coating with a mesoporous silica shell, using CTAB as a template to promote the formation of the mesopores. The successful synthesis of the AuMSS nanorods and their core-shell organization was confirmed by TEM images (Figure 14 A). Additionally, the analysis of TEM images demonstrates the presence of gold nanorods coated with a mesoporous silica shell. Further, the ImageJ measurements show that the gold core had a mean length and width of 53±11 nm and 19±4 nm, respectively,

corresponding to an A.R. of 2.8. Additionally, the AuMSS nanorods present a mesoporous silica layer with 30 nm of thickness, which results in nanoparticles with a total length and width of 96±15 nm and 66±14 nm, respectively.

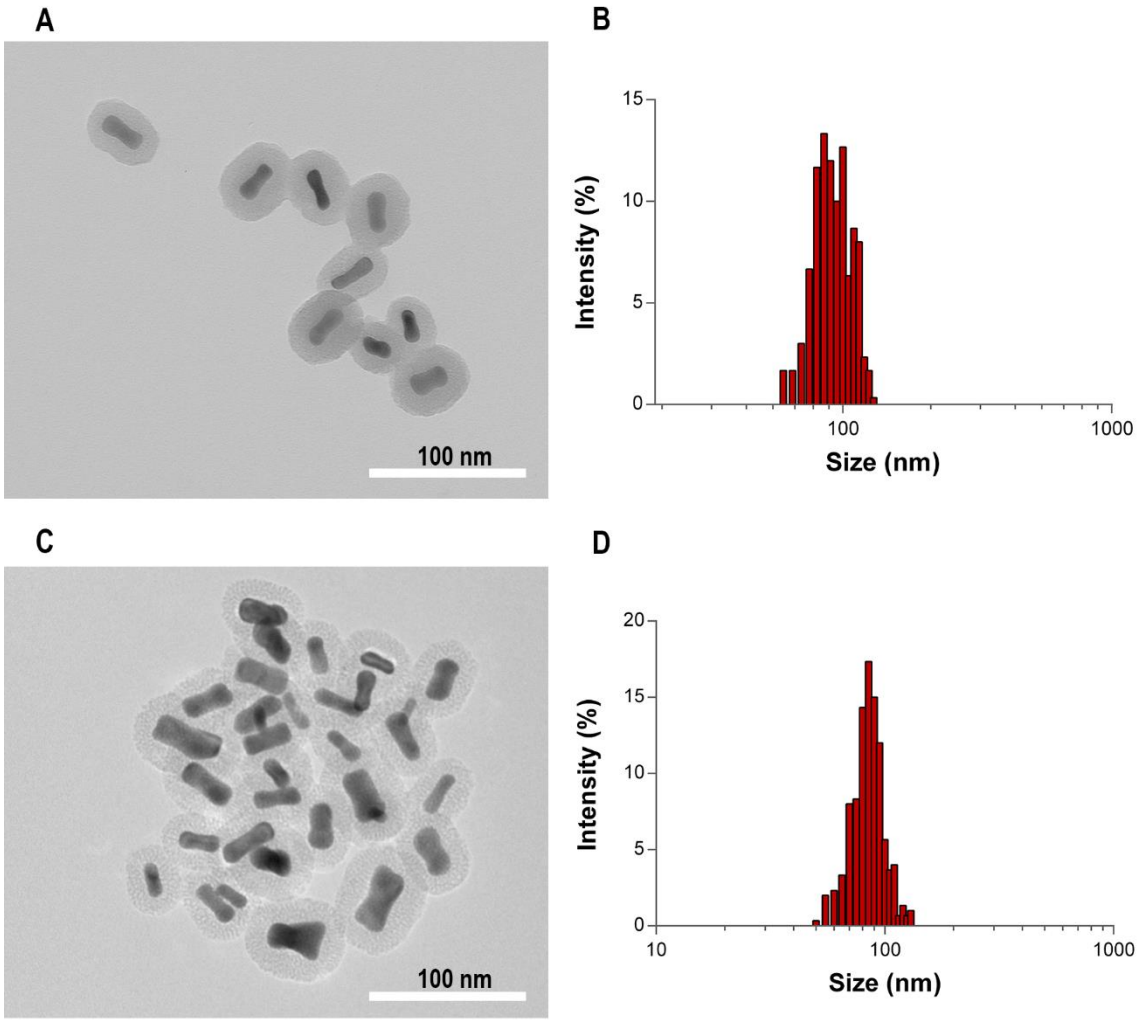

Figure 14: Size analysis of AuMSS and AuMSS/T-PEG-CH_3/T-GEL. TEM images of AuMSS (A) and AuMSS/T-PEG-CH_3/T-GEL nanorods (B). AuMSS size distribution of AuMSS (C) and AuMSS/T-PEG-CH_3/T-GEL (D) (length and width included), n=300.

After the AuMSS nanorods functionalization with T-PEG-CH_3 and T-GEL polymers, the TEM images analysis does not show any significant changes in overall nanoparticles size (L: 84±14 nm and W: 52±10 nm, Figure 14 C). Thus, the overall size of AuMSS formulations allows them to take advantage of the enhanced permeability and retention effect, which consequently enable their passive accumulation in the tumor tissue [47].

The successful removal of the CTAB and the formation of the mesoporous silica shell was evaluated by FTIR analysis (Figure 15 A). CTAB possesses two characteristic peaks, 2,850-2,950 cm^{-1} (corresponding to the C-H vibration), and 1,450-1,500 cm^{-1}

(corresponding to the CH_3-N^+ deformation) [180]. Therefore, the absence of these two characteristic bands in the AuMSS nanorods FTIR spectrum confirms the complete removal of the cytotoxic CTAB molecules. Additionally, it is also possible to observe the characteristics peaks of the mesoporous silica shell in the 750-1,150 cm^{-1}, which correspond to Si-O-Si and Si-OH vibrations [181].

3.3. Functionalization of the AuMSS nanorods

The immobilization of T-PEG-CH_3 and T-GEL on the surface of the AuMSS nanorods was achieved by exploring the condensation of the silane-modified polymers with the Si-OH groups present on the silica surface, originating the AuMSS/T-PEG-CH_3/T-GEL nanorods. The functionalization of AuMSS nanorods was evaluated by recording the changes in the nanoparticles' zeta potential. The AuMSS nanorods presented a negative surface charge, -23 mV, due to the silanol groups present on the mesoporous silica surface (Figure 15 B). The immobilization of T-PEG-CH_3 and T-GEL resulted in the neutralization of the AuMSS surface charge to -7.46 mV. Such can have a great impact on the nanomaterials' performance since neutral surface charges (±10 mV) are often considered ideal for biological applications due to the reduced RES recognition and improved blood circulation time [195].

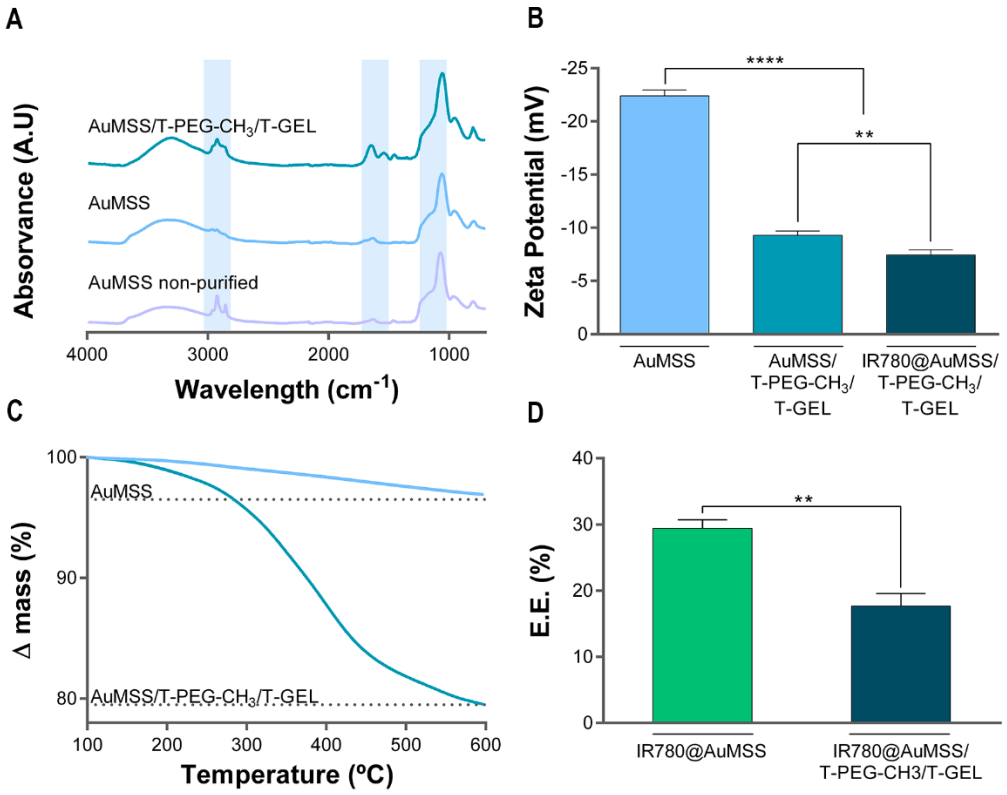

Figure 15: Physicochemical characterization of AuMSS formulations. (A) FTIR spectra of AuMSS non-purified, AuMSS, and AuMSS/T-PEG-CH_3/T-GEL nanorods. (B) Surface charge of AuMSS, AuMSS/T-PEG-CH_3/T-GEL, and IR780@AuMSS/T-PEG-CH_3/T-GEL. Data are presented as mean±s.d., $^{**}p<0.01$, $^{****}p<0.0001$ n=3. (C) TGA analysis of AuMSS and AuMSS/T-PEG-CH_3/T-GEL nanoparticles. (D) IR780 E.E. on AuMSS and AuMSS/T-PEG-CH_3/T-GEL nanoparticles. Data are presented as mean±s.d., n=3.

Additionally, the functionalization of AuMSS nanoparticles was also confirmed through FTIR analysis (Figure 15 A). The AuMSS/T-PEG-CH_3/T-GEL presented the characteristic peaks of mesoporous silica in the 750-1,100 cm^{-1} region, as well as the PEG-CH_3 C-H stretching at 2,900 cm^{-1} and the GEL C=O stretching at 1,650 cm^{-1}. Further, the polymer content on AuMSS/T-PEG-CH_3/T-GEL nanoparticles was determined by TGA analysis (Fig. 15 C). In Figure 15 C, it is possible to observe that the bare AuMSS nanorods present only 4% of weight loss, which can be attributed to the evaporation of water molecules in the interior of the mesopores and the loss of the hydroxyl groups present on nanoparticles' surface. Otherwise, the AuMSS/T-PEG-CH_3/T-GEL presented a weight loss of 20% due to the pyrolysis of the polymers. Overall, the presented results corroborate the successful immobilization of GEL and PEG on the surface of the AuMSS nanorods.

3.4. Evaluation of the IR780 loading

IR780 is a small molecule with an absorption peak at 780 nm that can mediate the generation of ROS (PDT) and heat (PTT) upon irradiation with NIR light [196]. However, this small molecule presents low solubility and tumor uptake, presenting a rapid blood clearance and acute toxicity [152]. Therefore, the encapsulation of IR780 in different nanostructures has been explored to improve its solubility and tumor accumulation [151, 152]. So, in this work, it was hypothesized that the IR780 encapsulation in AuMSS nanorods may contribute to improving the AuMSS photothermal capacity and overall therapeutic potential.

The AuMSS and AuMSS/T-PEG-CH_3/T-GEL nanorods 'ability to encapsulate IR780 was characterized by measuring the E.E. The encapsulation of the IR780 was performed by resuspending AuMSS and AuMSS/T-PEG-CH_3/T-GEL nanorods in the IR780 solution for 48 h. The results show that AuMSS and AuMSS/T-PEG-CH_3/T-GEL nanorods presented an E.E of 29,4% and 17,7%, respectively (Figure 15 D). As expected, the results demonstrate that the AuMSS functionalization with T-PEG-CH_3 and T-GEL decreases the E.E. of the IR780, which can be attributed to a repulsion phenomenon (negatively charged polymers and IR780 molecules) and/or the blockage of AuMSS pores by the polymers.

3.5. *In vitro* evaluation of the photothermal capacity of AuMSS nanoformulations

The AuMSS, AuMSS/T-PEG-CH_3/T-GEL, and IR780@AuMSS/T-PEG-CH_3/T-GEL nanoformulations ability to be applied as photothermal agents was initially verified through UV-vis analysis (Figure 16). As expected, free IR780 presented a well-defined absorption peak in the NIR region at 780 nm (Figure 16). Otherwise, the UV-vis spectra of AuMSS nanorods show two absorption bands at 520 nm and 750 nm (*i.e.* NIR region), which correspond to the characteristic transversal and longitudinal plasmon resonances of gold nanorods. The strong absorption peak at 750 nm supports the application of AuMSS nanorods as photothermal agents. Moreover, the functionalization of the AuMSS nanorods with PEG-CH_3 and GEL did not induce any significant changes in the nanoparticles' absorption spectrum. Further, apart from the two absorption bands at 520 nm and 750 nm, the IR780@AuMSS/T-PEG-CH_3/T-GEL nanorods also presented a small deformation in the absorption spectra at ≈780 nm. Such corroborates the previous results demonstrating the successful loading of IR780 in the AuMSS nanorods.

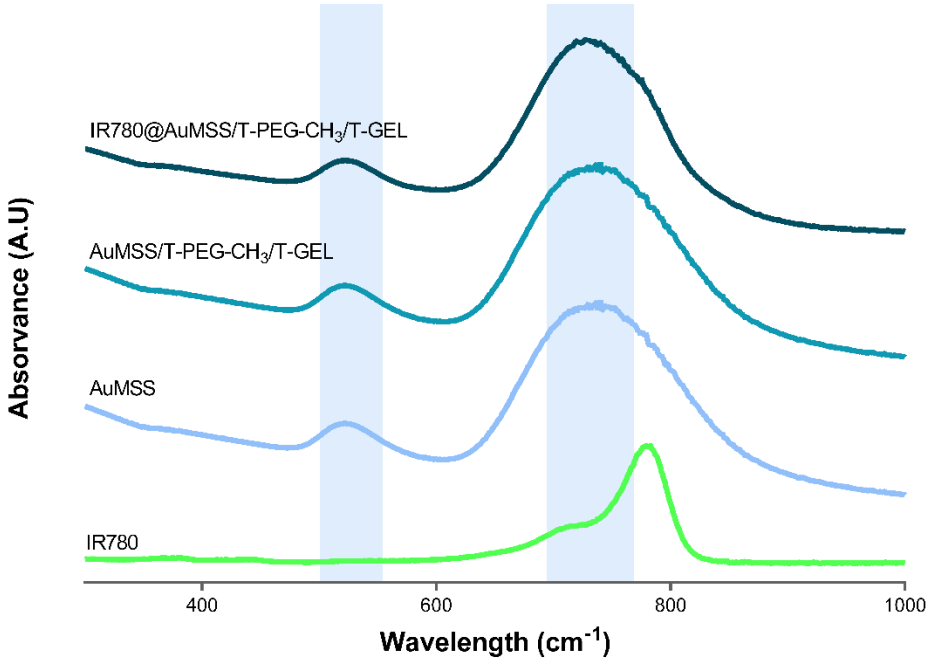

Figure 16: UV-Vis spectra of AuMSS nanoformulations and free IR780.

Then, the photothermal capacity of the free IR780 and the AuMSS nanoformulations was evaluated by measuring the temperatures changes when exposed to a NIR laser (808 nm, 1.7 W.cm^{-2}) for 1 to 10 min (Figure 17 A). It was possible to observe that both AuMSS nanoformulations can mediate an increase in temperature up to 10 min of irradiation. At

a concentration of 100 μg.mL^{-1} both AuMSS and AuMSS/T-PEG-CH_3/T-GEL mediated a ≈35°C temperature increase, contrasting with the obtained with the free IR780 (1.3 μg.mL^{-1} - a concentration equivalent to the IR780@AuMSS/T-PEG-CH_3/T-GEL). Otherwise, the IR780@AuMSS/T-PEG-CH_3/T-GEL nanorods presented a higher photothermal capacity, reaching a ΔT of ≈40°C after 6 min of irradiation. Nevertheless, from the 8 min of irradiation onward, the temperature of the medium started to decrease to a final ΔT of ≈37°C. This photothermal behavior can be explained by the photodegradation of IR780 upon continuous irradiation with NIR light [151]. To confirm these results, the photothermal stability of IR780@AuMSS/T-PEG-CH_3/T-GEL nanoparticles and free IR780 were evaluated by performing multiple irradiation cycles (Figure 17 B and C). After multiple NIR irradiations, free IR780 showed a decrease in the photothermal capacity, while IR780@AuMSS/T-PEG-CH_3/T-GEL maintained their photothermal profile, demonstrating the photothermal stability of the gold core. This enhanced photothermal stability can be explored for improving the therapeutic efficacy by performing multiple cycles of irradiation in the tumor tissue.

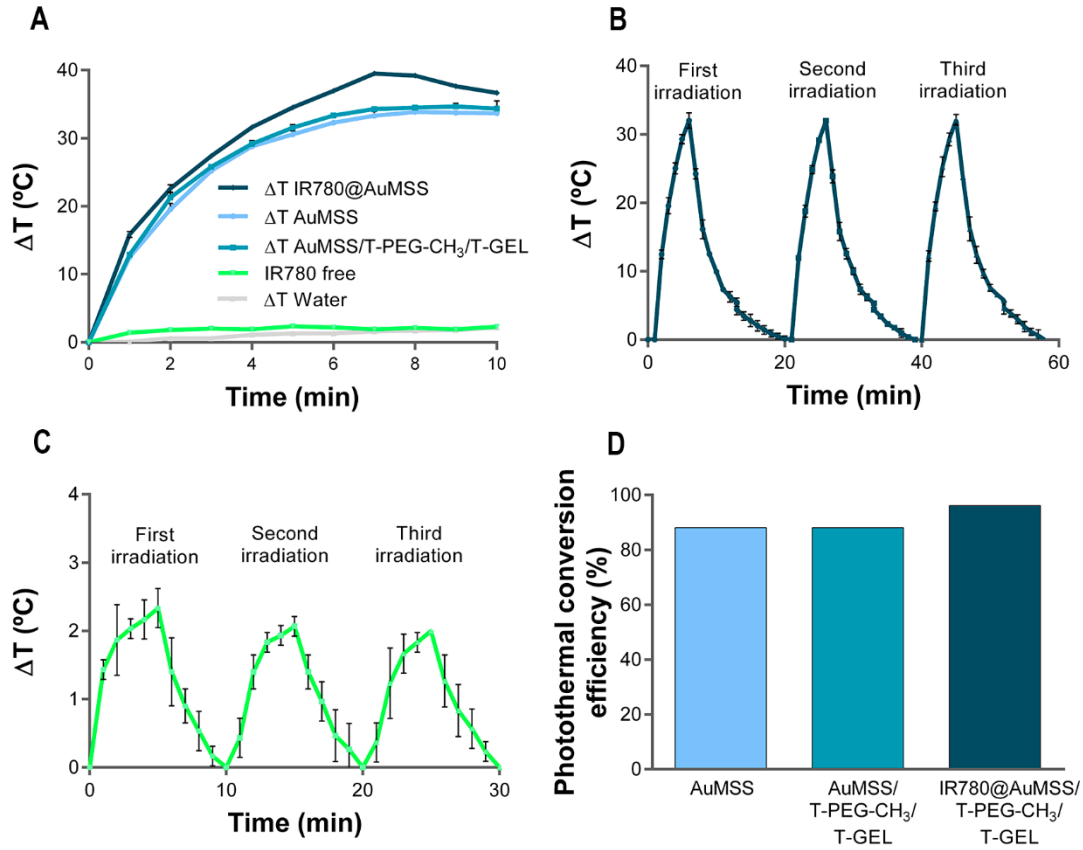

Figure 17: Characterization of the PTT capacity of AuMSS nanoformulations and free IR780. (A) Temperature variation curve of AuMSS nanoformulations and free IR780, NIR laser (808 nm,1.7 W cm^{-2}) irradiation for 10 min. (B) Temperature variation curve of multiple irradiations of IR780@AuMSS/T-PEG-CH_3/T-GEL nanoparticles and (C) free IR780, NIR laser (808 nm, 1.7 W cm^{-2}) irradiation for 5 min. (D) Photothermal conversion efficiency (%) of AuMSS, AuMSS/T-PEG-CH_3/T-GEL, and IR780@AuMSS/T-PEG-CH_3/T-GEL. Data are presented as mean±s.d..

Finally, the UV-vis and *in vitro* PTT results were used to calculate the photothermal conversion efficiency of the different AuMSS nanoformulations. The obtained results demonstrate that the encapsulation of IR780 improves the photothermal performance of AuMSS nanoparticles, the calculated photothermal conversion efficiency for AuMSS, AuMSS/T-PEG-CH_3/T-GEL, and IR780@AuMSS/T-PEG-CH_3/T-GEL was 88,1%, 88,1%, and 96,1%, respectively (Figure 17 D).

3.6. Characterization of the AuMSS nanorods biocompatibility

The cytocompatibility of AuMSS and AuMSS/T-PEG-CH_3/T-GEL nanorods was assessed both on HeLa and FibH cells through the resazurin assay. For that propose different concentrations of AuMSS nanoformulations (25 to 200 μg.mL^{-1}) were incubated with the cells for 24, 48, and 72 h. According to the ISO 10993-5 "*Biological evaluation of medical devices-Part 5: Tests for in vitro cytotoxicity*." a nanomaterial induces a cytotoxic effect when the cell viability is reduced by more than 30%. Therefore, Figure 18 demonstrates that both AuMSS and AuMSS/T-PEG-CH_3/T-GEL nanorods are biocompatible in all concentrations tested. These results are in agreement with the results described in the literature for AuMSS nanorods as well as with the safety profiles of GEL and PEG-CH_3 (FDA-approved polymers for biomedical applications) [180, 197].

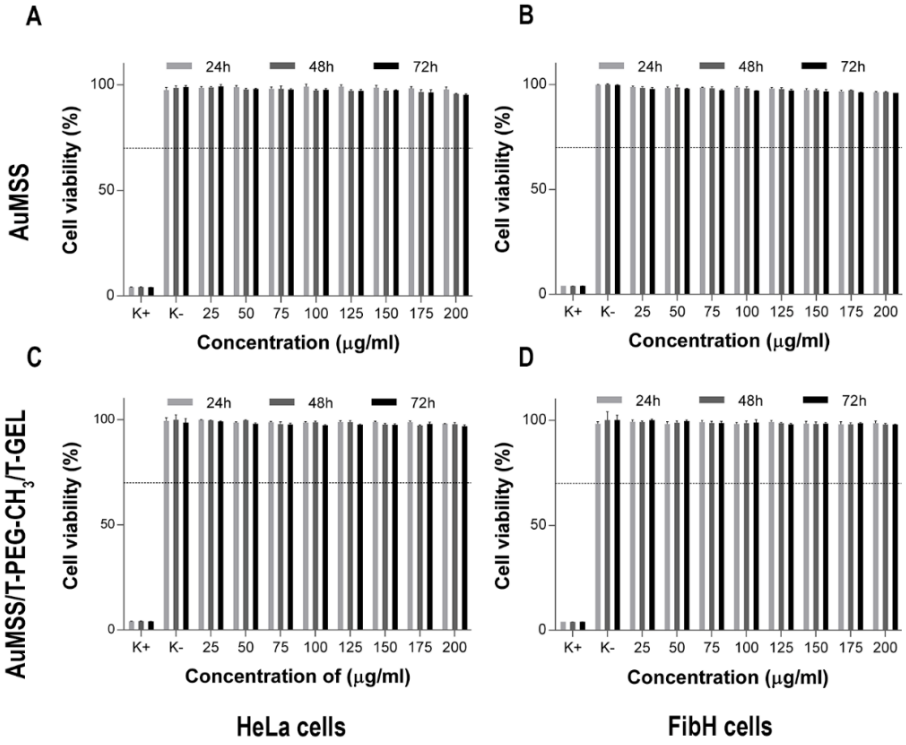

Figure 18: Evaluation of AuMSS and AuMSS/T-PEG-CH_3/T-GEL nanorods cytocompatibility in HeLa cells and FibH cells at 24, 48, and 72 h. (A) Cytocompatibility analysis for AuMSS nanorods in HeLa cells (B) and FibH cells (C) AuMSS/T-PEG-CH_3/T-GEL in HeLa cells and (D) and FibH cells. Positive control (K^+): cells treated with EtOH; negative control (K^-): cells without nanoparticle incubation. Data are presented as mean±s.d..

3.7. AuMSS nanorods uptake by HeLa and FibH cells

The nanoparticles uptake by cancer cells is one of the last barriers that nanoparticles have to surpass to induce their therapeutic effect. The nanoparticles' modification with agents that possess the ability to actively target cancer cells is one of the main approaches to improve the selectivity and the nanoparticles' uptake by cancer cells. For that propose, the uptake of AuMSS and AuMSS/T-PEG-CH_3/T-GEL nanorods was evaluated both in HeLa and FibH cells using fluorescence spectroscopy and CLSM. For that purpose, the AuMSS formulations were stained with FITC during 48 h to allow the nanoparticle tracking during the uptake assays. Afterward, the GEL targeting capacity was evaluated by measuring the fluorescence of the FITC-labeled AuMSS nanoformulations in HeLa (high $\alpha v\beta_3$ expression) and FibH (low $\alpha v\beta_3$ expression) cells through fluorescence spectroscopy (Figure 19).

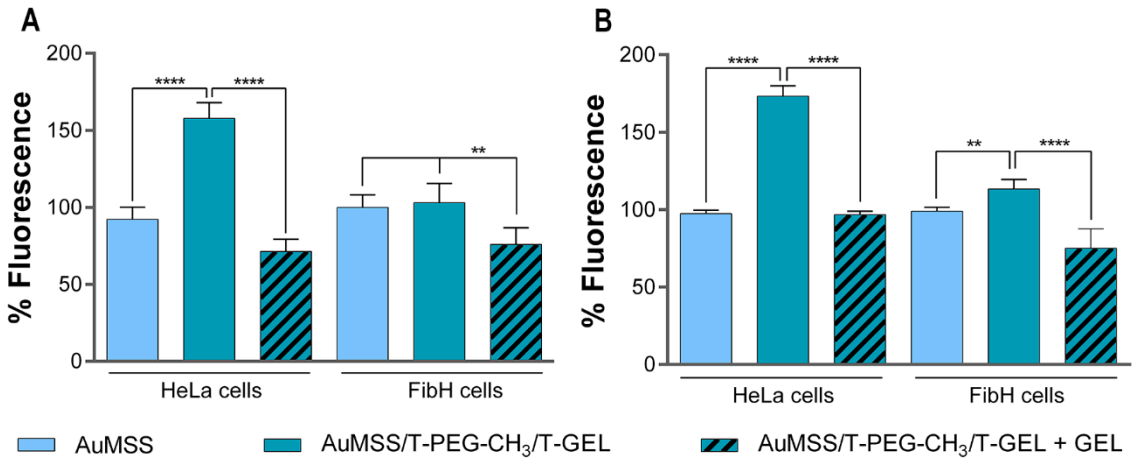

Figure 19: Analysis of AuMSS nanoformulations uptake by HeLa and FibH cells. (A) Fluorescence spectroscopy analysis of AuMSS nanoformulations at 100 µg.mL^{-1} and (B) 200 µg.mL^{-1}, fluorescence was normalized towards AuMSS nanorods group. Data are presented as mean±s.d., $^{**}p<0.01$, ****p<0.0001 n=5.

The obtained results demonstrated that the HeLa cells treated with FITC-stained AuMSS/T-PEG-CH_3/T-GEL nanorods presented a higher fluorescence intensity than those treated with AuMSS. Further, no significant differences were observed in the uptake of AuMSS formulations by FibH cells. Such results indicated that the increased uptake of AuMSS/T-PEG-CH_3/T-GEL nanorods in HeLa could be mediated by the interaction of RGD sequences available in GEL with the overexpressed $\alpha v\beta_3$ integrins. With that in mind, both HeLa and FibH were treated with free GEL for 4 h before the incubation with AuMSS nanoformulation. Such resulted in the reduction of the AuMSS/T-PEG-CH_3/T-GEL nanorods uptake in HeLa cells to values similar to those of AuMSS nanorods. Therefore, this experiment demonstrated that the introduction of GEL in the AuMSS nanorods confer to the nanoparticles a preferential uptake in cancer cells

overexpressing the $\alpha v\beta_3$ integrins. Such behavior is in accordance with the data available in the literature, where the functionalization of the nanoparticles with RGD sequences increased their cellular uptake by cancer cells overexpressing the $\alpha v\beta_3$ integrins [198-200]. Additionally, the uptake of AuMSS nanoformulation by HeLa cells was also confirmed by CLSM. In confocal images (Figure 20) it is possible to co-localize the FITC fluorescence (*i.e.* stained nanoparticles) with the cell cytoplasm, highlighted with the white arrows, confirming that both the AuMSS and AuMSS/T-PEG-CH_3/T-GEL can be uptaken by HeLa cells.

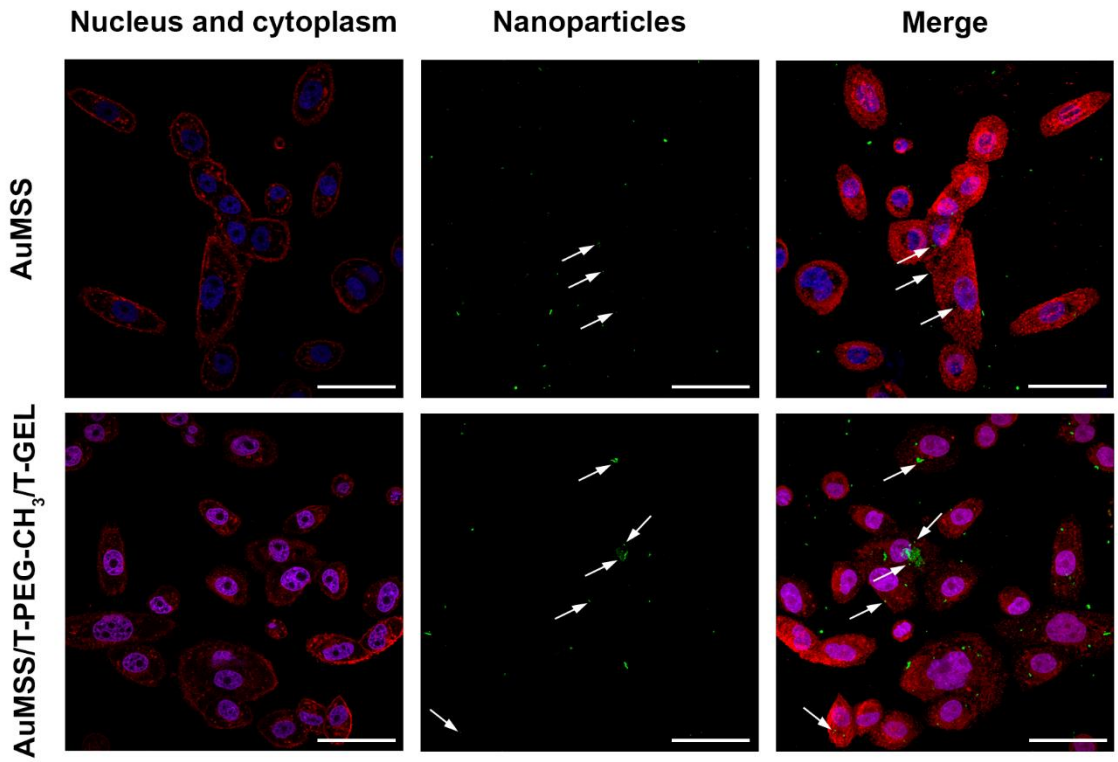

Figure 20: Representative confocal microscopy images of the AuMSS nanoformulations uptake by HeLa cells after 6 h of incubation at 200 $\mu g.mL^{-1}$. The white arrows are pointing to the internalized nanoparticles. The scale bar corresponds to 50 µm. Blue channel: Hoechst 33342® stained cell nucleus; red channel: WGA-Alexa Fluor 594®stained cell cytoplasm; green channel: FITC labeled nanoparticles.

3.8. Evaluation of intracellular ROS generation in HeLa cells

The intracellular generation of ROS by HeLa cells treated with AuMSS, AuMSS/T-PEG-CH_3/T-GEL, IR780@AuMSS/T-PEG-CH_3/T-GEL, and free IR780, in the presence or absence of NIR irradiation, was assessed using the H_2DCF-DA probe [180]. The obtained results revealed that in general the NIR irradiation induce an increase in the generation of ROS by HeLa cells (Figure 21 B). Additionally, it is possible to observe that the group treated with the IR780@AuMSS/T-PEG-CH_3/T-GEL

nanoformulation presented a generation of ROS 2-times superior to the other AuMSS formulations. Such an increase in the generation of ROS can be explained by the encapsulation of IR780 and its capacity to generate ROS in response to NIR laser irradiation. Otherwise, the free IR780 treated cells presented the lowest levels of ROS, which can be attributed to the photodegradation of non-protected IR780 during NIR irradiation.

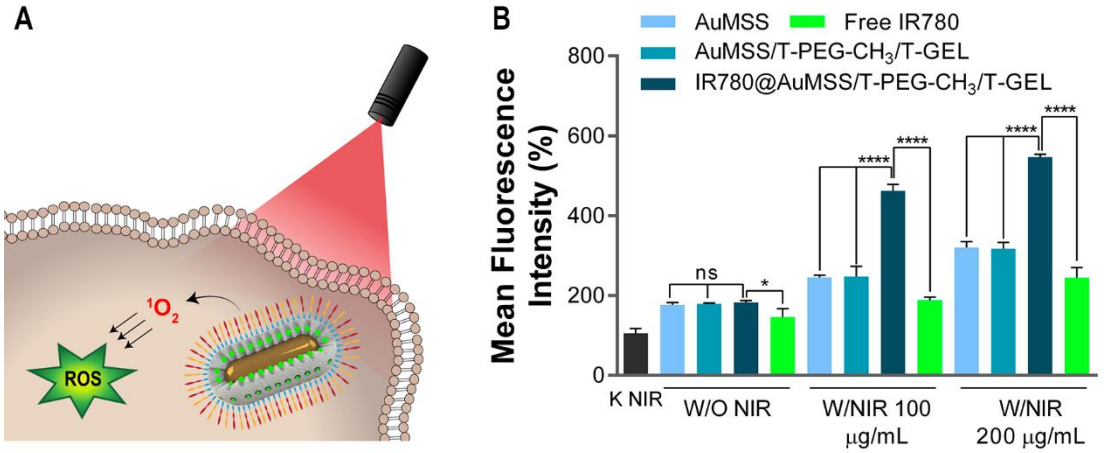

Figure 21: Analysis of the intracellular generation of ROS in HeLa cancer cells mediated by the AuMSS nanoformulations. (A) Schematic representation of the intracellular generation of ROS in response to AuMSS nanoformulations upon NIR irradiation (808 nm, 1.7 W.cm^{-2}, 5 min) (B) Evaluation of the intracellular generation of ROS, fluorescence was normalized towards K NIR group. K$^+$: cells treated with EtOH. K$^-$: non-irradiated HeLa cells and (K NIR): HeLa cells only exposed to NIR irradiation (808 nm, 1.7 W.cm^{-2}, 5 min). Data are presented as mean±s.d., *p<0.05, ****p<0.0001 n=4; n.s. – non-significant

3.9. Characterization of the AuMSS nanoformulations' photothermal cytotoxic activity

The anti-cancer potential of AuMSS nanoformulations as well as its capacity to combine PTT and PDT was evaluated in HeLa cells. For that purpose, HeLa cells were incubated with different concentrations of free IR780 (0.65, 1.3, and 2.6 µg.mL^{-1}, equivalent to that found in the nanoparticles) and AuMSS nanoformulations (50, 100, and 200 µg.mL^{-1}) for 24 h, and subjected to irradiation with a NIR laser for 5 min. In Figure 22 C, it can be observed that all AuMSS nanoformulations induced a decrease in the cancer cells' viability to values inferior to 5% when the concentration was superior to 100 µg.mL^{-1}. Moreover, at these concentration values, no significant differences were observed between the different AuMSS nanoformulations. Such results are in accordance with the previously described photothermal data, where the AuMSS nanoformulations can mediate a temperature increase superior to 30°C upon NIR laser irradiation. As described in the literature, temperatures higher than 45°C led to the elimination of cancer cells by promoting DNA damages, protein denaturation, and the destruction of the cell membrane. However, at the lowest concentrations tested (50 µg.mL^{-1}) the group

treated with IR780@AuMSS/T-PEG-CH_3/T-GEL nanorods presented the lowest cell viability (≈50%), followed by AuMSS/T-PEG-CH_3/T-GEL, AuMSS nanorods, and IR780. This enhanced antitumoral capacity of IR780@AuMSS/T-PEG-CH_3/T-GEL nanorods can be explained by the increased photothermal capacity as well as the combination of PTT and PDT. Additionally, the results also show an improved antitumoral capacity of AuMSS/T-PEG-CH_3/T-GEL when compared with AuMSS nanorods. Such difference demonstrates one more time the importance of GEL-mediated active targeting towards HeLa cancer cells, which increases the nanoparticle uptake by the cancer cells maximizing the therapeutic effect.

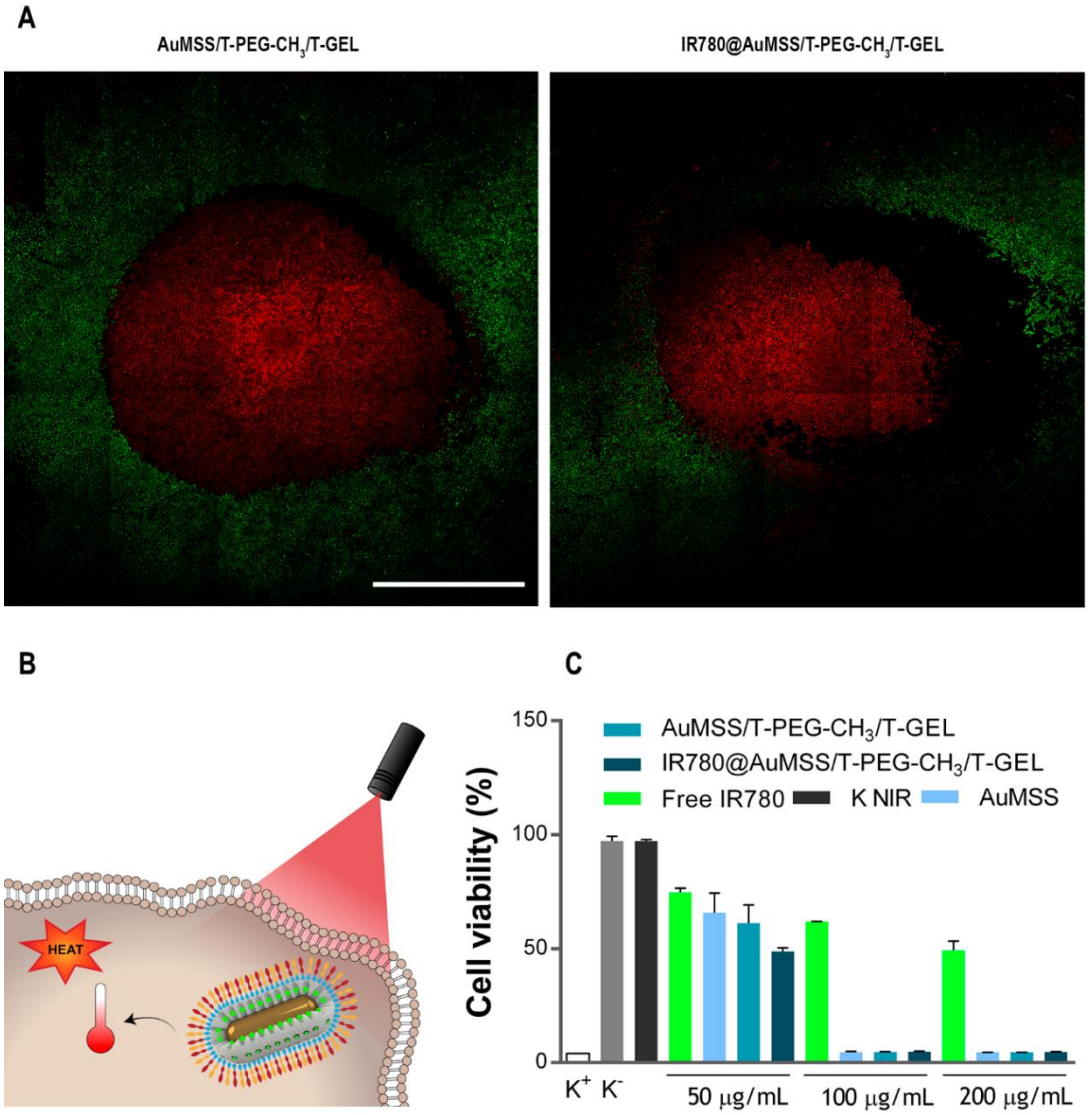

Figure 22: Analysis of the AuMSS nanoformulations' photothermal cytotoxic effect in HeLa cancer cells. (A) Live/Dead CLSM images of the HeLa cells incubated with AuMSS nanoformulations at a concentration of 100 µg.mL^{-1}. Green channel: Calcein stained cells; Red channel: PI stained cells. Scale bar: 200 µm. (B) Schematic representation of the AuMSS nanoformulations' cytotoxic activity upon NIR irradiation (808 nm, 1.7 W.cm^{-2}, 5 min) (C) Analysis of the HeLa cells viability in response to the treatment with free IR780 or AuMSS nanoformulations, fluorescence was normalized towards K NIR group. K^+: cells treated with EtOH. K^-: non-irradiated HeLa cells and (K NIR): HeLa cells only exposed to NIR irradiation (808 nm,1.7 W.cm^{-2}, 5 min).

Further, the photothermal effect mediated by the AuMSS/T-PEG-CH_3/T-GEL and IR780@AuMSS/T-PEG-CH_3/T-GEL on HeLa cells was also confirmed by the Live/Dead assays. The CLSM images (Figure 22 A and B) showed the presence of a zone with a high number of dead cells (red fluorescence) within the area irradiated with the NIR laser. Such confirm that the AuMSS/T-PEG-CH_3/T-GEL and IR780@AuMSS/T-PEG-CH_3/T-GEL nanorods can be activated by the irradiation of a NIR laser. Therefore, this on-demand and laser dependent behavior can be explored to confine the treatment to the target tumoral tissue. Moreover, the combination of AuMSS/T-PEG-CH_3/T-GEL and IR780 proved to be more effective than the therapeutic application of AuMSS/T-PEG-CH_3/T-GEL nanoparticles alone.

Chapter 4

Conclusion and Future Perspectives

4. Conclusion

Currently, cancer remains a major health problem affecting the worldwide population. Thus, novel anti-cancer therapeutic approaches have been developed to surpass the limitations of conventional therapies. Among the new therapeutic approaches, the application of nanomaterials capable of mediating a photothermal effect has been gaining great attention by researchers. Among the different nanomaterials applied in PTT, rod-shaped AuMSS nanoparticles present excellent physicochemical and biological properties that make them promising nanoplatforms for cancer therapy. Thus, AuMSS nanorods are multifunctional nanoparticles that can act simultaneously as photothermal, drug delivery, and bioimaging agents. However, it is crucial to improve their blood circulation time, cancer cells' specificity, and photothermal performance.

Taking this into account, the research work developed during the second year of my MSc aimed to develop a new surface functionalization for AuMSS rod-shaped nanoparticles based on the utilization of PEG-CH_3 and GEL to increase the blood circulation time and internalization by cancer cells, respectively. Additionally, IR780 was encapsulated for the first time in AuMSS nanoparticles to increase the photothermal capacity and allow its combination with the PDT, which can enhance the therapeutic potential of AuMSS nanorods. The obtained results demonstrate that the functionalization of AuMSS nanorods did not impact their overall size and PTT capacity. Otherwise, the polymers grafting on the AuMSS nanorods induced the neutralization of the surface charge from -23 to -7.46 mV. Additionally, the IR780@AuMSS/T-PEG-CH_3/T-GEL presented an enhanced photothermal capacity mediating a temperature increase of ≈40°C upon NIR laser irradiation, whereas the AuMSS and AuMSS/T-PEG-CH_3/T-GEL nanorods only reached a ΔT of 35°C. Additionally, the *in vitro* assays performed in the 2D cell culture models showed that all AuMSS nanoformulations were biocompatible at concentrations up to 200 $\mu g.mL^{-1}$. Moreover, the functionalization of AuMSS nanorods with GEL increased the nanoparticles' internalization by the HeLa cancer cells in a process mediated by the $\alpha v\beta_3$ integrins. Finally, the IR780@AuMSS/T-PEG-CH_3/T-GEL nanorods presented an enhanced cytotoxic effect towards HeLa cancer cells due to the combination of the increased PTT capacity and PDT (*i.e.* increased generation of ROS molecules).

In the future, the PEG-CH_3 and GEL polymers capacity to control the IR780 release from AuMS nanorods will be characterized in physiological and acidic pH. Moreover, the anti-cancer potential of IR780@AuMSS/T-PEG-CH_3/T-GEL will be characterized in 3D cell culture models. Furthermore, the simultaneous loading IR780 and

chemotherapeutic drug (*e.g*. DOX) will also be considered to improve the anti-cancer efficacy of AuMSS nanoparticles. Then, the most promising AuMSS nanoformulation will proceed to *in vivo* assays to explore the PEG-CH_3 and GEL potential to improve the biodistribution and selectivity of the nanoparticles as well as to characterize the AuMSS biosafety and anti-tumoral effect.

Chapter 5
References

5. References

[1] L.A. Torre, F. Bray, R.L. Siegel, J. Ferlay, J. Lortet-Tieulent, A. Jemal, Global cancer statistics, 2012, CA Cancer J. Clin., 65 (2015) 87-108.

[2] R.L. Siegel, K.D. Miller, A. Jemal, Cancer statistics, 2020, CA Cancer J. Clin., 70 (2020) 7-30.

[3] F. Bray, J. Ferlay, I. Soerjomataram, R.L. Siegel, L.A. Torre, A. Jemal, Global cancer statistics 2018: GLOBOCAN estimates of incidence and mortality worldwide for 36 cancers in 185 countries, CA Cancer J. Clin., 68 (2018) 394-424.

[4] Miranda N GM, Andrade C, Santos G. Programa Nacional para as Doenças Oncológicas. Direção-Geral da Saúde. 2017.

[5] C. Stein, G. Colditz, Modifiable risk factors for cancer, Br. J. Cancer, 90 (2004) 299-303.

[6] J.S. Barclay, J.E. Owens, L.J. Blackhall, Screening for substance abuse risk in cancer patients using the Opioid Risk Tool and urine drug screen, Suport Care Cancer, 22 (2014) 1883-1888.

[7] S. Singh, B. Sharma, S.S. Kanwar, A. Kumar, Lead phytochemicals for anticancer drug development, Front. Plant Sci., 7 (2016) 1667.

[8] D.F. Quail, J.A. Joyce, Microenvironmental regulation of tumor progression and metastasis, Nat. Med., 19 (2013) 1423-1437.

[9] B.T. Yuhan, P.F. Svider, S. Mutchnick, A. Sheyn, Benign and malignant oral lesions in children and adolescents: an organized approach to diagnosis and management, Pediatr. Clin., 65 (2018) 1033-1050.

[10] W. Zou, Immunosuppressive networks in the tumour environment and their therapeutic relevance, Nat. Rev. Cancer, 5 (2005) 263-274.

[11] D. Hanahan, R.A. Weinberg, Hallmarks of cancer: the next generation, Cell, 144 (2011) 646-674.

[12] L. Vannucci, Stroma as an active player in the development of the tumor microenvironment, Cancer Microenviron., 8 (2015) 159-166.

[13] E. Witsch, M. Sela, Y. Yarden, Roles for growth factors in cancer progression, Physiology, 25 (2010) 85-101.

[14] D. Hanahan, R.A. Weinberg, The hallmarks of cancer, Cell, 100 (2000) 57-70.

[15] E. Giampazolias, S.W. Tait, Mitochondria and the hallmarks of cancer, FEBS J., 283 (2016) 803-814.

[16] P.A. Muller, K.H. Vousden, Mutant p53 in cancer: new functions and therapeutic opportunities, Cancer Cell, 25 (2014) 304-317.

[17] S.E. Artandi, R.A. DePinho, Telomeres and telomerase in cancer, Carcinogenesis, 31 (2010) 9-18.

[18] T. Liu, X. Yuan, D. Xu, Cancer-specific telomerase reverse transcriptase (TERT) promoter mutations: biological and clinical implications, Genes, 7 (2016) 38.
[19] H.L. Goel, A.M. Mercurio, VEGF targets the tumour cell, Nat. Rev. Cancer, 13 (2013) 871-882.
[20] M.J. Ernsting, M. Murakami, A. Roy, S.-D. Li, Factors controlling the pharmacokinetics, biodistribution and intratumoral penetration of nanoparticles, J. Control. Release, 172 (2013) 782-794.
[21] M. Canel, A. Serrels, M.C. Frame, V.G. Brunton, E-cadherin–integrin crosstalk in cancer invasion and metastasis, J. Cell. Sci., 126 (2013) 393-401.
[22] L.M. Coussens, Z. Werb, Matrix metal loproteinases and the development of cancer, Chem. Biol., 3 (1996) 895-904.
[23] J.C. Coffey, J. Wang, M. Smith, D. Bouchier-Hayes, T. Cotter, H. Redmond, Excisional surgery for cancer cure: therapy at a cost, Lancet. Oncol., 4 (2003) 760-768.
[24] A.D. Fitoussi, M. Berry, F. Fama, M.-C. Falcou, A. Curnier, B. Couturaud, F. Reyal, R.J. Salmon, Oncoplastic breast surgery for cancer: analysis of 540 consecutive cases [outcomes article], Plast. Reconstr. Surg., 125 (2010) 454-462.
[25] M. Michael, I.F. Tannock, Measuring health-related quality of life in clinical trials that evaluate the role of chemotherapy in cancer treatment, CMAJ, 158 (1998) 1727-1734.
[26] A. Romiti, M.C. Cox, I. Sarcina, R. Di Rocco, C. D'Antonio, V. Barucca, P. Marchetti, Metronomic chemotherapy for cancer treatment: a decade of clinical studies, Cancer Chemoth. Pharm., 72 (2013) 13-33.
[27] G. Delaney, S. Jacob, C. Featherstone, M. Barton, The role of radiotherapy in cancer treatment: estimating optimal utilization from a review of evidence-based clinical guidelines, ACS, 104 (2005) 1129-1137.
[28] S. Ishikura, Quality assurance of radiotherapy in cancer treatment: toward improvement of patient safety and quality of care, Jpn. J. Clin. Oncol., 38 (2008) 723-729.
[29] C.E. DeSantis, C.C. Lin, A.B. Mariotto, R.L. Siegel, K.D. Stein, J.L. Kramer, R. Alteri, A.S. Robbins, A. Jemal, Cancer treatment and survivorship statistics, 2014, CA Cancer J. Clin., 64 (2014) 252-271.
[30] C.D. Runowicz, C.R. Leach, N.L. Henry, K.S. Henry, H.T. Mackey, R.L. Cowens-Alvarado, R.S. Cannady, M.L. Pratt-Chapman, S.B. Edge, L.A. Jacobs, American cancer society/American society of clinical oncology breast cancer survivorship care guideline, CA Cancer J. Clin., 66 (2016) 43-73.
[31] K.K. Collins, Y. Liu, M. Schootman, R. Aft, Y. Yan, G. Dean, M. Eilers, D.B. Jeffe, Effects of breast cancer surgery and surgical side effects on body image over time, Breast Cancer Res. Treat., 126 (2011) 167-176.

[32] B. Zachariah, L. Balducci, G. Venkattaramanabalaji, L. Casey, H.M. Greenberg, J.A. DelRegato, Radiotherapy for cancer patients aged 80 and older: a study of effectiveness and side effects, IJROBP, 39 (1997) 1125-1129.
[33] Q. Hu, W. Sun, C. Wang, Z. Gu, Recent advances of cocktail chemotherapy by combination drug delivery systems, Adv. Drug Delivery Rev., 98 (2016) 19-34.
[34] C. Holohan, S. Van Schaeybroeck, D.B. Longley, P.G. Johnston, Cancer drug resistance: an evolving paradigm, Nat. Rev. Cancer, 13 (2013) 714-726.
[35] Y. Tang, Y. Wang, M.F. Kiani, B. Wang, Classification, treatment strategy, and associated drug resistance in breast cancer, Clin. Breast Cancer, 16 (2016) 335-343.
[36] F.J. Sharom, Complex interplay between the P-glycoprotein multidrug efflux pump and the membrane: its role in modulating protein function, Front Oncol, 4 (2014) 41.
[37] R. Callaghan, F. Luk, M. Bebawy, Inhibition of the multidrug resistance P-glycoprotein: time for a change of strategy?, Drug Metab. Dispos., 42 (2014) 623-631.
[38] D. Cross, J.K. Burmester, Gene therapy for cancer treatment: past, present and future, Clin. Med. Res., 4 (2006) 218-227.
[39] M. Dougan, G. Dranoff, Immunotherapy of cancer, in: Innate immune regulation and cancer immunotherapy, Springer, 2012, pp. 391-414.
[40] L.J. Anghileri, J. Robert, Hyperthermia in cancer treatment, CRC Press, 2019.
[41] K. Hynynen, B. Lulu, Hyperthermia in cancer treatment, Invest. Radiol., 25 (1990) 824-834.
[42] B. Hildebrandt, P. Wust, O. Ahlers, A. Dieing, G. Sreenivasa, T. Kerner, R. Felix, H. Riess, The cellular and molecular basis of hyperthermia, Crit. Rev. Oncol. Hematol., 43 (2002) 33-56.
[43] M.J. Santos-Marques, F. Carvalho, C. Sousa, F. Remião, R. Vitorino, F. Amado, R. Ferreira, J.A. Duarte, M. de Lourdes Bastos, Cytotoxicity and cell signalling induced by continuous mild hyperthermia in freshly isolated mouse hepatocytes, Toxicology, 224 (2006) 210-218.
[44] R.W. Habash, R. Bansal, D. Krewski, H.T. Alhafid, Thermal therapy, part 2: hyperthermia techniques, Crit. Rev. Biomed. Eng., 34 (2006).
[45] P.F. Turner, Regional hyperthermia with an annular phased array, IEEE. Trans. Biomed. Eng., (1984) 106-114.
[46] R. Pettigrew, J.M. Galt, C. Ludgate, A. Smith, Clinical effects of whole-body hyperthermia in advanced malignancy, Br. Med. J., 4 (1974) 679-682.
[47] D. de Melo-Diogo, C. Pais-Silva, D.R. Dias, A.F. Moreira, I.J. Correia, Strategies to Improve Cancer Photothermal Therapy Mediated by Nanomaterials, Adv. Healthcare Mater., 6 (2017) 1700073.

[48] A.F. Moreira, D.R. Dias, I.J. Correia, Stimuli-responsive mesoporous silica nanoparticles for cancer therapy: A review, Micropor. Mesopor. Mat., 236 (2016) 141-157.
[49] J. Fang, H. Nakamura, H. Maeda, The EPR effect: unique features of tumor blood vessels for drug delivery, factors involved, and limitations and augmentation of the effect, Adv. Drug Delivery Rev., 63 (2011) 136-151.
[50] B. Liu, C. Li, Z. Cheng, Z. Hou, S. Huang, J. Lin, Functional nanomaterials for near-infrared-triggered cancer therapy, Biomater. Sci., 4 (2016) 890-909.
[51] A.F. Moreira, C.F. Rodrigues, C.A. Reis, E.C. Costa, P. Ferreira, I.J. Correia, Development of poly-2-ethyl-2-oxazoline coated gold-core silica shell nanorods for cancer chemo-photothermal therapy, Nanomedicine, 13 (2018) 2611-2627.
[52] Y. Matsumoto, J.W. Nichols, K. Toh, T. Nomoto, H. Cabral, Y. Miura, R.J. Christie, N. Yamada, T. Ogura, M.R. Kano, Vascular bursts enhance permeability of tumour blood vessels and improve nanoparticle delivery, Nat. Nanotechnol., 11 (2016) 533.
[53] H. Maeda, H. Nakamura, J. Fang, The EPR effect for macromolecular drug delivery to solid tumors: Improvement of tumor uptake, lowering of systemic toxicity, and distinct tumor imaging in vivo, Adv. Drug Delivery Rev., 65 (2013) 71-79.
[54] K.N. Andrade, A.M.P. Pérez, G.G.C. Arízaga, Passive and active targeting strategies in hybrid layered double hydroxides nanoparticles for tumor bioimaging and therapy, Appl. Clay Sci., 181 (2019) 105214.
[55] B.-J.L. Van Hong Nguyen, Protein corona: a new approach for nanomedicine design, Int. J. Nanomedicine, 12 (2017) 3137.
[56] S. Shen, S. Wang, R. Zheng, X. Zhu, X. Jiang, D. Fu, W. Yang, Magnetic nanoparticle clusters for photothermal therapy with near-infrared irradiation, Biomaterials, 39 (2015) 67-74.
[57] C. Chen, S. Wang, L. Li, P. Wang, C. Chen, Z. Sun, T. Song, Bacterial magnetic nanoparticles for photothermal therapy of cancer under the guidance of MRI, Biomaterials, 104 (2016) 352-360.
[58] S. Liang, C. Li, C. Zhang, Y. Chen, L. Xu, C. Bao, X. Wang, CD44v6 monoclonal antibody-conjugated gold nanostars for targeted photoacoustic imaging and plasmonic photothermal therapy of gastric cancer stem-like cells, Theranostics, 5 (2015) 970.
[59] H. Chen, L. Shao, T. Ming, Z. Sun, C. Zhao, B. Yang, J. Wang, Understanding the photothermal conversion efficiency of gold nanocrystals, Small, 6 (2010) 2272-2280.
[60] F. Yan, W. Duan, Y. Li, H. Wu, Y. Zhou, M. Pan, H. Liu, X. Liu, H. Zheng, NIR-laser-controlled drug release from DOX/IR-780-loaded temperature-sensitive-liposomes for chemo-photothermal synergistic tumor therapy, Theranostics, 6 (2016) 2337.

[61] M. Chu, Y. Shao, J. Peng, X. Dai, H. Li, Q. Wu, D. Shi, Near-infrared laser light mediated cancer therapy by photothermal effect of Fe3O4 magnetic nanoparticles, Biomaterials, 34 (2013) 4078-4088.
[62] K. Yang, H. Xu, L. Cheng, C. Sun, J. Wang, Z. Liu, In vitro and in vivo near-infrared photothermal therapy of cancer using polypyrrole organic nanoparticles, Adv. Mater., 24 (2012) 5586-5592.
[63] P. Liang, Q. Tang, Y. Cai, G. Liu, W. Si, J. Shao, W. Huang, Q. Zhang, X. Dong, Self-quenched ferrocenyl diketopyrrolopyrrole organic nanoparticles with amplifying photothermal effect for cancer therapy, Chem. Sci., 8 (2017) 7457-7463.
[64] X. Zhu, W. Feng, J. Chang, Y.-W. Tan, J. Li, M. Chen, Y. Sun, F. Li, Temperature-feedback upconversion nanocomposite for accurate photothermal therapy at facile temperature, Nat. Commun., 7 (2016) 10437.
[65] B. Zhang, H. Wang, S. Shen, X. She, W. Shi, J. Chen, Q. Zhang, Y. Hu, Z. Pang, X. Jiang, Fibrin-targeting peptide CREKA-conjugated multi-walled carbon nanotubes for self-amplified photothermal therapy of tumor, Biomaterials, 79 (2016) 46-55.
[66] Z. Zhou, B. Kong, C. Yu, X. Shi, M. Wang, W. Liu, Y. Sun, Y. Zhang, H. Yang, S. Yang, Tungsten oxide nanorods: an efficient nanoplatform for tumor CT imaging and photothermal therapy, Sci. Rep., 4 (2014) 3653.
[67] C.F. Rodrigues, C.A. Reis, A.F. Moreira, P. Ferreira, I.J. Correia, Optimization of gold core-mesoporous silica shell functionalization with TPGS and PEI for cancer therapy, Micropor. Mesopor. Mat., 285 (2019) 1-12.
[68] D. Jaque, L.M. Maestro, B. Del Rosal, P. Haro-Gonzalez, A. Benayas, J. Plaza, E.M. Rodriguez, J.G. Sole, Nanoparticles for photothermal therapies, Nanoscale, 6 (2014) 9494-9530.
[69] V. Amendola, R. Pilot, M. Frasconi, O.M. Maragò, M.A. Iatì, Surface plasmon resonance in gold nanoparticles: a review, J. Phys. Condens. Matter., 29 (2017) 203002.
[70] A.F. Moreira, C.F. Rodrigues, C.A. Reis, E.C. Costa, I.J. Correia, Gold-core silica shell nanoparticles application in imaging and therapy: A review, Micropor. Mesopor. Mat., 270 (2018) 168-179.
[71] P. Huang, J. Lin, W. Li, P. Rong, Z. Wang, S. Wang, X. Wang, X. Sun, M. Aronova, G. Niu, Biodegradable gold nanovesicles with an ultrastrong plasmonic coupling effect for photoacoustic imaging and photothermal therapy, Angew. Chem., 125 (2013) 14208-14214.
[72] J. Lin, S. Wang, P. Huang, Z. Wang, S. Chen, G. Niu, W. Li, J. He, D. Cui, G. Lu, Photosensitizer-loaded gold vesicles with strong plasmonic coupling effect for imaging-guided photothermal/photodynamic therapy, ACS Nano, 7 (2013) 5320-5329.

[73] J. Song, P. Huang, X. Chen, Preparation of plasmonic vesicles from amphiphilic gold nanocrystals grafted with polymer brushes, Nat. Protoc., 11 (2016) 2287-2299.
[74] P. Huang, O. Pandoli, X. Wang, Z. Wang, Z. Li, C. Zhang, F. Chen, J. Lin, D. Cui, X. Chen, Chiral guanosine 5′-monophosphate-capped gold nanoflowers: Controllable synthesis, characterization, surface-enhanced Raman scattering activity, cellular imaging and photothermal therapy, Nano Res., 5 (2012) 630-639.
[75] P. Huang, P. Rong, J. Lin, W. Li, X. Yan, M.G. Zhang, L. Nie, G. Niu, J. Lu, W. Wang, Triphase interface synthesis of plasmonic gold bellflowers as near-infrared light mediated acoustic and thermal theranostics, J. Am. Chem. Soc., 136 (2014) 8307-8313.
[76] J. Lin, M.G. Zhang, Y. Tang, B. Wen, H. Hu, J. Song, Y. Liu, P. Huang, X. Chen, Temporal-spatially transformed synthesis and formation mechanism of gold bellflowers, Nanoscale, 8 (2016) 7430-7434.
[77] C. Li, E. Mei, C. Chen, Y. Li, B. Nugasur, L. Hou, X. Ding, M. Hu, Y. Zhang, Z. Su, Gold-Nanobipyramid-Based Nanotheranostics for Dual-Modality Imaging-Guided Phototherapy, ACS Appl. Mater. Interfaces, 12 (2020) 12541-12548.
[78] M. Moros, A. Lewinska, F. Merola, P. Ferraro, M. Wnuk, A. Tino, C. Tortiglione, Gold nanorods and nanoprisms mediate different photothermal cell death mechanisms in vitro and in vivo, ACS Appl. Mater. Interfaces, 12 (2020) 13718-13730.
[79] G. Alfranca, Á. Artiga, G. Stepien, M. Moros, S.G. Mitchell, J.M. de la Fuente, Gold nanoprism–nanorod face off: comparing the heating efficiency, cellular internalization and thermoablation capacity, Nanomedicine, 11 (2016) 2903-2916.
[80] A. Ambrosone, P.d. Pino, V. Marchesano, W.J. Parak, J.M. de la Fuente, C. Tortiglione, Gold nanoprisms for photothermal cell ablation in vivo, Nanomedicine, 9 (2014) 1913-1922.
[81] B. Liu, W. Cao, G. Qiao, S. Yao, S. Pan, L. Wang, C. Yue, L. Ma, Y. Liu, D. Cui, Effects of gold nanoprism-assisted human PD-L1 siRNA on both gene down-regulation and photothermal therapy on lung cancer, Acta Biomater., 99 (2019) 307-319.
[82] W. Zhang, X. Ding, H. Cheng, C. Yin, J. Yan, Z. Mou, W. Wang, D. Cui, C. Fan, D. Sun, Dual-targeted gold nanoprism for recognition of early apoptosis, dual-model imaging and precise cancer photothermal therapy, Theranostics, 9 (2019) 5610.
[83] C. Bao, J. Conde, F. Pan, C. Li, C. Zhang, F. Tian, S. Liang, M. Jesus, D. Cui, Gold nanoprisms as a hybrid in vivo cancer theranostic platform for in situ photoacoustic imaging, angiography, and localized hyperthermia, Nano Res., 9 (2016) 1043-1056.
[84] C.D. De Souza, B.R. Nogueira, M.E.C. Rostelato, Review of the methodologies used in the synthesis gold nanoparticles by chemical reduction, J. Alloy. Compd., 798 (2019) 714-740.

[85] C.A. Reis, C.F. Rodrigues, A.F. Moreira, T.A. Jacinto, P. Ferreira, I.J. Correia, Development of gold-core silica shell nanospheres coated with poly-2-ethyl-oxazoline and beta-cyclodextrin aimed for cancer therapy, Mater. Sci. Eng. C Mater. Biol. Appl., 98 (2019) 960-968.
[86] X. Huang, W. Qian, I.H. El-Sayed, M.A. El-Sayed, The potential use of the enhanced nonlinear properties of gold nanospheres in photothermal cancer therapy, Lasers Surg. Med., 39 (2007) 747-753.
[87] P. Liu, W. Yang, L. Shi, H. Zhang, Y. Xu, P. Wang, G. Zhang, W.R. Chen, B. Zhang, X. Wang, Concurrent photothermal therapy and photodynamic therapy for cutaneous squamous cell carcinoma by gold nanoclusters under a single NIR laser irradiation, J. Mater. Chem. B, 7 (2019) 6924-6933.
[88] J.C.Y. Kah, R.C.Y. Wan, K.Y. Wong, S. Mhaisalkar, C.J.R. Sheppard, M. Olivo, Combinatorial treatment of photothermal therapy using gold nanoshells with conventional photodynamic therapy to improve treatment efficacy: an in vitro study, Lasers Surg. Med., 40 (2008) 584-589.
[89] P.K. Jain, M.A. El-Sayed, Universal scaling of plasmon coupling in metal nanostructures: extension from particle pairs to nanoshells, Nano Lett., 7 (2007) 2854-2858.
[90] B.M. Reinhard, M. Siu, H. Agarwal, A.P. Alivisatos, J. Liphardt, Calibration of dynamic molecular rulers based on plasmon coupling between gold nanoparticles, Nano Lett., 5 (2005) 2246-2252.
[91] R. Tannenbaum, M. Zubris, E.P. Goldberg, S. Reich, N. Dan, Polymer-directed nanocluster synthesis: control of particle size and morphology, Macromolecules, 38 (2005) 4254-4259.
[92] A.L. West, M.H. Griep, D.P. Cole, S.P. Karna, DNase 1 retains endodeoxyribonuclease activity following gold nanocluster synthesis, Anal. Chem., 86 (2014) 7377-7382.
[93] X. Qu, Y. Li, L. Li, Y. Wang, J. Liang, J. Liang, Fluorescent gold nanoclusters: synthesis and recent biological application, J. Nanomater., 2015 (2015).
[94] V. Chegel, O. Rachkov, A. Lopatynskyi, S. Ishihara, I. Yanchuk, Y. Nemoto, J.P. Hill, K. Ariga, Gold nanoparticles aggregation: drastic effect of cooperative functionalities in a single molecular conjugate, J. Phys. Chem. C, 116 (2012) 2683-2690.
[95] S. Park, H. Kim, S.C. Lim, K. Lim, E.S. Lee, K.T. Oh, H.-G. Choi, Y.S. Youn, Gold nanocluster-loaded hybrid albumin nanoparticles with fluorescence-based optical visualization and photothermal conversion for tumor detection/ablation, J. Control Release, 304 (2019) 7-18.

[96] C. Iodice, A. Cervadoro, A. Palange, J. Key, S. Aryal, M.R. Ramirez, C. Mattu, G. Ciardelli, B.E. O'Neill, P. Decuzzi, Enhancing photothermal cancer therapy by clustering gold nanoparticles into spherical polymeric nanoconstructs, Opt. Lasers Eng., 76 (2016) 74-81.
[97] H. Li, P. Wang, Y. Deng, M. Zeng, Y. Tang, W.-H. Zhu, Y. Cheng, Combination of active targeting, enzyme-triggered release and fluorescent dye into gold nanoclusters for endomicroscopy-guided photothermal/photodynamic therapy to pancreatic ductal adenocarcinoma, Biomaterials, 139 (2017) 30-38.
[98] C. Loo, A. Lin, L. Hirsch, M.-H. Lee, J. Barton, N. Halas, J. West, R. Drezek, Nanoshell-enabled photonics-based imaging and therapy of cancer, Technol. Cancer Res. T., 3 (2004) 33-40.
[99] Y. Gao, Y. Li, Y. Wang, Y. Chen, J. Gu, W. Zhao, J. Ding, J. Shi, Controlled synthesis of multilayered gold nanoshells for enhanced photothermal therapy and SERS detection, Small, 11 (2015) 77-83.
[100] L. Luo, Y. Bian, Y. Liu, X. Zhang, M. Wang, S. Xing, L. Li, D. Gao, Combined near infrared photothermal therapy and chemotherapy using gold nanoshells coated liposomes to enhance antitumor effect, Small, 12 (2016) 4103-4112.
[101] A.R. Rastinehad, H. Anastos, E. Wajswol, J.S. Winoker, J.P. Sfakianos, S.K. Doppalapudi, M.R. Carrick, C.J. Knauer, B. Taouli, S.C. Lewis, Gold nanoshell-localized photothermal ablation of prostate tumors in a clinical pilot device study, Proc. Natl. Acad. Sci. U S A., 116 (2019) 18590-18596.
[102] Y. Liu, M. Xu, Q. Chen, G. Guan, W. Hu, X. Zhao, M. Qiao, H. Hu, Y. Liang, H. Zhu, Gold nanorods/mesoporous silica-based nanocomposite as theranostic agents for targeting near-infrared imaging and photothermal therapy induced with laser, Int. J. Nanomedicine, 10 (2015) 4747.
[103] J. Pérez-Juste, L.M. Liz-Marzán, S. Carnie, D.Y. Chan, P. Mulvaney, Electric-field-directed growth of gold nanorods in aqueous surfactant solutions, Adv. Funct. Mater., 14 (2004) 571-579.
[104] D.K. Smith, B.A. Korgel, The importance of the CTAB surfactant on the colloidal seed-mediated synthesis of gold nanorods, Langmuir, 24 (2008) 644-649.
[105] P. Huang, L. Bao, C. Zhang, J. Lin, T. Luo, D. Yang, M. He, Z. Li, G. Gao, B. Gao, Folic acid-conjugated silica-modified gold nanorods for X-ray/CT imaging-guided dual-mode radiation and photo-thermal therapy, Biomaterials, 32 (2011) 9796-9809.
[106] M.A. Mackey, M.R. Ali, L.A. Austin, R.D. Near, M.A. El-Sayed, The most effective gold nanorod size for plasmonic photothermal therapy: theory and in vitro experiments, J. Phys. Chem. B, 118 (2014) 1319-1326.

[107] S. Wang, W. Xi, F. Cai, X. Zhao, Z. Xu, J. Qian, S. He, Three-photon luminescence of gold nanorods and its applications for high contrast tissue and deep in vivo brain imaging, Theranostics, 5 (2015) 251.
[108] L.M. Maestro, E. Camarillo, J.A. Sánchez-Gil, R. Rodríguez-Oliveros, J. Ramiro-Bargueño, A. Caamaño, F. Jaque, J.G. Solé, D. Jaque, Gold nanorods for optimized photothermal therapy: the influence of irradiating in the first and second biological windows, RSC Adv., 4 (2014) 54122-54129.
[109] W. Xu, J. Qian, G. Hou, Y. Wang, J. Wang, T. Sun, L. Ji, A. Suo, Y. Yao, A dual-targeted hyaluronic acid-gold nanorod platform with triple-stimuli responsiveness for photodynamic/photothermal therapy of breast cancer, Acta Biomater., 83 (2019) 400-413.
[110] X. Xia, Y. Xia, Gold nanocages as multifunctional materials for nanomedicine, Front. Phys., 9 (2014) 378-384.
[111] S.E. Skrabalak, J. Chen, Y. Sun, X. Lu, L. Au, C.M. Cobley, Y. Xia, Gold nanocages: synthesis, properties, and applications, Acc. Chem. Res., 41 (2008) 1587-1595.
[112] C.M. Cobley, L. Au, J. Chen, Y. Xia, Targeting gold nanocages to cancer cells for photothermal destruction and drug delivery, Expert. Opin. Drug. Deliv., 7 (2010) 577-587.
[113] E. Panfilova, A. Shirokov, B. Khlebtsov, L. Matora, N. Khlebtsov, Multiplexed dot immunoassay using Ag nanocubes, Au/Ag alloy nanoparticles, and Au/Ag nanocages, Nano Res., 5 (2012) 124-134.
[114] J. Yang, D. Shen, L. Zhou, W. Li, X. Li, C. Yao, R. Wang, A.M. El-Toni, F. Zhang, D. Zhao, Spatially confined fabrication of core–shell gold nanocages@ mesoporous silica for near-infrared controlled photothermal drug release, Chem. Mater., 25 (2013) 3030-3037.
[115] H. Cheng, D. Huo, C. Zhu, S. Shen, W. Wang, H. Li, Z. Zhu, Y. Xia, Combination cancer treatment through photothermally controlled release of selenous acid from gold nanocages, Biomaterials, 178 (2018) 517-526.
[116] H. Yuan, C.G. Khoury, H. Hwang, C.M. Wilson, G.A. Grant, T. Vo-Dinh, Gold nanostars: surfactant-free synthesis, 3D modelling, and two-photon photoluminescence imaging, Nanotechnology, 23 (2012) 075102.
[117] A. Guerrero-Martínez, S. Barbosa, I. Pastoriza-Santos, L.M. Liz-Marzán, Nanostars shine bright for you: colloidal synthesis, properties and applications of branched metallic nanoparticles, Curr. Opin. Colloid Interface Sci., 16 (2011) 118-127.
[118] C.G. Khoury, T. Vo-Dinh, Gold nanostars for surface-enhanced Raman scattering: synthesis, characterization and optimization, J. Phys. Chem. C, 112 (2008) 18849-18859.

[119] A. Espinosa, A.K. Silva, A. Sánchez-Iglesias, M. Grzelczak, C. Péchoux, K. Desboeufs, L.M. Liz-Marzán, C. Wilhelm, Cancer cell internalization of gold nanostars impacts their photothermal efficiency in vitro and in vivo: toward a plasmonic thermal fingerprint in tumoral environment, Adv. Healthc. Mater., 5 (2016) 1040-1048.
[120] D. Li, Y. Zhang, S. Wen, Y. Song, Y. Tang, X. Zhu, M. Shen, S. Mignani, J.-P. Majoral, Q. Zhao, Construction of polydopamine-coated gold nanostars for CT imaging and enhanced photothermal therapy of tumors: an innovative theranostic strategy, J. Mater. Chem. B, 4 (2016) 4216-4226.
[121] S. Wang, P. Huang, L. Nie, R. Xing, D. Liu, Z. Wang, J. Lin, S. Chen, G. Niu, G. Lu, Single continuous wave laser induced photodynamic/plasmonic photothermal therapy using photosensitizer-functionalized gold nanostars, Adv. Mater., 25 (2013) 3055-3061.
[122] S. Nouri, E. Mohammadi, B. Mehravi, F. Majidi, K. Ashtari, A. Neshasteh-Riz, S. Einali, NIR triggered glycosylated gold nanoshell as a photothermal agent on melanoma cancer cells, Artif. Cells, Nanomed., Biotechnol., 47 (2019) 2316-2324.
[123] L.L. Tan, L. Shang, Smart Delivery Systems Based on Poly (glycidyl methacrylate) s-Coated Organic/Inorganic Core–Shell Nanohybrids, Macromol. Rapid. Commun., 40 (2019) 1800879.
[124] J.-T. Song, X.-Q. Yang, X.-S. Zhang, D.-M. Yan, Z.-Y. Wang, Y.-D. Zhao, Facile synthesis of gold nanospheres modified by positively charged mesoporous silica, loaded with near-infrared fluorescent dye, for in vivo X-ray computed tomography and fluorescence dual mode imaging, ACS Appl. Mater. Interfaces, 7 (2015) 17287-17297.
[125] T. Salminen, M. Honkanen, T. Niemi, Coating of gold nanoparticles made by pulsed laser ablation in liquids with silica shells by simultaneous chemical synthesis, Phys. Chem. Chem. Phys., 15 (2013) 3047-3051.
[126] T.A. Jacinto, C.F. Rodrigues, A.F. Moreira, S.P. Miguel, E.C. Costa, P. Ferreira, I.J. Correia, Hyaluronic acid and Vitamin E polyethylene glycol succinate functionalized gold-core silica shell nanorods for cancer targeted photothermal therapy, Colloids Surf. B, (2020) 110778.
[127] C. Fernández-López, C. Mateo-Mateo, R.A. Alvarez-Puebla, J. Pérez-Juste, I. Pastoriza-Santos, L.M. Liz-Marzán, Highly controlled silica coating of PEG-capped metal nanoparticles and preparation of SERS-encoded particles, Langmuir, 25 (2009) 13894-13899.
[128] B. Zhang, L. Wei, Z. Chu, Development of indocyanine green loaded Au@ Silica core shell nanoparticles for plasmonic enhanced light triggered therapy, J. Photochem. Photobiol. A, 375 (2019) 244-251.

[129] B.N. Khlebtsov, V.A. Khanadeev, E.V. Panfilova, O.A. Inozemtseva, A.M. Burov, N.G. Khlebtsov, A simple Mie-type model for silica-coated gold nanocages, J. Quant. Spectrosc. Radiat. Transfer, 121 (2013) 23-29.
[130] Y.-S. Chen, W. Frey, S. Kim, K. Homan, P. Kruizinga, K. Sokolov, S. Emelianov, Enhanced thermal stability of silica-coated gold nanorods for photoacoustic imaging and image-guided therapy, Opt. Express, 18 (2010) 8867-8878.
[131] N. Fernandes, C.F. Rodrigues, A.F. Moreira, I.J. Correia, Overview of the application of inorganic nanomaterials in cancer photothermal therapy, Biomater. Sci., 8 (2020) 2990-3020.
[132] D. de Melo-Diogo, R. Lima-Sousa, C.G. Alves, I.J. Correia, Graphene family nanomaterials for application in cancer combination photothermal therapy, Biomater. Sci., 7 (2019) 3534-3551.
[133] C. Xu, D. Yang, L. Mei, Q. Li, H. Zhu, T. Wang, Targeting chemophotothermal therapy of hepatoma by gold nanorods/graphene oxide core/shell nanocomposites, ACS Appl. Mater. Interfaces, 5 (2013) 12911-12920.
[134] K. Turcheniuk, T. Dumych, R. Bilyy, V. Turcheniuk, J. Bouckaert, V. Vovk, V. Chopyak, V. Zaitsev, P. Mariot, N. Prevarskaya, Plasmonic photothermal cancer therapy with gold nanorods/reduced graphene oxide core/shell nanocomposites, RSC Adv., 6 (2016) 1600-1610.
[135] C. Wu, D. Li, L. Wang, X. Guan, Y. Tian, H. Yang, S. Li, Y. Liu, Single wavelength light-mediated, synergistic bimodal cancer photoablation and amplified photothermal performance by graphene/gold nanostar/photosensitizer theranostics, Acta Biomater., 53 (2017) 631-642.
[136] N. Guskos, J. Typek, M. Maryniak, Z. Roslaniec, D. Petridis, E. Senderek, FMR study of γ–Fe2O3 magnetic nanoparticles embedded in a poly (ether–ester) multiblock copolymers (PEN–block–PTMO) and (PTT–block–PTMO), Rev. Adv. Mater. Sci., 14 (2007) 157-162.
[137] B. Liu, C. Li, G. Chen, B. Liu, X. Deng, Y. Wei, J. Xia, B. Xing, P.a. Ma, J. Lin, Synthesis and optimization of MoS2@ Fe3O4-ICG/Pt (IV) nanoflowers for MR/IR/PA bioimaging and combined PTT/PDT/chemotherapy triggered by 808 nm laser, Adv. Sci., 4 (2017) 1600540.
[138] T. Zhang, Y. Li, W. Hong, Z. Chen, P. Peng, S. Yuan, J. Qu, M. Xiao, L. Xu, Glucose oxidase and polydopamine functionalized iron oxide nanoparticles: combination of the photothermal effect and reactive oxygen species generation for dual-modality selective cancer therapy, J. Mater. Chem. B, 7 (2019) 2190-2200.
[139] J. Estelrich, M.A. Busquets, Iron oxide nanoparticles in photothermal therapy, Molecules, 23 (2018) 1567.

[140] L.-Y. Bai, X.-Q. Yang, J. An, L. Zhang, K. Zhao, M.-Y. Qin, B.-Y. Fang, C. Li, Y. Xuan, X.-S. Zhang, Multifunctional magnetic-hollow gold nanospheres for bimodal cancer cell imaging and photothermal therapy, Nanotechnology, 26 (2015) 315701.
[141] C. Liang, X. Song, Q. Chen, T. Liu, G. Song, R. Peng, Z. Liu, Magnetic field-enhanced photothermal ablation of tumor sentinel lymph nodes to inhibit cancer metastasis, Small, 11 (2015) 4856-4863.
[142] J. Nam, S. Son, L.J. Ochyl, R. Kuai, A. Schwendeman, J.J. Moon, Chemo-photothermal therapy combination elicits anti-tumor immunity against advanced metastatic cancer, Nat. Commun., 9 (2018) 1-13.
[143] J. Hu, J. Wang, W. Tang, W. Yang, Y. Liu, R. Li, H. Liu, PEGylated polypyrrole–gold nanocomplex as enhanced photothermal agents against tumor cells, J. Mater. Sci., 55 (2020) 5587-5599.
[144] C. Leng, X. Zhang, F. Xu, Y. Yuan, H. Pei, Z. Sun, L. Li, Z. Bao, Engineering gold nanorod–copper sulfide heterostructures with enhanced photothermal conversion efficiency and photostability, Small, 14 (2018) 1703077.
[145] S.K. Maji, S. Yu, K. Chung, M. Sekkarapatti Ramasamy, J.W. Lim, J. Wang, H. Lee, D.H. Kim, Synergistic Nanozymetic Activity of Hybrid Gold Bipyramid–Molybdenum Disulfide Core@ Shell Nanostructures for Two-Photon Imaging and Anticancer Therapy, ACS Appl. Mater. Interfaces, 10 (2018) 42068-42076.
[146] J.S. Treger, M.F. Priest, R. Iezzi, F. Bezanilla, Real-time imaging of electrical signals with an infrared FDA-approved dye, Biophys. J., 107 (2014) L09-L12.
[147] I. Ocsoy, N. Isiklan, S. Cansiz, N. Özdemir, W. Tan, ICG-Conjugated magnetic graphene oxide for dual photothermal and photodynamic therapy, RSC Adv., 6 (2016) 30285-30292.
[148] T.I. Kim, K.H. Jeong, M.K. Shin, Verrucous epidermal nevus (VEN) successfully treated with indocyanine green (ICG) photodynamic therapy (PDT), JAAD case reports, 1 (2015) 312.
[149] E. Higbee-Dempsey, A. Amirshaghaghi, M.J. Case, J. Miller, T.M. Busch, A. Tsourkas, Indocyanine green–coated gold nanoclusters for photoacoustic imaging and photothermal therapy, Adv. Ther., 2 (2019) 1900088.
[150] J. Chen, Z. Sheng, P. Li, M. Wu, N. Zhang, X.-F. Yu, Y. Wang, D. Hu, H. Zheng, G.P. Wang, Indocyanine green-loaded gold nanostars for sensitive SERS imaging and subcellular monitoring of photothermal therapy, Nanoscale, 9 (2017) 11888-11901.
[151] M.M. Leitão, D. de Melo-Diogo, C.G. Alves, R. Lima-Sousa, I.J. Correia, Prototypic Heptamethine Cyanine Incorporating Nanomaterials for Cancer Phototheragnostic, Adv. Health. Mater., 9 (2020) 1901665.

[152] C.G. Alves, R. Lima-Sousa, D. de Melo-Diogo, R.O. Louro, I.J. Correia, IR780 based nanomaterials for cancer imaging and photothermal, photodynamic and combinatorial therapies, Int. J. Pharm., 542 (2018) 164-175.
[153] T. Nagy-Simon, M. Potara, A.-M. Craciun, E. Licarete, S. Astilean, IR780-dye loaded gold nanoparticles as new near infrared activatable nanotheranostic agents for simultaneous photodynamic and photothermal therapy and intracellular tracking by surface enhanced resonant Raman scattering imaging, J. Colloid Interface Sci., 517 (2018) 239-250.
[154] F. Xia, J. Niu, Y. Hong, C. Li, W. Cao, L. Wang, W. Hou, Y. Liu, D. Cui, Matrix metallopeptidase 2 targeted delivery of gold nanostars decorated with IR-780 iodide for dual-modal imaging and enhanced photothermal/photodynamic therapy, Acta Biomater., 89 (2019) 289-299.
[155] W. Gu, Q. Zhang, T. Zhang, Y. Li, J. Xiang, R. Peng, J. Liu, Hybrid polymeric nano-capsules loaded with gold nanoclusters and indocyanine green for dual-modal imaging and photothermal therapy, J. Mater. Chem. B, 4 (2016) 910-919.
[156] X. Jiang, B. Du, Y. Huang, M. Yu, J. Zheng, Cancer Photothermal Therapy with ICG-Conjugated Gold Nanoclusters, Bioconjugate Chem., 31 (2020) 1522-1528.
[157] Y. Liu, X. Zhi, M. Yang, J. Zhang, L. Lin, X. Zhao, W. Hou, C. Zhang, Q. Zhang, F. Pan, Tumor-triggered drug release from calcium carbonate-encapsulated gold nanostars for near-infrared photodynamic/photothermal combination antitumor therapy, Theranostics, 7 (2017) 1650.
[158] R. Liu, C. Hu, Y. Yang, J. Zhang, H. Gao, Theranostic nanoparticles with tumor-specific enzyme-triggered size reduction and drug release to perform photothermal therapy for breast cancer treatment, Acta Pharm. Sin. B, 9 (2019) 410-420.
[159] Q. You, Q. Sun, M. Yu, J. Wang, S. Wang, L. Liu, Y. Cheng, Y. Wang, Y. Song, F. Tan, BSA–bioinspired gadolinium hybrid-functionalized hollow gold nanoshells for NIRF/PA/CT/MR quadmodal diagnostic imaging-guided photothermal/photodynamic cancer therapy, ACS Appl. Mater. Interfaces, 9 (2017) 40017-40030.
[160] M.R. Younis, C. Wang, R. An, S. Wang, M.A. Younis, Z.-Q. Li, Y. Wang, A. Ihsan, D. Ye, X.-H. Xia, Low power single laser activated synergistic cancer phototherapy using photosensitizer functionalized dual plasmonic photothermal nanoagents, ACS Nano, 13 (2019) 2544-2557.
[161] J. Liu, H. Liang, M. Li, Z. Luo, J. Zhang, X. Guo, K. Cai, Tumor acidity activating multifunctional nanoplatform for NIR-mediated multiple enhanced photodynamic and photothermal tumor therapy, Biomaterials, 157 (2018) 107-124.
[162] H. Cui, D. Hu, J. Zhang, G. Gao, Z. Chen, W. Li, P. Gong, Z. Sheng, L. Cai, Gold Nanoclusters–Indocyanine Green Nanoprobes for Synchronous Cancer Imaging,

Treatment, and Real-Time Monitoring Based on Fluorescence Resonance Energy Transfer, ACS Appl. Mater. Interfaces, 9 (2017) 25114-25127.
[163] X. Huang, Y. Yin, M. Wu, W. Zan, Q. Yang, LyP-1 peptide-functionalized gold nanoprisms for SERRS imaging and tumor growth suppressing by PTT induced-hyperthermia, Chin. Chem. Lett., 30 (2019) 1335-1340.
[164] Y. Huang, Q. Liu, Y. Wang, N. He, R. Zhao, J. Choo, L. Chen, Gold nanorods functionalized by a glutathione response near-infrared fluorescent probe as a promising nanoplatform for fluorescence imaging guided precision therapy, Nanoscale, 11 (2019) 12220-12229.
[165] N. Khlebtsov, L. Dykman, Biodistribution and toxicity of engineered gold nanoparticles: a review of in vitro and in vivo studies, Chem. Soc. Rev., 40 (2011) 1647-1671.
[166] R. Arvizo, R. Bhattacharya, P. Mukherjee, Gold nanoparticles: opportunities and challenges in nanomedicine, Expert. Opin. Drug. Deliv., 7 (2010) 753-763.
[167] Y.-P. Jia, B.-Y. Ma, X.-W. Wei, Z.-Y. Qian, The in vitro and in vivo toxicity of gold nanoparticles, Chin. Chem. Lett., 28 (2017) 691-702.
[168] I. Fratoddi, I. Venditti, C. Cametti, M.V. Russo, How toxic are gold nanoparticles? The state-of-the-art, Nano Res., 8 (2015) 1771-1799.
[169] W. Cheng, S. Dong, E. Wang, Synthesis and self-assembly of cetyltrimethylammonium bromide-capped gold nanoparticles, Langmuir, 19 (2003) 9434-9439.
[170] T. Niidome, M. Yamagata, Y. Okamoto, Y. Akiyama, H. Takahashi, T. Kawano, Y. Katayama, Y. Niidome, PEG-modified gold nanorods with a stealth character for in vivo applications, J. Control. Release, 114 (2006) 343-347.
[171] D.S. Salem, M.A. Sliem, M. El-Sesy, S.A. Shouman, Y. Badr, Improved chemo-photothermal therapy of hepatocellular carcinoma using chitosan-coated gold nanoparticles, J. Photochem. Photobiol. B, Biol., 182 (2018) 92-99.
[172] K. Bolaños, M.J. Kogan, E. Araya, Capping gold nanoparticles with albumin to improve their biomedical properties, Int. J. Nanomedicine, 14 (2019) 6387.
[173] B. Cheng, H. He, T. Huang, S.S. Berr, J. He, D. Fan, J. Zhang, P. Xu, Gold nanosphere gated mesoporous silica nanoparticle responsive to near-infrared light and redox potential as a theranostic platform for cancer therapy, J. Biomed. Nanotechnol., 12 (2016) 435-449.
[174] P. Manivasagan, S.W. Jun, G. Hoang, S. Mondal, H. Kim, V.H.M. Doan, J. Kim, C.-S. Kim, J. Oh, Anti-EGFR antibody conjugated thiol chitosan-layered gold nanoshells for dual-modal imaging-guided cancer combination therapy, J. Control. Release, 311 (2019) 26-42.

[175] X.-D. Zhang, D. Wu, X. Shen, P.-X. Liu, F.-Y. Fan, S.-J. Fan, In vivo renal clearance, biodistribution, toxicity of gold nanoclusters, Biomaterials, 33 (2012) 4628-4638.
[176] Y. Chen, Z. Xu, D. Zhu, X. Tao, Y. Gao, H. Zhu, Z. Mao, J. Ling, Gold nanoparticles coated with polysarcosine brushes to enhance their colloidal stability and circulation time in vivo, J. Colloid Interface Sci., 483 (2016) 201-210.
[177] A. Kodiyan, E.A. Silva, J. Kim, M. Aizenberg, D.J. Mooney, Surface modification with alginate-derived polymers for stable, protein-repellent, long-circulating gold nanoparticles, ACS Nano, 6 (2012) 4796-4805.
[178] C. Xu, F. Chen, H.F. Valdovinos, D. Jiang, S. Goel, B. Yu, H. Sun, T.E. Barnhart, J.J. Moon, W. Cai, Bacteria-like mesoporous silica-coated gold nanorods for positron emission tomography and photoacoustic imaging-guided chemo-photothermal combined therapy, Biomaterials, 165 (2018) 56-65.
[179] H. Xie, Z.J. Wang, A. Bao, B. Goins, W.T. Phillips, In vivo PET imaging and biodistribution of radiolabeled gold nanoshells in rats with tumor xenografts, Int. J. Pharm., 395 (2010) 324-330.
[180] D.R. Dias, A.F. Moreira, I.J. Correia, The effect of the shape of gold core–mesoporous silica shell nanoparticles on the cellular behavior and tumor spheroid penetration, J. Mater. Chem. B, 4 (2016) 7630-7640.
[181] A.F. Moreira, V.M. Gaspar, E.C. Costa, D. de Melo-Diogo, P. Machado, C.M. Paquete, I.J. Correia, Preparation of end-capped pH-sensitive mesoporous silica nanocarriers for on-demand drug delivery, Eur. J. Pharm. Biopharm., 88 (2014) 1012-1025.
[182] A.F. Moreira, D.R. Dias, E.C. Costa, I.J. Correia, Thermo-and pH-responsive nano-in-micro particles for combinatorial drug delivery to cancer cells, Eur J Pharm Sci, 104 (2017) 42-51.
[183] X. Liu, B. Li, F. Fu, K. Xu, R. Zou, Q. Wang, B. Zhang, Z. Chen, J. Hu, Facile synthesis of biocompatible cysteine-coated CuS nanoparticles with high photothermal conversion efficiency for cancer therapy, Dalton Trans., 43 (2014) 11709-11715.
[184] V.M. Gaspar, A.F. Moreira, E.C. Costa, J.A. Queiroz, F. Sousa, C. Pichon, I.J. Correia, Gas-generating TPGS-PLGA microspheres loaded with nanoparticles (NIMPS) for co-delivery of minicircle DNA and anti-tumoral drugs, Colloids Surf., B, 134 (2015) 287-294.
[185] J.M. Harris, R.B. Chess, Effect of pegylation on pharmaceuticals, Nat. Rev. Drug Discov., 2 (2003) 214-221.
[186] B. Pelaz, P. del Pino, P. Maffre, R. Hartmann, M. Gallego, S. Rivera-Fernandez, J.M. de la Fuente, G.U. Nienhaus, W.J. Parak, Surface functionalization of nanoparticles

with polyethylene glycol: effects on protein adsorption and cellular uptake, ACS Nano, 9 (2015) 6996-7008.
[187] Y. Cui, H. Dong, X. Cai, D. Wang, Y. Li, Mesoporous silica nanoparticles capped with disulfide-linked PEG gatekeepers for glutathione-mediated controlled release, ACS Appl. Mater. Interfaces, 4 (2012) 3177-3183.
[188] M. Gómez-Guillén, B. Giménez, M.a. López-Caballero, M. Montero, Functional and bioactive properties of collagen and gelatin from alternative sources: A review, Food Hydrocoll., 25 (2011) 1813-1827.
[189] M.E. Hoque, T. Nuge, T.K. Yeow, N. Nordin, R. Prasad, Gelatin based scaffolds for tissue engineering-a review, Polym. Res. J., 9 (2015) 15.
[190] F. Danhier, A. Le Breton, V.r. Préat, RGD-based strategies to target alpha (v) beta (3) integrin in cancer therapy and diagnosis, Mol. Pharm., 9 (2012) 2961-2973.
[191] E. Hoch, C. Schuh, T. Hirth, G.E. Tovar, K. Borchers, Stiff gelatin hydrogels can be photo-chemically synthesized from low viscous gelatin solutions using molecularly functionalized gelatin with a high degree of methacrylation, J. Mater. Sci. Mater. Med., 23 (2012) 2607-2617.
[192] A. Haroun, S. El Toumy, Effect of natural polyphenols on physicochemical properties of crosslinked gelatin-based polymeric biocomposite, J. Appl. Polym. Sci., 116 (2010) 2825-2832.
[193] B. Nikoobakht, M.A. El-Sayed, Preparation and growth mechanism of gold nanorods (NRs) using seed-mediated growth method, Chem. Mater., 15 (2003) 1957-1962.
[194] I. Gorelikov, N. Matsuura, Single-step coating of mesoporous silica on cetyltrimethyl ammonium bromide-capped nanoparticles, Nano Lett., 8 (2008) 369-373.
[195] E. Fröhlich, The role of surface charge in cellular uptake and cytotoxicity of medical nanoparticles, Int. J. Nanomedicine, 7 (2012) 5577.
[196] C.G. Alves, D. de Melo-Diogo, R. Lima-Sousa, E.C. Costa, I.J. Correia, Hyaluronic acid functionalized nanoparticles loaded with IR780 and DOX for cancer chemo-photothermal therapy, Eur. J, Pharm. Biopharm., 137 (2019) 86-94.
[197] A. Laha, S. Majumdar, C.S. Sharma, Controlled Drug Release Formulation by Sequential Crosslinking of Multilayered Electrospun Gelatin Nanofiber Mat, MRS Adv., 1 (2016) 2107-2113.
[198] X. Li, L. Xing, Y. Hu, Z. Xiong, R. Wang, X. Xu, L. Du, M. Shen, X. Shi, An RGD-modified hollow silica@Au core/shell nanoplatform for tumor combination therapy, Acta Biomater., 62 (2017) 273-283.

[199] H. Zhou, H. Xu, X. Li, Y. Lv, T. Ma, S. Guo, Z. Huang, X. Wang, P. Xu, Dual targeting hyaluronic acid - RGD mesoporous silica coated gold nanorods for chemo-photothermal cancer therapy, Mater. Sci. Eng. C. Mater. Biol. Appl., 81 (2017) 261-270.
[200] J. Yang, Y. Luo, Y. Xu, J. Li, Z. Zhang, H. Wang, M. Shen, X. Shi, G. Zhang, Conjugation of iron oxide nanoparticles with RGD-modified dendrimers for targeted tumor MR imaging, ACS. Appl. Mater. Interfaces, 7 (2015) 5420-5428.